Inaugural Dissertation zur Erlangung des
Doktorgrades der Naturwissenschaften
der Justus-Liebig-Universität Gießen
(Fachbereich Physik)

Performance Studies and Improvements of a Time-of-Flight Detector for Isochronous Mass Measurements at the FRS-ESR Facility

vorgelegt von
Natalia Kuzminchuk
geboren in Raduzhny (Russland)

September 2011, Gießen

Gutachter: Prof Dr. Hans Geissel
Prof Dr. Volker Metag

Zusammenfassung

Die Isochrone Massenspektrometrie (IMS) wird im Fragmentseparator (FRS) und Experimentier-Speicherring (ESR) des Helmholtzzentrum für Schwerionenforschung (GSI) Darmstadt zur präzisen Messung von Kernmassen genutzt. Die IMS ermöglicht den Zugriff auf Nuklide mit Lebensdauern bis hinunter zu einigen zehn Mikrosekunden und besitzt eine Massengenauigkeit in der Größenordnung von bis zu 10^{-6}. Hierbei werden exotische Kerne bei relativistischen Energien via Projektil-Fragmentation und -Spaltung am Eingang des FRS produziert, im Fluge räumlich getrennt und im Speicherring gespeichert. Zur Kompensation der breiten Impulsverteilung des Ionenstrahls bei genauen Frequenzmessungen wird der Ring in einem isochronen Modus betrieben. Dieser spezielle Ring-Modus führt dazu, dass Ionen mit einem identischen Masse-zu-Ladungsverhältnis gleiche Umlauffrequenz im ESR besitzen.

Die Massen können dann aus präzisen Messungen der Umlauffrequenz abgeleitet werden. Dabei werden die zeitlichen Entwicklungen und Korrelationen der Umlauffrequenz der exotischen Kerne mit Hilfe eines Flugzeitdetektors im Innern des ESR gemessen. Im Detektor passieren die Ionen eine dünne Folie und lösen darin Sekundärelektronen durch atomare Wechselwirkungen aus, welche vorwärts und rückwärts gerichtet durch elektrische und magne-tische Felder zum Mikrokanalplatten-Detektor (MCP-Detektor) transportiert werden.

Im Rahmen der vorliegenden Dissertationsarbeit wurden die Eigenschaften des Detektors durch Computer-Simulationen untersucht und durch Online- sowie Offline-Experimente signifikant verbessert. Insbesondere wurden die Zeiteigenschaften und die Ratenfestigkeit experimentell gemessen und gesteigert. Die Verbesserungen der Nachweiseffizienz aus früheren Arbeiten wurde überprüft und die Verwendung dünnerer Kohlenstofffolien implementiert, um die Anzahl der Ionenumläufe im Ring zu erhöhen. Perspektivisch bildet diese Arbeit auch eine Grundlage für die Entwicklung eines Detektor-Systems für IMS im Collector Ring im FAIR.

Da die Massen der exotischen Nuklide direkt durch Umlaufzeitmessungen bestimmt werden, haben die Zeiteigenschaften des Detektors einen direkten Einfluss auf die Genauigkeit der bestimmten Masse. Daher wurden in der vorliegenden Arbeit die wichtigsten Beiträge wie Transportzeit von Sekundärelektronen, Durchlaufzeit durch die Mikrokanalplatten und die Methode zur Ereignis-Zeitbestimmung gemäß den MCP-Signalen analysiert und verbessert. Die Genauigkeit des Flugzeitdetektors wurde durch koinzidente Flugzeitmessungen mit anderen Detektoren untersucht. Die Zeitauflö-

sung von 48 ps eines einzelnen Zweiges des Detektors wurde im Labor mit einer α-Quelle und niedrigen Raten gemessen. Die Online-Messungen am ESR mit 5 μm Porengröße der MCPs ergaben eine Zeitgenauigkeit von 48 ps mit einem stabilen ^{20}Ne - Strahl und 45 ps mit Uranspaltungsfragmenten. Diese Messungen wurden bei einer kinetischen Energie der Sekundärelektronen von 700 eV durchgeführt.
Zudem wurde der Aufbau des TOF-Detektors fortwährend zur Verbesserung der Transportzeit der Sekundärelektronen für höhere Werte der elektrischen und magnetischen Felder aktualisiert. Eine verbesserte Standardabweichung von 37 ps erhält man mit 10 μm Kanaldurchmesser der MCPs und mit einer zweimal erhöhten kinetischen Energie von 1400 eV der Sekundärelektronen. Der mögliche Beitrag Elektronenausbeuten aus verschieden Foliendicken (10-37$\mu g/cm^2$) wurde ebenfalls untersucht. Nachweislich verbessert die Benutzung dickerer Kohlenstofffolien nicht wesentlich die Zeiteigenschaften. Hieraus leitet sich ab, dass $10\mu g/cm^2$ das Optimum für die gesuchte Stärke der Kohlenstofffolien in Hinblick auf eine Verbesserung bei Effizienz und Zeiteigenschaften darstellt. Jedoch kann durch Verwendung eines anderen Materials die Anzahl der Sekundärelektronen um den Faktor 10 gesteigert und die Zeitgenauigkeit zu σ_{branch}=27 ps (K=1400 eV) verbessert werden.
Zudem wurde ein neuartiges Anoden-Design für den MCP-Detektor konstruiert, um die Zeitmessung für die MCP-Signale zu optimieren. Letztendlich konnten Verbesserungen durch eine zweifach verkleinerte Signalbreite und ein Gewinn von etwa 20% in der MCP-Anstiegszeit erzielt werden. Die Signalform des MCP-Detektors beeinflusst die exakte Bestimmung der Umlaufzeit der gespeicherten Ionen und somit auch die erreichbare Massengenauigkeit.
Aufgrund der hohen Umlauffrequenzen der Ionen im ESR ($\sim$2 MHz) ist ebenfalls eine hohe Ratenfestigkeit des Detektors erforderlich. Während der Offline-Messungen wurde der Sättigungseffekt mit Hilfe von 10 μm und 5 μm Kanaldurchmessern der MCPs untersucht. Erfreulicherweise konnte die Ratenfestigkeit des MCP-Detektors um den Faktor 4 aufgrund der größeren Anzahl an Kanälen der Mikrokanalplatten mit 5 μm Porengröße verbessert werden.
Bei jedem Umlauf im ESR verlieren die Ionen Energie beim Durchqueren der Folie. Gemäß den Simulationsrechnungen führt eine Verringerung der Foliendicke um die Hälfte zu einer in etwa doppelten Anzahl an Ionenumläufen im Ring. Zum längerfristigen Speichern von Ionen im ESR wurde eine dünnere Kohlenstofffolie [10 $\mu g/cm^2$] und MCPs mit einem 5 μm Kanal-Durchmesser im TOF-Detektor installiert. Danach wurden diese zum ersten Mal in Online-Experimenten verwendet.

Die Ergebnisse aus den Messungen mit $^{20}Ne^{10+}$ Strahlen und Uranspaltfragmenten wurden mit den Resultaten vorausgegangener Experimente verglichen, in denen Kohlenstofffolien mit einer Dicke von [17 $\mu g/cm^2$], beidseitig mit CsI beschichtete Kohlenstoffolien [10 $\mu g/cm^2$] und MCPs mit einer Porengröße von 10 μm verwendet wurden. Dieses Szenario bedingte einen Energieverlust von 86 keV ($^{86}As^{33+}$, 386.3 MeV/u). Es ergab sich für eine Kohlenstofffolie mit einer Stärke von 10 $\mu g/cm^2$ ein berechneter Energieverlust von 31 keV, was einem 2.7-fach geringeren Energieverlust als bei dickeren Folien entspricht. Fasst man die Teilergebnisse zusammen, ist zu konstatieren, dass durch dünnere Kohlenstofffolien und höhere Ratenfestigkeit durch MCPs mit einer Kanalgröße von 5 μm im TOF-Detektor bis zu zehnmal mehr Ionenumläufe im Speicherring möglich sind. Nachweislich verbessern erhöhte Umlaufzahlen im Speicherring die Nachweiseffizienz und die Genauigkeit in der Massenmessung. Obwohl die Messzeit im Experiment stark limitiert war (ca. 7 Std.), konnten die gemessenen Ionen aus dem Online-Experiment mit ^{238}U eindeutig identifiziert wurden und mit entsprechenden Daten aus vorangegangen Experimenten verglichen werden.

Contents

Chapter 1

Introduction

1.1 Motivation for Mass Measurements of Exotic Nuclei

All existing atoms can be identified according to their mass value. The mass of the atom is mainly concentrated in its nucleus, which consists of two types of fermions: protons and neutrons. The interest in nuclear masses is due to the fact that the mass $M(Z, N)$ of a neutral atom with Z number of protons and N number of neutrons is measurably less than the sum of the masses of its constituent free nucleons and bound electrons. Therefore a direct determination of the binding energy B of the nucleus is possible:

$$M(Z, N) = Z \cdot (m_p + m_e) + N \cdot m_n - BE_{electron} - BE_{nuclear}, \qquad (1.1)$$

where m_p, m_n and m_e are the rest masses of a proton, a neutron and an electron, respectively. BE_{electron} and BE_{nuclear} are an electron and nuclear binding energies, respectively. Therefore, the mass of the atom reflects all interactions between the fermions and thus carries an important information on the strong, weak, and electromagnetic interactions.

In the last decades, new techniques, applied in nuclear physics experiments have allowed the exploration of nuclei far away from the region of beta-stability and their mass measurements have already contributed to our understanding not only of nuclear structure but also of several other fields of physics. Present investigations are focused on the more exotic nuclei aiming to those at the proton and neutron drip lines. Here one enters the area of unexplored ground where reliable theoretical extrapolations are hardly be made due to the poor accuracy.

Mass differences give an important information in nuclear structure, such

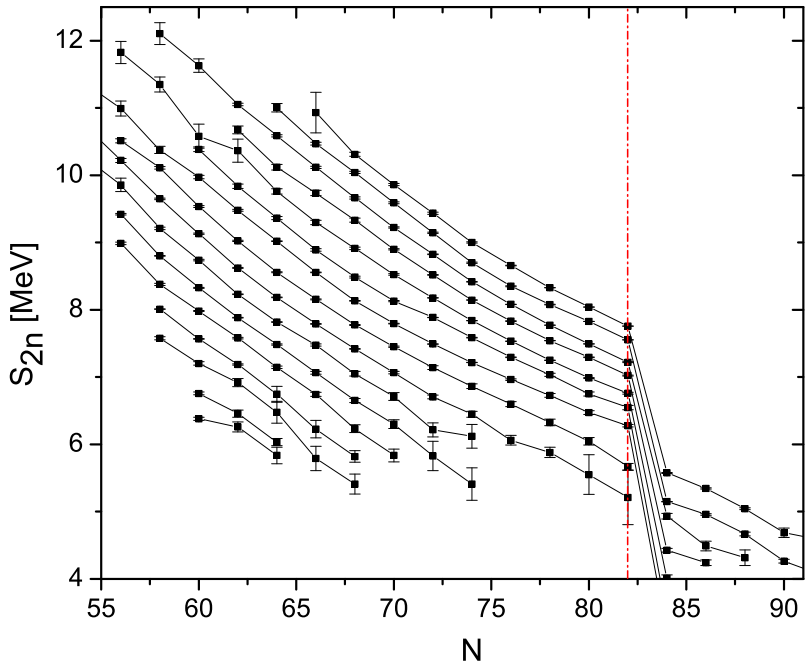

Figure 1.1: Experimental two-neutron separation energy of several elements in the range of Z ∼41-56 as a function of the neutron number N. The drop of separation energy at N=82 is indicated with dash-dotted line. Data are taken from [Aud 03].

as a paring gap, halo-effect [Tan 85], separation energies and other phenomenon. For instance, the most obvious way to observe a shell structure in mass systematics is through the two-neutron separation energy

$$S_{2n}(N,Z) = B(N,Z) - B(N-2,Z) \tag{1.2}$$

in case of neutron shells. The general tendency for the S_{2n} in an isotopic chain is to fall steadily as the neutron number N increases [Lun 03]. But, at the magic numbers there is a drop of the separation energy. After this drop the fall of the separation energy continues. This phenomenon is illustrated in Figure 1.1, where the variation of S_{2n} with neutron number for the elements $Z \sim$ 41-56 is shown. At the neutron magic number N=82 a drop of separation energy is indicated with dash-dotted line. There are still questions present of whether there might be new magic numbers and whether the traditional magic numbers, which were discovered mainly based on the nuclei close to stability line, will remain in neutron-rich or proton-rich regions of the cart of nuclei and new mass measurement experiments plays

one of the major role to explore those nuclei.
Meanwhile, a knowledge of precise nuclear masses, involved in a certain reaction or other processes such as beta decay or fission, is essential for determination of Q - value released.
The needs of the astrophysics community are one of the major goal for the current growth of activity in the field of nuclear masses [Lun 03]. Because of difficulties in production, the masses of the nuclei lying further and further away from the stability line, are still not measured. But many of these nuclei with unmeasured mass play an important role in the stellar nucleosynthesis of heavy elements, and investigation of these processes requires a knowledge of the masses of all nuclei involved. The problems are especially exacerbated in the case of heavy, highly neutron - or proton - rich nuclei, that are involved in the r-process (rapid neutron capture) and rp-process (rapid proton capture) of nucleosynthesis. Although in case of rp-process the problem is less acute since the available mass measurements fill bigger area towards the proton drip line than to the neutron drip line.
The nuclear masses are intended in multiple computations in different fields, at different levels of accuracy [Lun 03] [Bla 06] [Fra 08]. It is clear that at a certain field of physics the mass values can contribute only at a relatively good accuracy. For the application in nuclear physics and astrophysics accuracy of $\Delta m/m \approx 10^{-6} - 10^{-7}$ or better is sufficient. For fundamental physics application, like weak interaction the limit of about $\Delta m/m \approx 10^{-8}$ is required.

1.2 Production and Separation of Exotic Nuclei

The very first step for exotic nuclei mass measurement experiments is production of the nuclei and their efficient separation.
In principle the beams of exotic nuclei can be produced as a result of many nuclear reactions, depending on the energy regime, primary intensity, target thickness, production cross sections of specific nucleus. The desired nuclei are produced together with high amount of other reaction products and an important task is to separate them efficiently in short time due to the small half-lives.

1.2.1 Production of Exotic Nuclei

The dominant processes for production of secondary exotic beams are projectile nuclei fragmentation, fission and fusion. In Figure 1.2 the chart of nuclei is shown with indicated areas where ceratin reactions dominate for

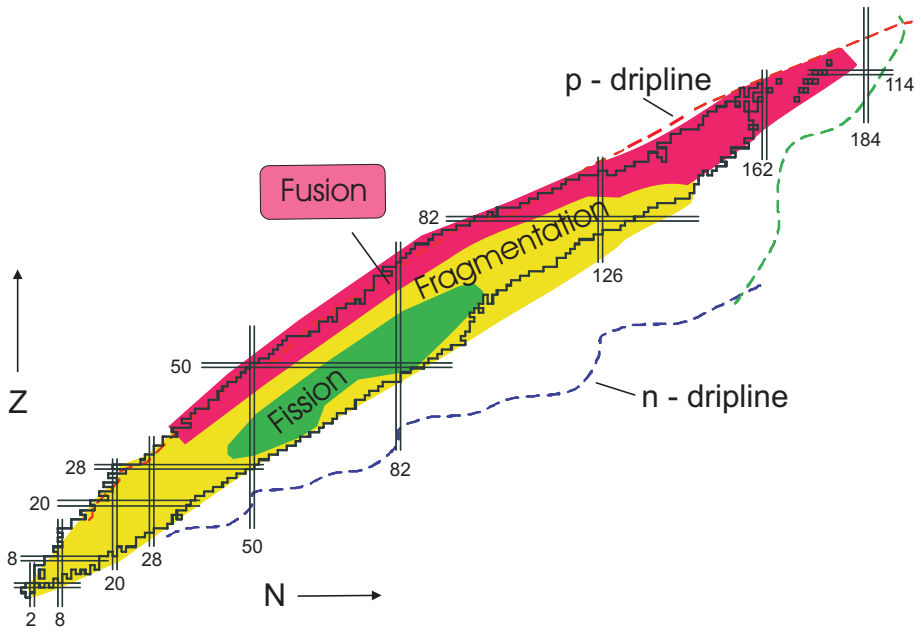

Figure 1.2: Chart of nuclei with indicated regions of predominant type of reactions for the production of certain nuclei.

the nuclear production. At the lower energies of the projectile close to the Coulomb barrier fusion reactions can take place. If the kinetic energy of the projectile is enough to overcome the Coulomb barrier of the target nuclide, they fuse into a single heavier nucleus. The projectile transfers the full momentum to the fusion products and they are the only reaction products that recoil from the target with center-of-mass velocity

$$v_f = \frac{A_p}{A_p + A_t} \cdot v_f, \tag{1.3}$$

where v_p and v_f are the velocities of the projectiles and fusion product, respectively. The fusion products are emitted in a forward direction with a well-determined velocity. The principle of kinematics in fusion reaction is shown on the top of Figure 1.3.

Secondary ion beams with energies above the Coulomb barrier ranging to the relativistic region are produced by projectile fragmentation or by fission.

In fragmentation reaction, the primary heavy projectile usually impinges the thick target consisting of lighter elements. In the collision of projectile with a target a part of the projectile nucleons is removed by abrasion and so called prefragment is produced in excited state. This prefragment finally deexcites and via ablation produces other fragments. The velocity of projectile fragments are equal to the projectile velocity $v_f \approx v_p$. The energy distribution of the fragments produced in such reaction is a few percent and

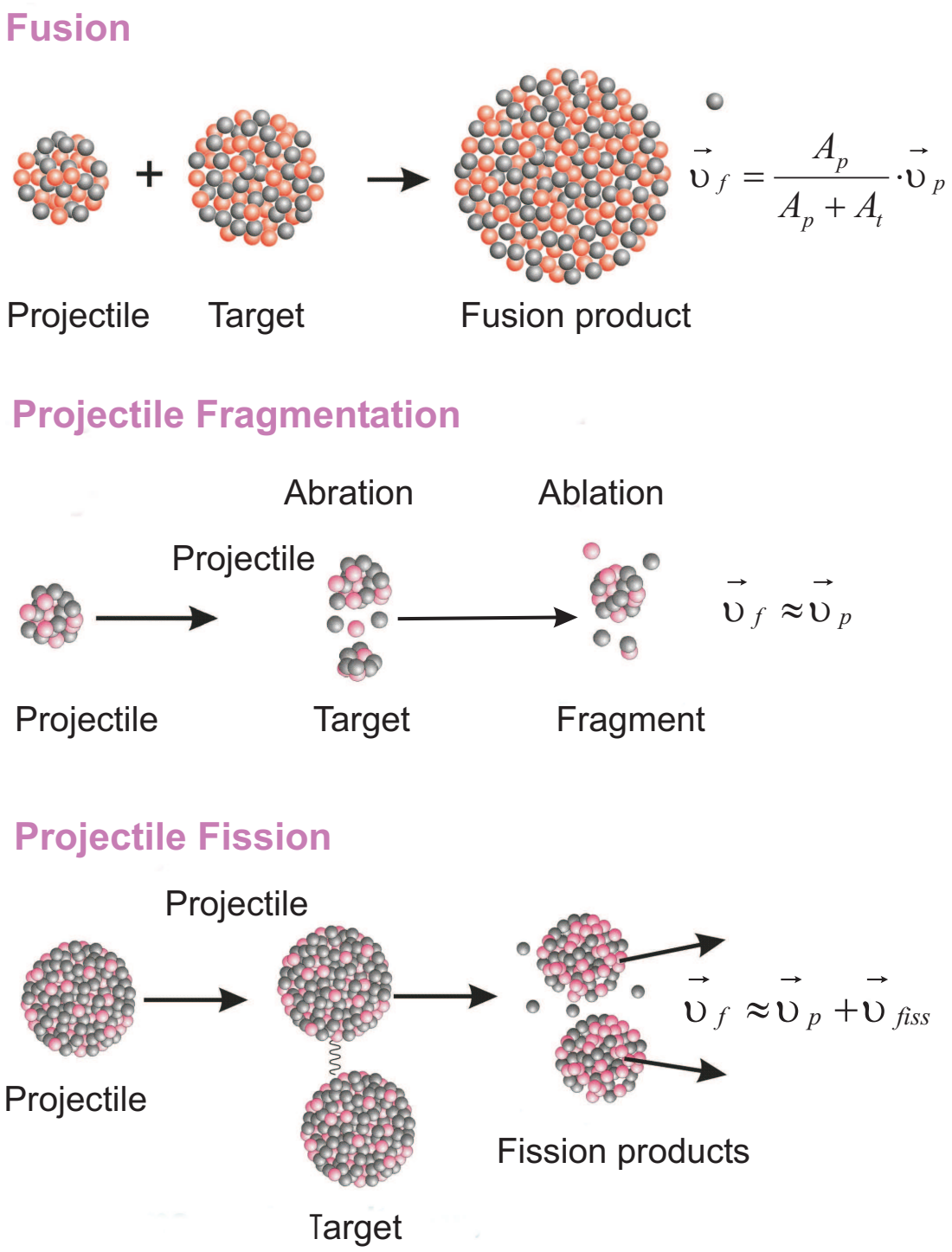

Figure 1.3: Schemes of main nuclear reactions for the production of exotic beams [H. Geissel, private communication]. If the projectile has enough kinetic energy to overcome the Coulomb barrier of the target nucleus they can fuse into a single heavier nucleus. In this reaction the projectile transfers the full momentum to the fusion product. In the projectile fragmentation the part of the projectile nucleus is removed by abrasion, formed prefragment in excited state which later deexcites and via ablation produces other fragments. The velocity of fragment is equal to the projectile velocity. In the projectile fission, projectile splits into two main fission products. The energy of the products is higher than the kinetic energy of the projectile.

depends on the number of nucleons removed from the projectile.
In a fission reaction a projectile splits into fragments with symmetric or asymmetric mass distribution depending on the impact parameter of the collision. The fragments leave the target with higher kinetic energy as projectile's energy $\upsilon_f > \upsilon_p$. At large impact parameters the fission of a parent nucleus at low excitation energies produces two group of fragments: the heavy group and the light group. The centroid mass of this asymmetric fragment distribution is almost identical for different parent nuclei and is around doubly magic ^{132}Sn. The asymmetry of fission fragment distribution is a quantum mechanical effect related to the shell closures and quantified by shell correction energies. At high excitation energy of the projectile the shell effects are breaking and the prefragment fissions into two fragments of similar masses. So the mass distribution of produced fragments is symmetric. This is the case for small impact parameters, when nuclear collisions between the projectile and the target nucleus occur [NUC 11].

1.2.2 ISOL Separation Technique

Isotope-Separation-On-Line (ISOL) technique was developed to complement the nuclear chemistry tools [Her 69] for short-lived nuclei far away from stability. In ISOL separation method the radioactive nuclei produced in a nuclear reaction are stopped in a thick target, then transported by diffusion processes from the target to an ion source for ionization, accelerated to the typical levels of 10-100 keV and separated according to the mass-to-charge ratio (m/q) electromagnetically. This method is applied for example in such world wide known facilities like ISOLDE at CERN (Geneva) [Hag 92] and ISAC at TRIUMF (Vancouver) [Bri 02].
The main steps of the ISOL method are shown in Figure 1.4. The ion beam is impinging on the thick target and the exotic nuclides are produced via the fragmentation or fission. During the diffusion through the target the nuclides are thermalized. After leaving the solid target thermalized nuclides are transported to the ion source and ionized.
After that the ions are extracted from an ion source and accelerated through a static electric field to a kinetic energies up to tens of keV and separated according to their mass-to-charge ratio in an electromagnetic field.
A disadvantage of the ISOL technique is efficiency of extracted ions compared to the number of produced in the target. It is difficult to predict this ratio because it strongly depends on the chemical and solid state properties of the target, that is element dependence of the release from the target and ionization efficiency. The other disadvantage is that this method is not ap-

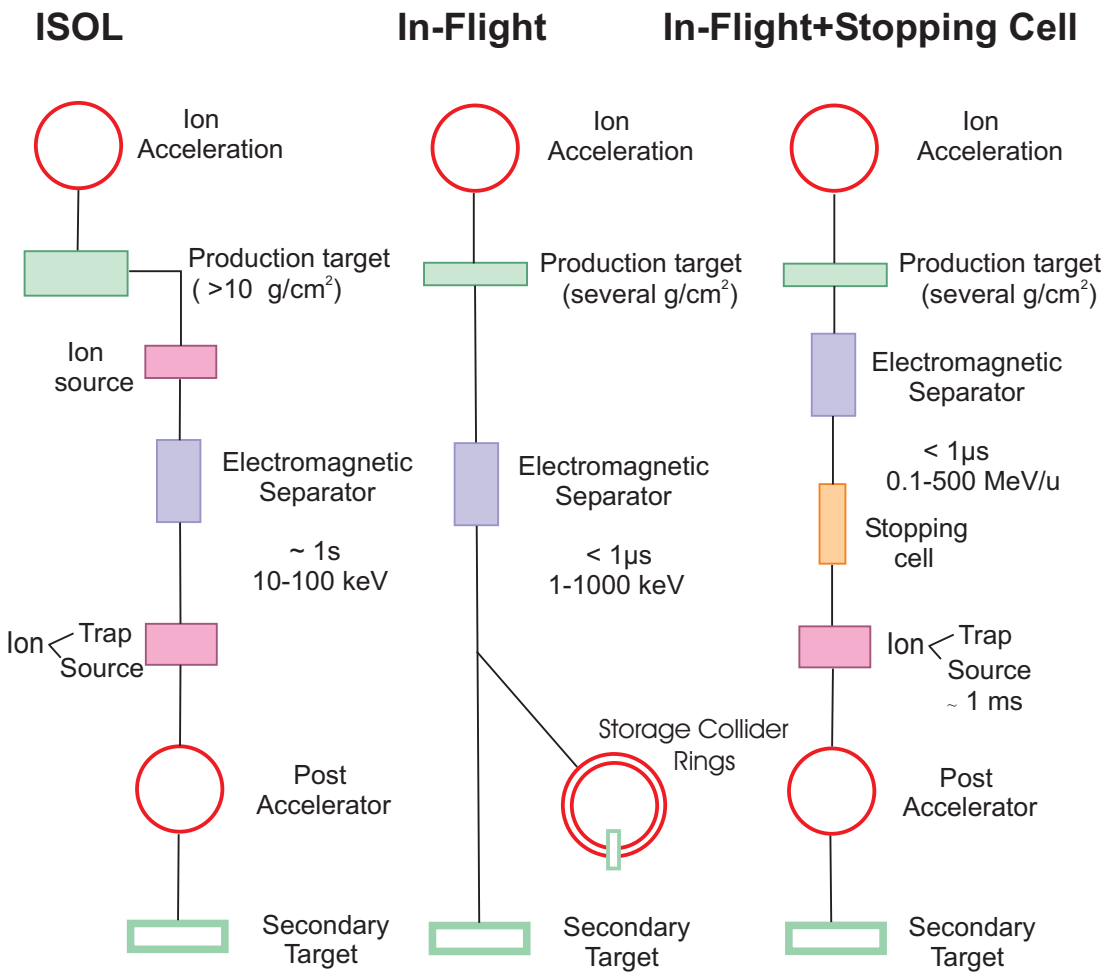

Figure 1.4: Comparison of the methods for the production and separation of secondary nuclear beams: the ISOL, In-Flight technique, combination of In-Flight method and Stopping Cell [Gei 95].

plicable to very exotic nuclei. Due to the rather slow diffusion process, the ISOL system is limited to the nuclides lifetimes longer that 10 ms, depending on the chemical and solid-state characteristics of the reaction products [Gei 95].

1.2.3 In-Flight Separation Technique

An alternative separation method is an In-Flight separation. The target used for production of exotic nuclei in an In-Flight method is thinner than in ISOL facility and reaction products have therefore higher energies when they enter an ion-optical system. In Figure 1.4, the principle of In-Flight method is compared with the ISOL technique.

The separation is made by an ion-optical system, for example like FRagment Separator (FRS) at GSI [Gei 92]. The separation is performed with electric and magnetic fields. The combination of electric and magnetic fields is used

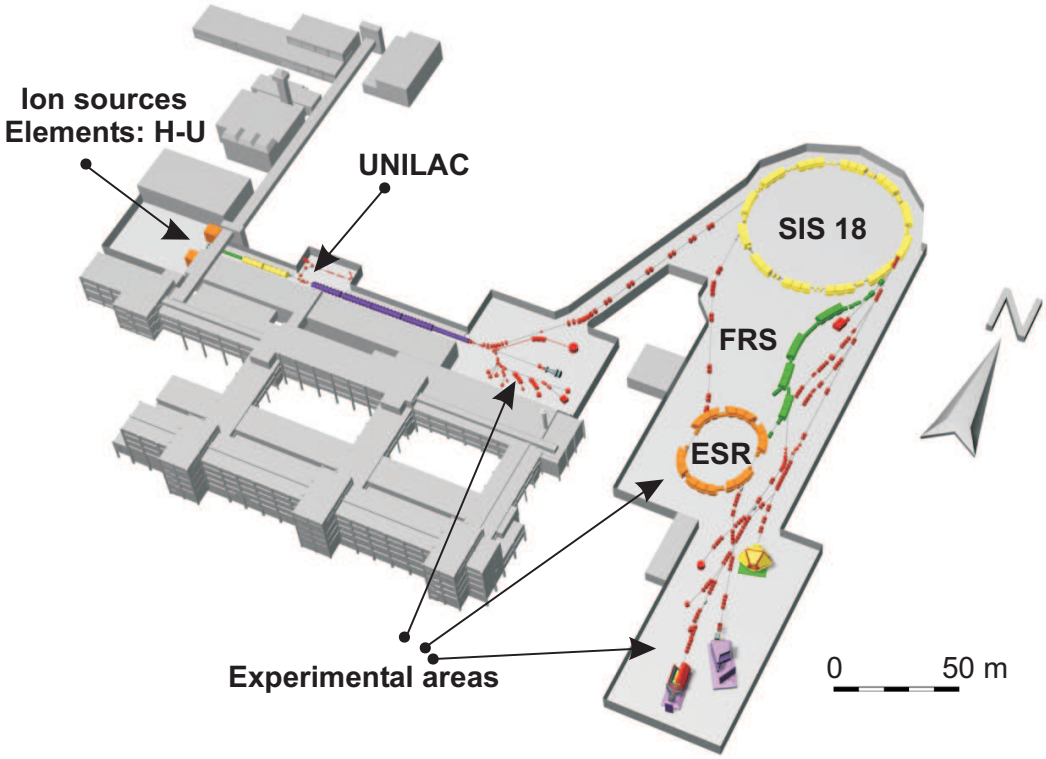

Figure 1.5: The layout of the high-energy radioactive beam facility at GSI [GSI]. The stable primary beams are accelerated by the linear accelerator UNILAC to an energy of 11.4 MeV/u. The heavy ion synchrotron SIS accelerates the ion beams up to a maximum rigidity of 18 Tm. The fragment separator FRS separates in-flight radioactive isotopes produced in the production target and transports the nuclei to three main experimental areas.

only up to medium energies. At relativistic energies due to the technical limitations only the magnetic field is applied.
A major advantage of the In-Flight technique is that it does not include diffusion process or ionization as it takes place in ISOL technique and so it can perform separation of a secondary beam with half-lives shorter than microseconds. The limitation in nuclei half-lives is determined by the time-of-flight through the electromagnetic separator and is independent of the chemical property of the selected element.

1.2.3.1 The Fragment Separator FRS at GSI

The high-energy secondary beam facility at research center GSI, where the present work has been performed is based on the in-flight technique. Schematic view of the main components is presented in Figure 1.5. All stable primary beams from protons up to uranium can be accelerated firstly by the UNIversal Linear ACcelerator (UNILAC) to the energy about 11.4

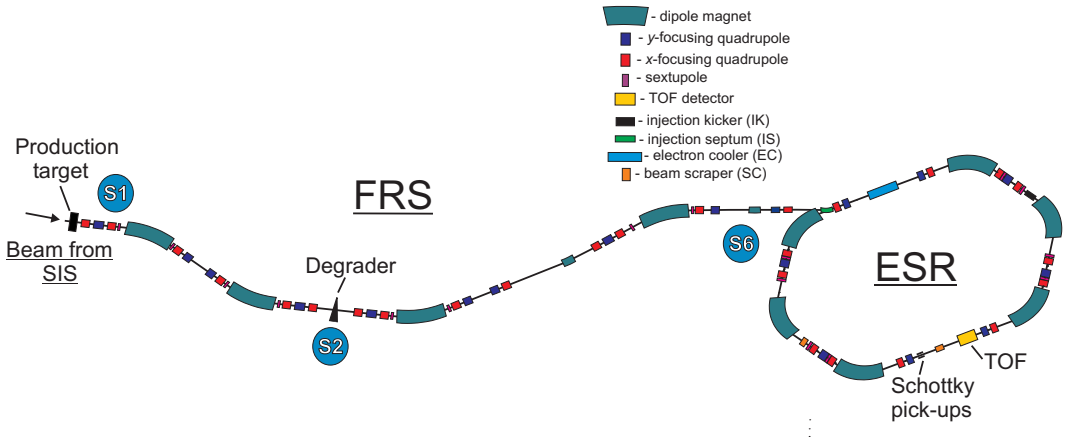

Figure 1.6: Layout of the FRS with main focal planes and ESR with main tools for the mass measurement experiments [Lit 08]. At first focal plane S1 the thick target is located for the production of radioactive secondary beams, at central dispersive focal plane S2 a degrader is installed for separation of selective nuclei from all other reaction products, at the final focal plane S6 the beam is spatially separated before the injection into the ESR.

MeV/u and further with heavy ion synchrotron SIS [Bla 92] up to a maximum magnetic rigidity of 18 Tm.
A secondary nuclear beam can be produced in the thick [typically 1-8 g/cm^2] Be target at the entrance to the FRS [Gei 92]. Fragment Separator is an in-flight magnetic forward spectrometer and is used for efficient separation of radioactive isotopes. The location within the SIS and the Experimental Storage Ring (ESR) complex was determined by the requirement of using the FRS in combination with both instruments. FRS can be described as two stages, each of them consists of two bending dipole magnets, a set of quadrupoles and sextupoles correction magnets before and after the dipole to fulfill first-order focusing conditions. The layout of FRS is shown in Figure 1.6.
The separation of heavy ions by the FRS can be divided into three steps. At the first one produced nuclides are separated according to their momenta with dipole magnets surrounded by the focusing quadrupole lenses. Consequently only the ions with the same m/q ratio are transported to the central dispersive focal plane S2.
The separation of ions with similar mass-to-charge-ratio but different charge numbers Z can be performed exploiting their atomic interactions with matter. This is realized in practice with a special shaped energy degrader placed in the middle focal plane S2 of the FRS. The ions penetrating through the degrader loss their energy proportional to Z^2 [Bet 30] and therefore the nuclides with the same momenta/magnetic rigidity before the degrader but

different proton number Z will have different momenta after it and can be separated.
During the next step, the ions behind the degrader again are separated in-flight according to their momenta using dipole magnets and set of quadrupole lenses. Now, the nuclides with the specific values of mass and charge can be separated at the final focal plane S4.
So, after the nuclides produced at the FRS, the specific nuclide can be selected from all other reaction products by the combination of ionization energy loss and magnetic rigidity analysis, i.e. $B\rho$-ΔE-$B\rho$. For the mass measurement experiments the selected fragments at S6 are injected into the ESR.

1.2.3.2 FRS + Stopping Cell

In the case of combination of In-Flight and ISOL techniques [Gei 95], the advantages of both methods such as high selectivity, element-dependence, short production time (∼10 ms), as well as low kinetic energy (a few 10 keV) and small emittance (a few π mm mrad) of post accelerated beams can be achieved [Pet 08].
This method was successfully applied in an experiment at the FRS Ion Catcher at GSI [Pet 08]. The main principle of combination of In-Flight method with an ion catcher is presented in Figure 1.4. The exotic nuclei after their production and separation in-flight according to $B\rho$-ΔE-$B\rho$ method at the FRS are stopped in a gas cell, then extracted and transported to the low-energy experiments.
The FRS Ion Catcher is a prototype for a gas cell system at the Low-Energy Branch of the future Super-FRS [Gei 03] at FAIR.

1.3 Mass Measurements of Stored Ions

In 1912 the English physicist J.J. Thomson, together with his assistant F.W. Aston discovered the existence of isotopes and performed first separation of neon isotopes according to their masses. It was the first example of the mass spectrometry. Later, the resolving power of the method was improved and the general method of mass separation was developed by F.W. Aston.
The methods of mass measurements are usually divided into two groups: direct and indirect methods. Most direct mass measurement techniques are based on the measurement of quantities proportional to the mass-to-charge ratio (m/q) of the ions. Either time-of-flight is measured through a magnetic spectrometer (SPEC at GANIL), or their cyclotron frequency

in a Penning traps (e.g. ISOLTRAP at ISOLDE [Bol 96], JYFLTRAP at IGISOL [Ays 01], SHIPTRAP at SHIP [Dil 01]), in a storage ring (ESR at GSI; CSR at Lanzhou [Lit 10]) or in a RF spectrometer.

1.3.1 Penning Traps

Direct mass measurements can be performed by Penning trap mass spectrometry by cyclotron frequency measurement of an ion in a magnetic field. There are several facilities worldwide which applied this technique. For example ISOLTRAP at ISOLDE (CERN) [Bol 96] [Her 03], the Canadian Penning trap (CPT) [Sav 06] at the Argonne National Laboratory ANL, the JYFLTRAP facility at IGISOL in Jyväskulä [Ays 01], LEBIT [Rin 06] at NSCL (MSU) and TITAN [Dil 06] at TRIUMF (Vancouver) perform the measurements with an accuracy of typically 10^{-7}. Another facility is SHIPTRAP [Blo 07], which is developed for the mass measurements of superheavy elements at the velocity filter SHIP at GSI.
In Penning traps an axial homogeneous magnetic field confines the ions radially and a quadrupole electric field confines the ions axially. The trajectory of a stored ion consists of three independent harmonic modes with the corresponding magnetron ν_-, modified cyclotron ν_+ and axial frequency ν_z. The layout of the Penning trap as well as a three directional motion is shown in Figure 1.7.
The cyclotron frequency ν_c can be determined from the motion of the ion with charge q and mass m_{ion} in a homogeneous magnetic field B as

$$\nu_c = \frac{1}{2\pi}\frac{q}{m_{ion}}B, \tag{1.4}$$

where $\nu_c = \nu_+ + \nu_-$. For the needs of nuclear physics precise mass measurements at Penning traps can be performed using TOF-ICR method. This method is based on the measurement of a time-of-flight resonance curve, from which the cyclotron frequency can be determined and according to eq. 1.4 the mass-to-charge ratio of the ion.
To improve the beam quality the ions are injected into a radio-frequency quadrupole (RFQ) cooler/buncher where the ions are decelerated and cooled by collisions with the buffer gas. Then the ions are released in bunches and transferred into the first trap, where they are cooled with helium gas and isobarically separated. Afterwards the ions are transferred into the second trap for the mass measurements. When the ions are captured in the second trap, the magnetron radius is increased by dipole excitation. Then by applying a quadrupole excitation at the ions's frequency the magnetron motion is converted by cyclotron motion, which results in a gain in radial

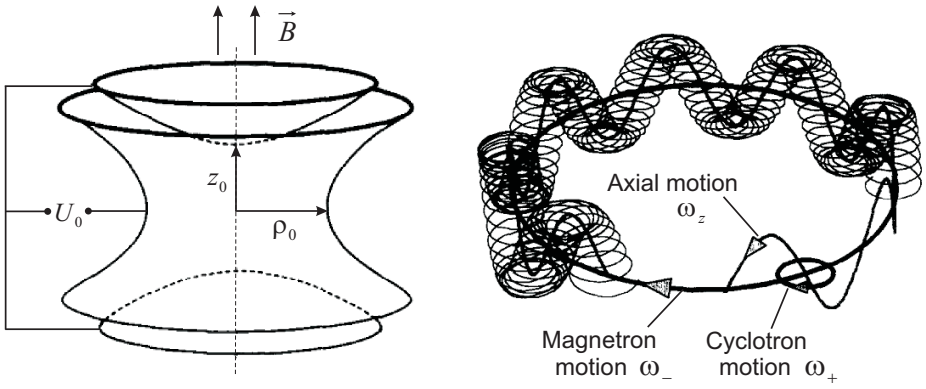

Figure 1.7: Layout of a Penning trap [Bol 96]. ρ_0 denotes the inner radius of the ring electrodes and z_0 the half distance between the endcap electrodes. On the right part the schematics of a three eigenmotions (characterized by frequencies ν_z, ν_- and ν_+) of an ion in a Penning trap is shown.

energy of the interested ions [Hag 07a].
Before describing the ejection of the ions one has to mention that the movement of the charged particle on the closed orbit is characterized by the magnetic moment, which depends on the m/q ratio, the gyromagnetic ratio and angular momentum. After excitation the ion has higher magnetic moment. Directly after ejection the ion passes through an inhomogeneous region of the magnetic field and accelerates towards the microchannel plate detector. The radial energy increase of the ion is detected by measuring the time-of-flight to a microchannel plate detector. By scanning through different quadrupole excitation frequencies, a time-of-flight spectrum for the ion can be obtained. Typically a few hundreds of ions per resonance are used. The disadvantage of this method is the measurement time of about 1 second, that limits the measurement for very exotic nuclei with lifetimes shorter than a second.

1.3.2 Ion Storage Rings

There are only two storage ring facilities worldwide which use high energy storage rings for accurate mass measurements [Lit 10]. The first experimental ring ESR [Fra 87] for this purpose was constructed at GSI, Darmstadt. The GSI facility is described in Sec. 1.2.3.1.
The second storage ring has been developed at IMP, Lanzhou. The acceleration of heavy ions with the synchrotron CSRm, separation of nuclides via in-flight method by fragment separator RIBLL2 and storage of ions in the ring CSR is done in the similar principle as at GSI [Xia 02] [Xia 09].
Two complementary experiment techniques namely Schottky (SMS) and

Isochronous Mass Spectrometry (IMS) have been developed at GSI for accurate mass measurements [Fra 08] and have been successfully used in several experiments [Wol 97] [Hau 00] [Rad 00] [Lit 05] [Kno 08] [Sun 08a]. The masses of the exotic nuclei are determined from the revolution frequencies (eq. 2.10) measured by Schottky pick-ups or by Time-of-Flight (TOF) detector. Both methods are non distractive. Overview of main characteristics for both methods can be found in [Sun 08b] [Lit 10].

1.3.2.1 Schottky Mass Spectrometry

In Schottky Mass Spectrometry [Fra 87] the velocity spread of the injected and stored ions are reduced by electron cooling [Ste 04] situated in one of the straight section of the ESR. In the cooler an electron beam with a well defined velocity is merged by the Coulomb interactions to the velocity of the electrons. After many passages through the cooler the ions achieve the relative velocity distribution of about $dv/v = 1 \cdot 10^7$. The magnetic rigidity according to eq. 2.7 depends on the mass-to-charge ratio and the velocity. For cooled ions, when $dv/v \rightarrow 0$ the second term in eq. 2.10 can be neglected. The electron cooling leads to ions with different mass-to-charge ratios and the same velocities v have different orbits and, consequently, different revolution frequencies. Operation of the ESR at standard mode for SMS with main explanation of the method is shown in Figure 1.8. Typical revolution frequency at the ESR is about 2 MHz. At each revolution, each stored ion induces a mirror signal on the Schottky pick-up probe installed inside the ESR. Masses are determined from the revolution frequencies which are obtained by a Fourier transformation of the signals induced in pick-up probes. Moreover the intensity of the frequency peak is proportional to the number of stored ions. This allows half-life measurements.
The electron cooling time limits the SMS method, the mass measurements of the nuclides with half-lives exceeding few seconds.

1.3.2.2 Isochronous Mass Spectrometry

Isochronous Mass Spectrometry technique does not require any kind of cooling and is, therefore, suited for the precision mass measurements of nuclides with short half-lives up to tens of microseconds. For IMS the ring is operated at special isochronous ion-optical mode. In this mode the ions are injected into the ESR with $\gamma = \gamma_t$. The detail explanation is in Sec. 2.2. When this isochronous condition is fulfilled the term containing the velocity spread in eq. 2.10 equals to zero. This means that the revolution time of the reaction products with a given mass-to-charge ration is independent on the

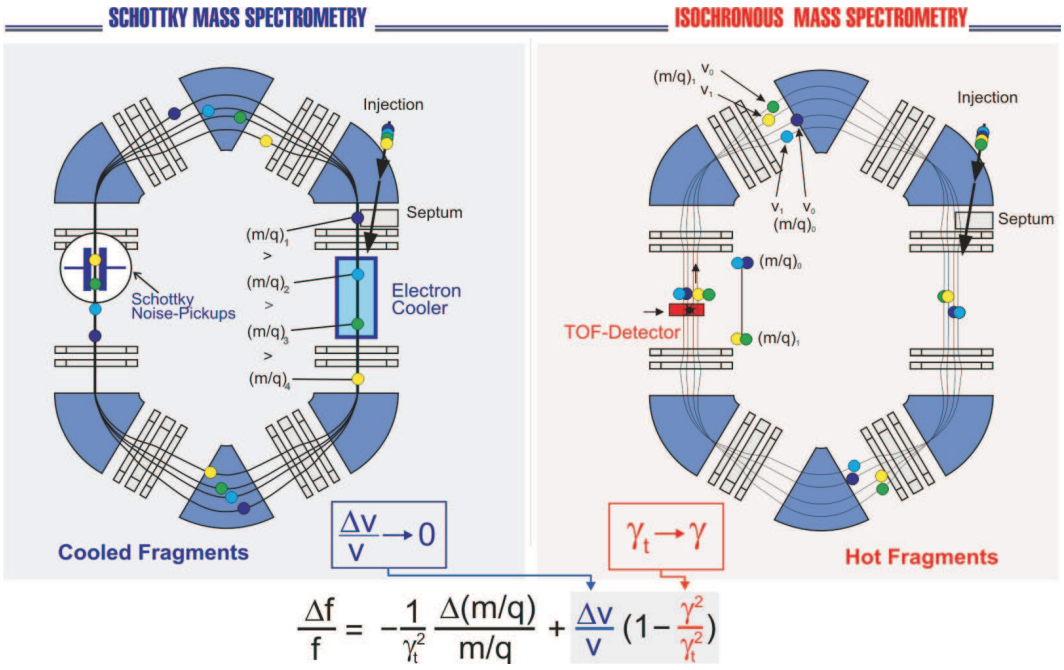

Figure 1.8: Comparison between two experimental methods for mass spectrometry [Bos 03]. On the left part the Schottky Mass Spectrometry technique is explained. While the velocity spread of the ions is reduced by electron cooling and $\Delta v/v \rightarrow 0$ right term in eq. 2.10 can be neglected. Alternatively, in Isochronous Mass Spectroscopy technique shown on the right part, the ions are injected into the ESR with $\gamma = \gamma_t$ (eq. 2.11). Thus, the term containing the velocity spread in eq. 2.10 equals to zero. The revolution frequencies are measured by Schottky pick-ups in SMS and by Time-of-Flight detector in IMS.

velocity spread. Here the revolution frequencies of each individual stored ion are measured by a microchannel plate time-of-flight detector (Sec. 2.5). The IMS method is compared to the SMS technique in Figure 1.8.
By this isochronous mass spectrometry one single stored ion can be easily detected, independently from its charge state. IMS gives access to nuclides with half-lives down to tens of microseconds with mass accuracy in the order of 10^{-6}.

Chapter 2

Isochronous Mass Spectrometry at the FRS - ESR

As it was mentioned in Sec. 1.3.2.2 the mass measurements of exotic nuclei with half-lives as short as few tens of microseconds can be performed with Isochronous Mass Spectrometry. IMS has successfully applied in the experiments at the ESR [Mat 04] [Kno 08] [Sun 08b].
In this method a cocktail of highly-charged ions is injected into the ESR operated in special isochronous ion-optical mode. This mode leads to a faster ion of one species to move on a longer orbit and slow ion of the same ion species to move on a shorter orbit, so that the spread in the ion velocities is exactly compensated by the length of the closed orbits. Hence, the revolution frequency of the circulating ions does not depend on their velocity spread [Hau 00], i.e. they become isochronous. The mass of the exotic nuclei can be deduced from a precise revolution time measurements by a time-of-flight detector placed in the ESR. The TOF detector is described in more detail in Sec. 2.5. Isochronous Mass Spectrometry allows the mass measurements of the exotic nuclei with an accuracy of 100 keV and mass resolving power of about $2 \cdot 10^5$ [Sun 08b].
In order to gain knowledge from overall process of mass measurements each step in the measurements, i.e. motion of charged particles in the electromagnetic field, the principle of isochronous ion-optical mode of the ESR, characteristics of TOF detector, creation of secondary electrons, transport of secondary electrons inside the TOF detector and their detection by the MCP detector must be characterized and examined independently. Main physical phenomenon related to those processes will be discussed in this chapter.

2.1 Motion of Charged Particles in Electromagnetic Field

In an electromagnetic field $(\vec{E}, \vec{B})$ a charged particle experiences a Lorentz force given by

$$\vec{F} = \frac{d\vec{p}}{dt} = q\vec{E} + q\vec{v} \times \vec{B}, \tag{2.1}$$

where q, $\vec{p}$ and $\vec{v}$ are the charge, momentum and the velocity of the particle, respectively. From this equation, individual trajectories of the particles can be calculated for a given field, initial coordinates and velocities.
In a radial electric or in a constant magnetic field, a charged particle travels on a circular path that has a radius ρ. The radius ρ of the circular trajectory can be characterized by magnetic

$$B\rho = \frac{p}{q} \tag{2.2}$$

and the electric

$$E\rho = \frac{pv}{q} \tag{2.3}$$

rigidities. The terms from these equations have already explained in eq. 2.7. From eq. 2.2 and 2.3 it is obvious that the magnetic sector acts as a momentum analyzer, and disperses each ion according to its momentum-to-charge ratio, while the electric field disperses the ions according to their kinetic energy. Thus, the electric sector can be used as an energy filter to produce an ion beam of nearly homogeneous energy [Das 07].
However, the combination of electric and magnetic field is valid to mass times acceleration only at low velocities. At relativistic velocities ($v \approx$c) the required electrical fields would exceed the present technical limitations. Therefore, mainly magnetic fields are applied for guiding and focusing the particle beams.

2.2 Isochronisity Condition

The revolution time of an ion with a mass m and charge q stored in the ESR is about 500 ns. It depends on the velocity v of the ion and the path length L as

$$T = \frac{L}{v}. \tag{2.4}$$

By differentiation of this equation the change of the revolution time or the frequency with change of the path length or the velocity of the ion can be obtained

$$\frac{dT}{T} = \frac{\partial T}{\partial L}\frac{dL}{T} + \frac{\partial T}{\partial v}\frac{dv}{T} = \frac{dL}{vT} - \frac{dv}{Tv^2} = \frac{dL}{L} - \frac{dv}{v}. \tag{2.5}$$

The path length of the ion in the magnetic field depends on the magnetic rigidity as [Bry 93]

$$\frac{dL}{L} = \alpha_p \frac{d(B\rho)}{(B\rho)} \tag{2.6}$$

with α_p is a momentum compaction factor that describes the change in the path length of an ion by changing the magnetic rigidity. The magnetic rigidity of a particle is given by

$$B\rho = \frac{p}{q} = \frac{m}{q}\beta\gamma c, \tag{2.7}$$

where p is a momentum, $\gamma = \frac{1}{\sqrt{1-\beta^2}}$ is a relativistic Lorenz factor and $\beta = \frac{v}{c}$ is an ion velocity according to the speed of light in vacuum c.
If to replace $\frac{dL}{L}$ in eq. 2.5 by eq. 2.6 we will get

$$\frac{dT}{T} = \alpha_p \frac{d(m/q)}{(m/q} + (\alpha_p\gamma^2 - 1)\frac{dv}{v}. \tag{2.8}$$

The transition energy γ_t is defined as

$$\gamma_t = \frac{1}{\sqrt{\alpha_p}}. \tag{2.9}$$

Then

$$\frac{dT}{T} = \alpha_p \frac{d(m/q)}{(m/q)} + (\frac{\gamma^2}{\gamma_t^2} - 1)\frac{dv}{v}. \tag{2.10}$$

Eq. 2.10 shows the main principle of mass measurement technique at the ESR. Thereby the system becomes isochronous with the following condition

$$\gamma = \gamma_t, \tag{2.11}$$

which is called isochronous condition. More detail calculations concerning an isochronous ion-optical operating mode of the ESR can be found in [Lit 08].
At $\gamma = \gamma_t$ the second term in eq. 2.10 vanishes and the revolution time of the ions is independent on their velocities [Wol 97]. An ion-optical mode of the ring is set in such way that faster ion of certain species moves in a longer orbit and a slower ion moves on a shorter orbit. So all ions with the same m/q will travel on the same trajectory and have the same revolution time. Consequently measurements of the revolution times give the possibility to determine the m/q ratio of the circulating ions.
In the Schottky Mass Measurements as it is described in Sec. 1.3.2.1 the velocity spread dv/v can be reduced by electron cooling [Ste 04], which force all stored ions towards the same mean velocity. So the $dv/v \to 0$ and therefore the second term in eq. 2.10 can be neglected. Then the measurements

of m/q reduces to the measurements of revolution times.
In the standard mode of ESR typical γ_t is equal to 2.5. However, for the most ions a gamma of 2.5 would be located outside of the adjustable magnetic rigidity of the ring. Therefore to match storage of more ions the setting changed by adjusting the quadruples in the ring to reduce γ till about 1.4. With this condition almost all nuclides can be stored by the ESR.
Before any isochronous mass measurements take place in the ESR, the isochronisity of the ring has to be tested. The isochronisity is tested with a cooled primary beam. With the help of the electron cooler the velocity spread of the stored ions can be reduced down to $dv/v \approx 5 \cdot 10^7$ [Ste 97]. The maximum electron energy possible in the ESR is 240 keV. By varying the cooler voltage the velocity of the circulating ions is varied. For every value of the cooler voltage the frequency of the ions is measured. In the isochronous mode the dependence of the ion frequency on the velocity drastically decreased. But nevertheless the little change in the revolution frequency has been observed. It is explained by the higher orders of the magnet field corrections.
The isochronicity curve is measured only for the beam of one ion species. In reality it is different for the desired nuclide because of difference in mass-to-charge ration between nuclides. To transform the isochronicity setting to the nuclide of interest, the frequency can be calculated from

$$f_{trans} = f_{meas} \frac{\sqrt{(\frac{(m/q)_{meas}}{B\rho})^2 + \frac{1}{c^2}}}{\sqrt{(\frac{(m/q)_{trans}}{B\rho})^2 + \frac{1}{c^2}}}. \tag{2.12}$$

The isochronicity curve is measured for the mass-to-charge ratio $(m/q)_{meas}$ and transformed to the mass-to-charge ration of interest nuclide $(m/q)_{trans}$.

2.3 Atomic Interaction of Charged Particles with Matter

In this section the energy loss and the contributions to it for the different energy regimes will be presented. Then the angular scattering and the charge-exchange reactions will be addressed.

2.3.1 Energy Loss

The energy loss process for the ions passing though the matter is mainly due to excitation and ionization of the target electrons and charge exchange between the projectile and the target.

The stopping power was first calculated by Bohr [Boh 13] [Boh 15], using classical theory and viewing each collision with atomic electrons independently. For the total energy loss he obtained

$$-\frac{dE}{dx} = \frac{4\pi Z_p^2 e^4}{m_e \upsilon^2} N_e \ln \frac{\gamma^2 m \upsilon^3}{Z_p e^2 \bar{\omega}}, \tag{2.13}$$

with Z_p and υ being a charge and velocity of the projectile, m_e the electron mass, N_e the density of target electrons. Eq. 2.13 presents the classical Bohr formula.

The correct quantum-mechanical calculation was first performed by Bethe, Bloch and other authors. In the calculation the energy transfer is parameterized in terms of momentum transfer. The formula obtained is commonly known as Bethe-Bloch formula and is the basic expression for energy loss calculation [Leo 87]

$$-\frac{dE}{dx} = 2\pi N_a r_e^2 m_e c^2 \rho \frac{Z_t}{A_t} \frac{Z_p^2}{\beta^2} [\ln(\frac{2m_e \gamma^2 \upsilon^2 W_{max}}{I^2}) - 2\beta^2], \tag{2.14}$$

where W_{max} is the maximum kinetic energy which can be transferred to the atomic electron in a single collision, ρ the density of the target material.

Let denote the right part under the natural logarithm in the eq. 2.14 as L_{Bethe}. At the relativistic velocities additional corrections ΔL to the L_{Bethe} have to be added [Sch 94]. One of the correction is $\delta/2$ - *Fermi density effect*. Due to the relativistic effects electric field of the projectile flattens and extends, so that the distant collision contribution to the energy loss increases as $\ln \beta\gamma$. However, real media becomes polarized, limiting the field extension and effectively reduces this part of the logarithmic rise. At very high energies the density effect correction is equal to

$$\frac{\delta}{2} = -\ln(\beta\gamma) + \ln \frac{I}{\hbar\omega_p} - \frac{1}{2}, \tag{2.15}$$

where $\hbar\omega_p$ is the plasma energy.

The theory developed by Lindhard and Sørensen (LS) [Lin 96] based on the relativistic scattering kinematics and Dirac equation incorporates *Mott* and *Bloch* corrections. At the low energies the LS-theory reproduces the *Bloch* correction and at relativistic energies by using the exact solutions to the Dirac equation, the LS-theory automatically incorporates *Mott scattering* [Ahl 78] [Ahl 80] [Sch 94]. In the nonrelativistic limit the *Bloch* correction ΔL_{Bloch} is equal to

$$\Delta L_{Bloch} = \psi(1) - Re\psi(1 + iZ\alpha/\beta), \tag{2.16}$$

where ψ is the logarithmic derivative of the gamma function in the complex plane. The *Bloch* correction vanishes at large velocities and behaves like

$\ln(1.1229\upsilon/Z_p\upsilon_0)$, with υ_0 being the Bohr velocity [Sig 04] while the *Mott* correction is the dominating correction increasing with projectile velocity.
So than the stopping of relativistic heavy ions can be rewritten in the simple form

$$-\frac{dE}{dx} = C \cdot (L_{Bethe} + \Delta L_{LS} - \frac{\delta}{2}). \tag{2.17}$$

The Barkas effect [Bar 69] is also has to be considered and it is the difference in stopping power between a particle and its antiparticle. This correction is often called as Z^3 - correction to the Bethe formula and calculated by different authors [Jac 72] [Lin 76].
When the velocity of the projectile becomes sufficiently small one has to consider the motion of the target electron during the collision, so call *Shell* correction. The effect becomes important when $\upsilon_p < Z_t^{2/3}\upsilon_0$. *Shell* correction in the Bethe and Bohr model have been derived by Walske [Wal 52] [Wal 56] and Sigmund [Sig 00], respectively.
Below $\beta \simeq 0.01$, however, a successful explanation of energy loss is given by the theory of Lindhard and Scharf [Lin 61].
The overview of the calculated stopping power with different corrections to the eq. 2.14 is given in [Sch 94] [Kuz 07]. The stopping power described above with all corresponding corrections can be calculated using computer code *ATIMA* [ATI].

2.3.2 Angular Scattering

Angular scattering affects stopping measurements in two ways:

- if the particles in the beam will be deflected away from the detecting system this may lead to distortion of the measured energy loss;
- if the traveled path length and penetration depth through the layer are different it will influence the range of the ions.

The probability of angular deflection into a solid angle $d^2\phi = 2\pi sin\phi d\phi$ if the path length l is small so that $dP \ll 1$ is given by [Sig 04]

$$dP = nlK(\phi)d^2\phi, \tag{2.18}$$

where $K(\phi)$ is the differential scattering cross section and ϕ the deflection angle in the laboratory frame of reference.
Multiple angular deflections become more important with increasing dP. Then the distribution in total angle θ is described by a distribution $F(\theta, l)d^2\theta$ which is similar to the single-scattering profile at large angles but close to gaussian-like shape around $\theta = 0$ [Sig 04].

2.3.3 Charge - Exchange Reaction

Besides the ionization of the target electrons projectile ionization also can occur during the interaction of charge particles with matter. Projectile ionization is a form of charge exchange between few-electrons of the projectile and neutral target atoms. The two most important processes are radiative electron capture (REC) and non-radiative electron capture (NRC) [Sch 98]. REC dominates at high-energy collisions of high Z_p - projectiles with low Z_t - targets and the electron capture is followed by a photon emission. A loosely bound electron may be considered as approximately free in a high-energy collision. An electron initially moving with certain velocity is captured into a bound state of the projectile with the simultaneous emission of a photon. Calculation of REC cross sections into the projectile K-shell is given in [Sto 30] and approximately equal to $\sigma_{REC} \approx Z_t$.
With increasing the nuclear charge of the target materials the importance of the non-radiative capture increases. In the NRC process the electron is transferred radiation less from a bound state of the target atom to a bound state of the projectile in a three body collisions. To match energy and momentum conservation this process thus needs a third particle involved, so the momentum difference is carried away by the target nucleus. The cross sections for NRC are calculated in [Eic 95] and the scaling dependency is giving by $\sigma_{NRC} \sim Z_p^2 Z_t^5 / E_{kin}^5$.
The NRC is dominant in the energy regime up to 90 MeV/u while the REC is a predominate process at the energies more than 100 MeV/u.
There are two computer codes developed which allow one to calculate charge-state distribution over 3 (CHARGE) and 28 (GLOBAL) charge states and mean charge at the equilibrium for relativistic collisions ($E/A \geq 100$ MeV/u) of heavy projectiles $Z_p \geq 30$.
The computer code GLOBAL [Sch 98] was used in this work to calculate the probability for an electron capture by the projectile from the target atom. The calculation shows that the probability to capture an electron from a carbon foil of thickness 10 $\mu g/cm^2$ is about $1.692 \cdot 10^{-6}$. So the probability of the charge exchange is so small and will contribute only after about 1000 turns of ion passage through the foil when the losses due to the ion optics are more essential. Therefore, in further calculations those processes are neglected.

2.4 Simulation of an Ion Motion in the ESR

A detailed understanding of atomic and nuclear interactions of ions penetrating through the matte placed within ion-optical systems is important for planning of many nuclear physics experiments and applications using energetic secondary nuclear beams. Moreover, it is necessary to combine the knowledge of the interaction of swift particles in matter with the transport properties of ion-optical system. For the design studies of the GSI fragment separator FRS [Gei 92] the code *MOCADI* was developed in late 80's [Sch 90]. There are many codes which calculate the transport of ions through ion-optical systems such as COSY [Ber 90], GICO [Wol 90], MIRCO [Fra 83] or Transport [Bro 67]. The Monte Carlo program *MOCADI* was the first code able to trace arbitrary phase-space-density distribution of relativistic heavy ions through ion-optical systems taking into account all particle coordinates and higher order image abberations as well as atomic and nuclear interaction with matter [Iwa 97]. Now *MOCADI* is routinely used for preparation and analysis of experiments with secondary beams: e.g. for rate estimation, for studying beam properties, separation quality, implantation profiles, optimization of the experimental setups and transmission studies [Iwa 97].

As during the penetration of charged particles through the matter different atomic and nuclear processes can take place, therefore it is important to implement into the predicted code those main processes. The particle can change it charge state by capturing or loosing electrons; can capture or loose nucleons in nuclear reactions (fission, fragmentation, electromagnetic dissociation) and as a result of both nuclear and atomic collisions will change its kinetic energy and direction. The nuclear interaction is implemented in *MOCADI* in terms of cross sections [Ber 63] and reaction kinematics [Mor 89]. Atomic interactions are especially important for efficient in-flight separation of energetic fragments using thick degrader placed at dispersive focal plane S2 of FRS. Theoretical descriptions of energy loss, energy loss straggling, charge-state population and multiple angular scattering are implemented into *MOCADI* code.

The code consists of modules which can be arranged in a desired sequence realistically to simulate experimental setup. One can calculate the coordinates of the particles in a complex ion-optical system [Iwa 97]. The electromagnetic fields are imported into *MOCADI* from GICO [Wol 90] and COSY [Ber 90], calculated based on the transfer matrixes, which are applied to any electromagnetic system.

In this work *MOCADI* code is used to simulate the number of detected ions

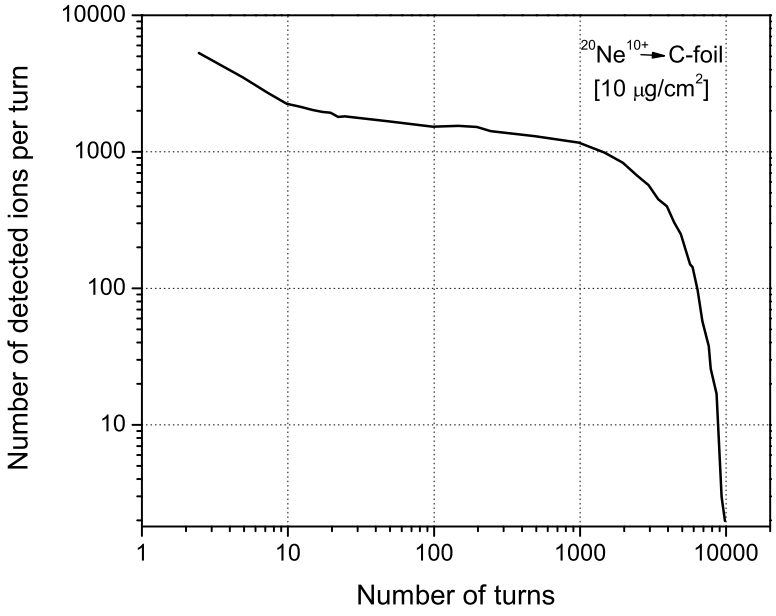

Figure 2.1: Simulated curve of the number of detected $^{20}Ne^{10+}$ ions with E=322.8 MeV/u per turn at the ESR. At each turn the ions pass the carbon foil of thickness 10 $\mu g/cm^2$ in the TOF detector and loss their energy. The strongest decrease of the number of ions is observed already after about 10 turns and it is explained by the larger momentum spread as the momentum acceptance of the ESR of the ions as they are injected from the FRS. Then the curve characterized the number of detected ions per turn is almost constant till about 1000 turns. Due to the energy loss of ions after passage numerous number of turns in the ESR through the carbon foil their trajectories shift and at the end they will be lost by hitting the chamber wall.

by TOF detector per turn in the ESR. The foil aperture in TOF detector placed at the ESR, dipole and quadruples, geometrical boundaries of vacuum chambers are included into the simulations. The size of the beam at the TOF detector position is defined by the foil diameter of 40 mm.
In the simulations about 10000 ions start to circulate at the ring and as in the real experiment at each turn pass the carbon foil in the TOF detector. The carbon foil of thickness 10 $\mu g/cm^2$ is installed in the moment in the TOF detector at the ESR. In the simulations as in real experiment at each turn when the ions pass through the foil they loss energy and after hundreds of turns change their trajectories at the ESR. Therefore, calculation of the energy loss for $^{20}Ne^{10+}$ ions at E=322.8 MeV/u used in the online at ESR (Sec. 4.1) in the carbon foil is implemented into the simulations. The energy loss according to *ATIMA* code [ATI] is ΔE=5 keV. Initial energy

spread of ± 0.2% and emittance of 10 mm mrad of the ion beam was set in the simulations. The simulated curve which explains the dependence of the number of detected ions per turn is shown in Figure 2.1.
After an injection from the FRS into the ESR in about ten turns the ions with a momentum far from the momentum acceptance of the ESR will be lost by hitting the chamber wall. It is clearly seen from Figure 2.1 that the number of ions is drastically decreased during first turns, then the number of ions detected by the TOF detector stays almost constant. After passing through the carbon foil numerous number of turns the ions will loss their energy and also as a consequence of the shift in the trajectories to the left side (negative dispersion) will be lost.

2.5 Time-of-Flight Detector

In Isochronous Mass Spectrometry at the FRS-ESR the masses of the nuclei are directly determined from the revolution frequencies measured by a microchannel plate (MCP) Time-of-Flight detector (Figure 2.2). For the first time this kind of detector was constructed and tested at University of California by D. Bowman and R.H. Heffner [Bow 78]. The details of the detector construction currently used at Giessen University (II Physikalisches Institut) can be found at [Tro 93] [Rad 94] [Wol 97].
In the detector, ions passing a carbon foil release secondary electrons (SE), which are transported to the microchannel plate detectors in forward and backward directions by electric and magnetic fields. The carbon foil is extremely thin [$10\mu g/cm^2$], thus the ions experience only about 5-200 keV energy loss and can longer circulate in the ring without changing crucially the trajectory.
Each branch of the TOF detector consists of equally spaced 12 electrodes which carries a potential supplied by a voltage divider in such way that the linear drop of the potential is obtained. There are two main voltages applied to the voltage divider U^{++} and U^{-}. Those electrode potentials mainly produce a constant electric field in the flight path of the secondary electrons. The other voltages U_{Foil} and U_{MCP} are used to apply potentials to the foil and to the first electrode of the set for the MCP detector. Extra voltage dividers are used to distribute the main voltages U_{MCP} for forward and backward detectors across the electrodes, which supports each MCP plate and provide with a potential difference.
Each MCP detector consists of two microchannel plates, which allows an amplification even of each secondary electrons produced from the foil by a

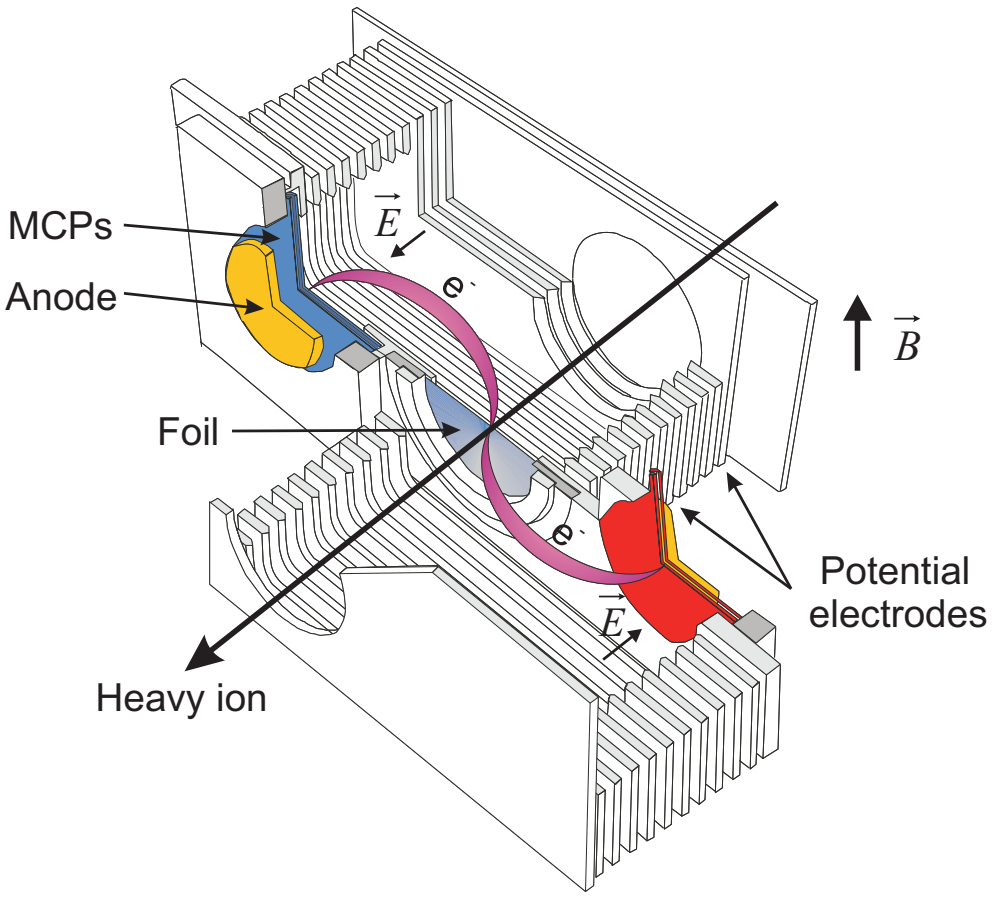

Figure 2.2: Schematic view of the Time-of-Flight detector. Ions passing a carbon foil release secondary electrons, which are transported to the microchannel plate detectors in forward and backward directions by electric and magnetic fields. The number of secondary electrons is multiplied in two-stage MCPs till about 10^6 and detected by the anode to produce measurable signal.

factor of $10^6 - 10^7$ electrons. The foil aperture is 40 mm in diameter as large as the size of the MCP active area. Therefore, the spot size on the foil is the same as potentially used acceptance of the MCP detector. This means that all electrons produced along the foil surface in an ideal case will be detected by the MCP detector. TOF detector is placed in vacuum chamber with operation pressure of about $1 \cdot 10^{-7}$ mbar in offline setup and about $1 \cdot 10^{-11}$ mbar at the ESR.

Under the following subsections the main physical processes occurring in the TOF detector, such as creation of the secondary electrons in the foil by the ions, transport of them in the electromagnetic field to the MCP detectors and detection will be discussed. The working principle of microchannel plates as well as the timing characteristics and rate capability are explained.

2.5.1 Theory of Ion Induced Secondary Electrons

Ions passing through the matter create secondary electrons by inelastic collisions with the electrons of the solid. The main mechanisms caused the secondary electron creation, diffusion of part of the excited electrons towards the surface and penetration into the vacuum as well as a main structures in the electron velocity spectra would be discussed. The "true" electrons are electrons at the energy of 0 - 50 eV [Dre 96] and they are the dominant in the spectrum. Therefore, the electron yield calculations presented below mainly describe the behavior of these electrons.

2.5.1.1 Secondary Electron Creation

Electron emission from the surface can be caused mainly by two different mechanisms: potential and kinetic electron emission [Bru 97]. When a slow (below 1keV/u) positively charged ion interacts with a target material the potential electron emission can take place. The potential energy of the projectile in this case is dissipated through Auger electron capture process and/or by de-excitation [Hag 74] [Agr 73]. Kinetic emission is induced by the direct interaction between the projectile and the atoms of the target. In this kind of process, the Auger effects are less probable.
The mechanism of kinetic electron emission is considered to consist of three steps

- generation of excited electrons in the solid;
- diffusion of part of the excited electrons towards the surface including cascade multiplication;
- penetration of electrons through the surface into the vacuum.

The generation of secondary electrons is described via two main processes happened between the projectile and target, e.g.:

1. direct collision processes between projectile and target atoms and ions:
   - **a)** by excitation of conduction or valence electrons into free states above the Fermi level;
   - **b)** by ionization of inner shells of the target atoms;
   - **c)** by ionization in outer and inner shells of the projectiles;
   - **d)** electron loss of electrons from the projectile;
2. by secondary processes:

a) cascade multiplication of diffusion secondary electrons;

b) excitation of target electrons by energetic recoil atoms (recoil ionization) and by backscattered projectiles;

c) one-electron-decay of volume and surface plasmons generated either by energetic primary ions or by secondary electrons;

d) by protons produced in projectile-target collisions.

Many semi-empirical theories do not separate between different excitation mechanisms and treat the electron generation process in a semi-empirical way [Has 98]. These theories based on the observation that an electron yield and electronic stopping power of the projectile follow the same dependence on the impact energy and ion range is large compared to the mean escape depth of secondary electrons.
The secondary electrons are created along the path of the projectile. On their way towards the surface excited electrons experience collisions with other electrons of the target and the energy, which electron got in primary event will be shared by a large number of collisions with other electrons. During these inelastic processes the cascade of secondary electrons is developed [Has 98]. In semi-empirical theories the diffusion process is described by mean of free pathes for elastic and inelastic collisions of excited electrons [Sch 80]. The mean free path of diffusing electrons may be used to give an estimate about the escape depth of secondary electrons which are detected in vacuum. Experimental mean free pathes vary from about 5 $\mathring{A}$ to 20 $\mathring{A}$ for electron energies up to a few hundreds of eV for metals and semiconductors and may be considerable larger for insulating materials [Sea 79] [Ohy 04] [Has 98]. In case of insulating materials the mean free path of the electrons is higher because the electrons are excited up to conduction band or in a continuum state and have less other electrons to collide. According to this effect more electrons will not be lost in the collisions and will reach the solid surface.
When the electrons reach the surface they still need to overcome the surface barrier that is characterized by the mean work function $e_0\Phi$ and a barrier height $W = E_F + e_0\Phi$, where Φ is a surface potential and E_F is Fermi energy. In case of semiconductors the work function should be replaced by the electron affinity [Sch 80] [Has 98]. The electrons with energy $E_e \leq W$ cannot overcome the surface barrier. For the electrons with energies $E_e \geq W$ the escape probability is a function of the barrier height W. Typical values of the work function for carbon is $e_0\Phi$=4.5 eV [Dre 96]. For the CsI target the work function value is equal to 0.2 eV [She 02]. So, by the difference between these two materials it is clear that in case of CsI foil higher sec-

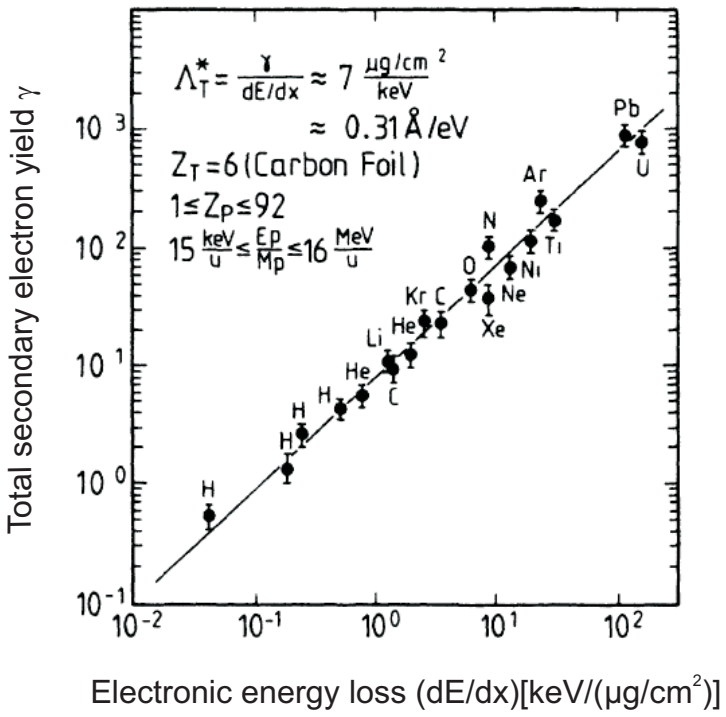

Figure 2.3: The total secondary electron yield from carbon foil as a function of the electronic energy loss dE/dx [Rot 90]. The projectiles the energy losses of which were taken are indicated.

ondary electron yield can be reached. Presently thin carbon foil optimized for the detection efficiency and energy loss is installed in the TOF detector (Sec. 2.5.4.2).

2.5.1.2 Secondary Electron Yield

As it is described above the electron emission is regarded as a three-step process: creation, diffusion, and penetration into the vacuum. By variety of experiments it was shown that the total electron yield n_{se^T} is proportional to the electronic energy loss of the projectile [Dev 91] [Rot 90]

$$n_{\mathrm{se}}^T = \Lambda \cdot \frac{dE}{dx}. \tag{2.19}$$

The constant Λ in eq. 2.19 depends on the target material [Has 98]. As an example the total secondary electron yield in dependence of the electronic energy loss from different projectiles in carbon foil is shown in Figure 2.3. Sternglass [Ste 57] and Koschar *et. al.* [Kos 89] started from this assumption by further considering that the kinetic energy of the projectile may be

lost in two different types of collisions: 1) "soft" collisions with a small energy transfer which leads to the creation of a large number of low-energy secondary electrons; 2) "violent" collisions with a large energy transfer which results in the creation of a small number of energetic δ-electrons. Then the energy loss is described like a sum of losses in both types of collisions [Ste 57]

$$\frac{dE}{dx} = \frac{dE}{dx}|_{\text{soft}} + \frac{dE}{dx}|_{\text{violent}} = \beta_s \frac{dE}{dx} + \beta_\delta \frac{dE}{dx} \tag{2.20}$$

Here, the energy fraction spent in soft collisions is given by $\beta_s = (1 - \beta_\delta)$ [Kos 89]. Sternglass [Ste 57] assumed that $\beta_\delta = \beta_s$=0.5 for fast projectiles of velocities $\upsilon_p > Z_p^{2/3}\upsilon_0$. The number of slow electrons from primary ionization by soft collisions in a layer dx is given as

$$n_s = \frac{1}{E_{\text{se}}} \frac{dE}{dx}(1 - \beta_\delta)dx, \tag{2.21}$$

where E_{se} denotes the mean energy transfer in an ionization event to liberate an electron. The high-energy δ electrons will also produce low-energy electrons due to the secondary ionization processes during their migration through the solid. Only a fraction β_δ of the energy loss is converted into the creation of δ electrons. The total number of δ electrons produced in a layer dx is

$$n_\delta = \frac{1}{E_{\text{se}}} \frac{dE}{dx}\beta_\delta dx. \tag{2.22}$$

The secondary electrons, which are created in the soft collisions along the ion path travel through the solid with inelastic mean free path λ_S. The diffusion length λ_S of low-energy electrons should mainly depend on the target material and not on the projectile atomic number or velocity. The δ electrons produced in the violent collisions have higher kinetic energy and will travel the directions which are pointed forward into the solid [Has 98] while the slow electrons created in the soft collisions in forward and backward directions. The value of λ_δ is found to increase strongly with increasing projectile velocity and can be described by a power law [Jun 96]

$$\lambda_\delta = 390(E_P/M_P)^{1.22}, \tag{2.23}$$

with E_P/M_P is the ratio between a projectile energy and mass in units of MeV/u and λ_δ in units of $\mathring{A}$. The λ_δ of δ electrons will be larger than those of slow electrons and thus these electrons travel further away from their point of origin compared to the slow electrons.

As shown by Sternglass [Ste 57] the function $f(x, \lambda_\delta)$ can be used to describe the transport of high-energy δ electrons

$$f(x, \lambda_\delta) = 1 - e^{-\frac{x}{\lambda_\delta}}. \tag{2.24}$$

Additionally to the eq. 2.24 one has to consider also the transport of slow electrons from their point of production to the surface. This can be done by introducing diffusion function [Rot 95]

$$P_B(x) = Pe^{-\frac{x}{d\lambda_s}} \tag{2.25}$$

$$P_F(x) = Pe^{-\frac{(x-d)}{\lambda_s}}, \tag{2.26}$$

where P denotes the surface transmission probability of electrons leaving the solid surface in forward and backward directions. It depends on the energy and angles of the electrons approaching the surface and the height of the surface barrier. If these two processes are independent from each other one can write the total electron yield n_{se}^T as

$$n_{\mathrm{se}}^T = \int (n_S + n_\delta) P_{B,F} dx. \tag{2.27}$$

It is important to note that the number of highly-energy electrons is not included in the yield calculation directly, but only indirectly by producing low-energy secondary electrons [Rot 95]. By integrating the eq. 2.27 over dx from 0 up to the target thickness d and assuming that $\lambda_\delta \gg \lambda_s$ and dE/dx is a constant for all thicknesses d the expressions for electron yields in forward and backward directions can be written as

$$n_{se}^F = \Lambda \cdot (\frac{dE}{dx})[1 - \beta_\delta e^{-x/\lambda_\delta \rho} - (1 - \beta_\delta) e^{-x/\lambda_s \rho}] \tag{2.28}$$

$$n_{se}^B = \Lambda \cdot (\frac{dE}{dx})(1 - \beta_\delta)[1 - e^{-x/\lambda_s \rho}], \tag{2.29}$$

with $\Lambda = \frac{P\lambda_{se}}{E_{se}}$ given in $[\frac{\mu g/cm^2}{keV}]$. β_δ is about 0.2 for protons and Helium [Has 98] and for heavier ions β_δ increases up to 0.7 [Jun 96], ρ is a density and for carbon is 1.65 $\mu g/cm^2$. The total electron yield of the slow secondary electrons per ion is given by the sum of the yields in forward and backward directions.

With heavy ions, strong deviations from the simple scaling with dE/dx at high energies as 5-6 MeV/u have been observed [Bor 91]. As a result the electron yield will be reduced [Rot 95]. The reduction yield effect is stronger for backward than for forward emission. It was discussed in [Sch 93] that with increasing projectile velocity and charge, the reduction effect disappears in forward direction. This is probably due to the increasing contribution of δ electrons induced secondary cascade multiplication. Therefore, higher electron yield in forward direction is expected than in backward direction at high energies.

For example, in case of $^{238}U^{92+}$ (381.913 MeV/u) ion passing through the carbon foil $[10\mu g/cm^2]$ 48 secondary electrons will be emitted in forward direction and 3 electrons in case of α-particle (1.145 MeV/u).

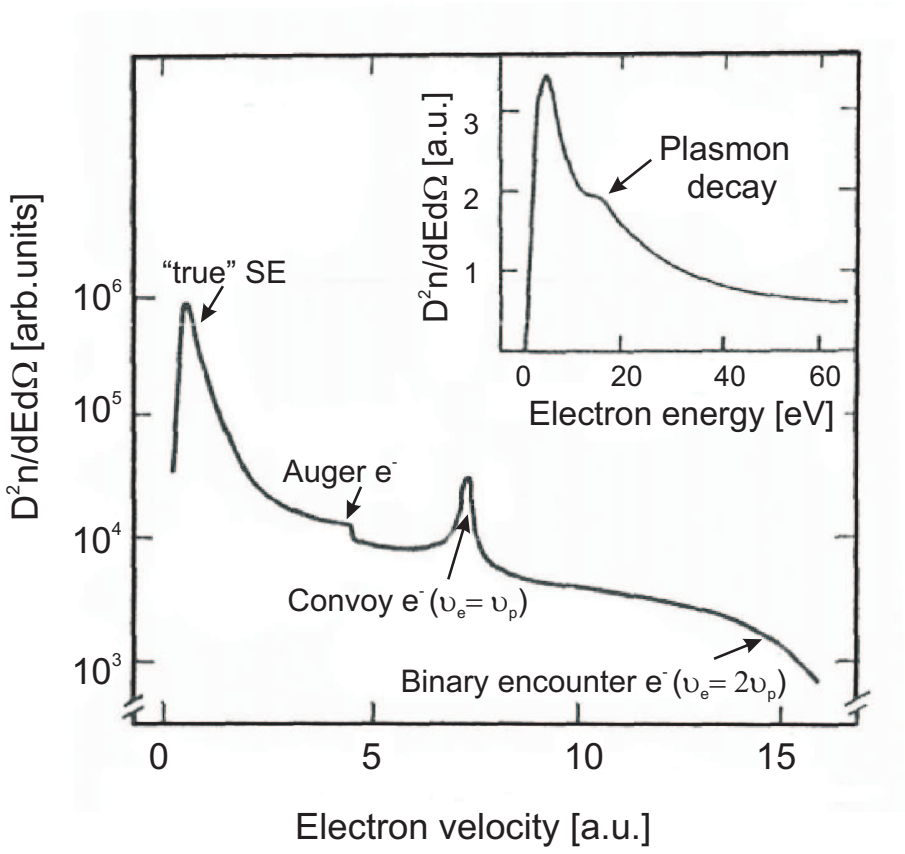

Figure 2.4: Typical secondary electron spectra from carbon foil of thickness 1500 $\mathring{A}$ induced by 1.2 MeV protons according to [Rot 90]. The spectra has been recorded at observation angle $\Theta = 0°$. The structures indicated in the figure as "true" SE, Auger electrons, convoy electrons, binary encounter electrons and electrons from plasmon decay (shown in the inset) are discussed in the text.

2.5.1.3 Secondary Electron Spectra

A typical velocity spectrum of secondary electrons (observation angle θ=0°) from carbon foil induced by 1.2 MeV protons is shown in Figure 2.4. The following structure can be identified [Rot 90] [Has 98]:

1. The maximum of energy spectrum is located at 2.1±0.3 eV and belongs to the low energy "true" secondary electrons. This peak is the dominant in the whole electron energy spectrum and contains about 85% of all secondary electrons. The creation of "true" SE is already explained in Sec. 2.5.1.1 and Sec. 2.5.1.2 by a 3 step model.

2. The second intense peak - convoy electron peak appears at an electron velocity equal to the projectile velocity, $v_e \approx v_p$ [Det 74]. When the ion penetrates through the solid a charge exchange and excitation processes form an atomic charge cloud around the projectile. Some of

these electrons are not lost into completely free states and not captured into bound states but are transferred into a projectile continuum state where they accompany the projectile with the same speed and direction [Has 98].

3. At $E_e \approx 270$ eV, the carbon KLL Auger electron distribution can be observed. When an electron from inner shell is removed on its place the vacancy is created. An electron from higher level can deexcite and occupy this lower vacancy resulting in energy release. The energy can be transferred to another electron, which will be emitted from the atom. This emitted electron is called Auger electron.

4. At twice the projectile velocity, $v_e \approx 2v_p$, the high-energy binary encounter electron distribution is a result from close collisions between the projectile and a target electron. In such collisions the target electron gets the maximum of momentum transfer from the projectile and thus it is the cutoff of the spectrum.

5. At the upper part of the Figure the low energy part of the electron energy spectrum is indicated. This small peak at energy of $E_e \leq$20 eV corresponds to the decay of the collective excitation of the electron solid plasma, plasmon. The energy of a plasmon ($\hbar\omega_p \approx$25 eV for carbon) is transferred to a single electron. When this electron escapes from the surface, its energy reduced by the surface barrier potential given by the work-function Φ. In the end, these electrons are observed in the spectrum at energy $E_e < \hbar\omega_p - \Phi$ [Has 98].

The shape of "true" secondary electron spectra does not depends on the projectile energy, mass or charge. But it depends on the type of the target material [Has 98].
For the simulations (Sec. 2.5.3) Maxwellian distribution with a maximum at 2.1 eV is taken as initial velocity distribution of "true" SE as they are emitted from the carbon foil. This distribution is taken as a similar shape to the dominant peak of SE spectrum explained above (Figure 2.4). Further experimental results on the yields of SE emitted from the thin carbon foil can be found in [Dre 96] [Lou 74] [Agr 70].

2.5.2 Electron Transport in the TOF Detector

An isochronous motion of SE in the time-of-flight detector is achieved by homogenous electric field $\vec{E}$ crossed with a magnetic field $\vec{B}$. Two forces

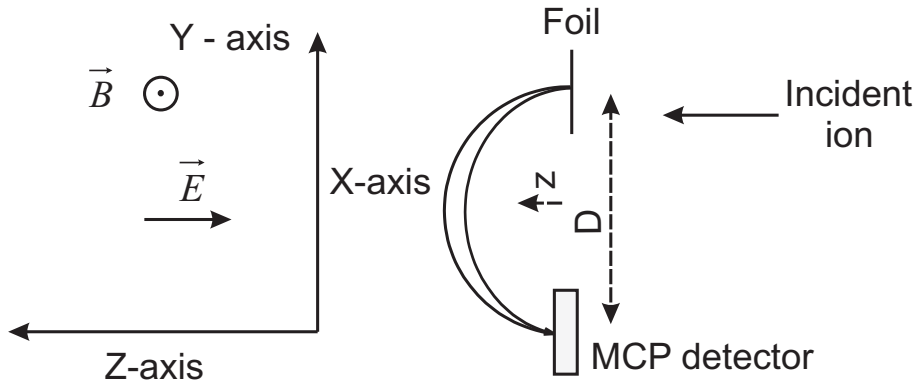

Figure 2.5: Schematic picture showing chosen coordinate system for trajectory calculation of the electrons from the foil to the MCP detector. The heavy ions are incident along the positive z-axis. The direction of an electric field is in minus z-axis and magnetic field is in the positive y-axis.

act on the charged particle moving in the electromagnetic field

$$F = m\ddot{\vec{r}} = q\vec{E} + q[\vec{v} \times \vec{B}] \tag{2.30}$$

By calculating the determinant of matrix according to the (x; y; z;) coordinate system, we will get

$$F = q \cdot [\begin{pmatrix} E_x \\ E_y \\ E_z \end{pmatrix} + \begin{pmatrix} \upsilon_y B_z - \upsilon_z B_y \\ \upsilon_z B_x - \upsilon_x B_z \\ \upsilon_x B_y - \upsilon_y B_x \end{pmatrix}] \tag{2.31}$$

Our chosen coordinate system is illustrated in Figure 2.5 where z axis is taken to be perpendicular to the plane of the carbon foil and the crossed electric $\vec{E}$ and magnetic $\vec{B}$ fields are taken to be in minus -z and plus y directions, respectively. Then taking into account negative z - direction of $\vec{E} = (0, 0, -E_z)$ and positive y - direction of $\vec{B} = (0, B_y, o)$, the eq. 2.31 can be written as

$$F_x = qE_x - \upsilon_z B_y \tag{2.32}$$
$$F_y = qE_y \tag{2.33}$$
$$F_z = q(-E_z + \upsilon_x B_y) \tag{2.34}$$

The system of differential equations with local vector $\vec{r} = (x, y, z)$ for the motion of charged particles is

$$m \cdot \frac{d^2x}{dt^2} = -q \cdot \frac{dz}{dt} \cdot B \tag{2.35}$$
$$m \cdot \frac{d^2y}{dt^2} = 0 \tag{2.36}$$
$$m \cdot \frac{d^2z}{dt^2} = q \cdot \frac{dy}{dt} - q \cdot E \tag{2.37}$$

After solving this equation system 2.35, 2.36 and 2.37 for an electron with mass m and charge q with initial coordinates (x(0),y(0),z(0)) and initial velocity $(\upsilon_x(0), \upsilon_y(0), \upsilon_y(0))$, we will get the components of the position vector of an electron

$$\begin{aligned} x(t) &= x(0) - \frac{\upsilon_z(0)}{\omega}(1-\cos(\omega t)) + \frac{\upsilon_y + E/B}{\omega} \cdot \sin(\omega t) - \frac{E}{B}t & (2.38)\\ y(t) &= y(0) + \upsilon_x(0)t & (2.39)\\ z(t) &= z(0) + \frac{\upsilon_y(0) + E/B}{\omega} \cdot (1-\cos(\omega t)) + \frac{\upsilon_z(0)}{\omega} \cdot \sin(\omega t), & (2.40) \end{aligned}$$

with cyclotron frequency $\omega = qB/m$. The equations of motion 2.35, 2.36, 2.37 describe a cycloidal trajectory and the time required for one cycle is given by

$$T = \frac{2\pi}{\omega} \tag{2.41}$$

The lateral displacement D of the electron in x direction is calculated by neglecting velocity component in z direction

$$D = x(T) - x(0) = \frac{2\pi m}{q}\frac{E}{B^2}. \tag{2.42}$$

The maximum deflection of the electrons in z direction is

$$\begin{aligned} z(T/2) &= z(0) + \frac{E}{B\omega}[1 - cos(\frac{\pi}{\omega}\omega)] = z(0) + \frac{2E}{B\omega} & (2.43)\\ z_{max} &= z(T/2) - z(0) = \frac{2E}{B\omega}. \end{aligned}$$

The travel time of the secondary electrons is dominated by the ratio E/B. For our design quantities this ration is qual to $2.08{\cdot}10^9$ cm/s. The most probable electron knockout energy is a few electron volts corresponding to the velocity $\upsilon(0) \approx 10^8$ cm/s [Bow 78]. Therefore, one expects that the time-of-flight of secondary electrons according to eq. 2.41

$$T = 4.6ns, \tag{2.44}$$

and flight fluctuations will be approximately

$$\frac{1}{\omega}\frac{\upsilon(0)}{(E/B)} \simeq 32ps. \tag{2.45}$$

In order to increase the kinetic energy of secondary electrons when they impinge on the MCP detector to be detected with a good efficiency the position of the MCP detector is shifted by 1 mm relative to the plane of the foil into the direction of the incoming electrons [Tro 93].

2.5.3 ITSIM Simulation of the Electron Transport

An electron transport in the Time-of-Flight detector is simulated with *Ion Trajectory Simulation Program* (*ITSIM*) [Pla 01]. The *ITSIM* simulations are of a great importance to understand and to improve the TOF parameters which influence on the timing characteristic of the detector and therefore on the mass accuracy in the measurements at ESR. The program is suited for a particle trajectory calculation for any analytical or numeric given electric and magnetic fields as well as a gas flow field. The detector geometry for the simulations is drawn in the computer program *COMSOL* [COM] by an implemented *CAD*-Program. For every detector electrode of 3D geometry an electric potential Φ is calculated with *COMSOL* program by solving the Laplace's equation

$$\nabla\Phi = 0. \tag{2.46}$$

Calculated electric field is imported into the *ITSIM* program. The potential linear drop, created by two main voltages U^{++} and U^{-} (Sec. 2.5) as well as two other potentials for the foil aperture U_{Foil} and the potential for the first plate of microchannel plate detector U_{MCP} are implemented into the simulations.

The magnetic induction at a certain applied current to the coils of the magnet is measured with a Hall probe and additionally the homogeneity of the magnetic field is calculated with a finite element method [Fab 08] with *COMSOL* program. The calculations by Fabian [Fab 08] show that the relative field deviations from the middle of the dipole magnet to the outer sides are about 10^{-4}. Taking into account those small deviations it was decided to use in the *ITSIM* a constant ideal magnetic field for the electron transport simulations.

For the *ITSIM* simulations several initial conditions have to be set. The initial kinetic energy distribution of the secondary electrons when they are emitted from the foil surface is chosen as Maxwellian distribution with a maximum at 2.1 eV and standard deviation of 1.8 eV (Sec. 2.5.1.3). In the ESR the TOF detector is installed to be perpendicular to the direction of circulating ions. Therefore most of the ions pass through the foil orthogonally and creation of secondary electrons in the other directions then normal to the foil surface are assumed to decrease with a cosine law [Kos 89] [Tro 93]. Uniform isotropic emission angles of the electrons from the foil in the simulations do not show significant influence on the timing characteristics. An initial spatial distribution of the secondary electrons on the foil area is chosen as homogeneous distribution. In the previous work the Gaussian distribution with a standard deviation of σ=10 mm was used [Fab 08].

Simulations show that the contribution of the Gaussian initial spatial distribution of SE on the foil is σ=18 ps and from homogeneous distribution is 30 ps. In further investigation the homogeneous distribution is used in this work as worst-case scenario. Calculated magnetic field strength of 8.4 mT at which the maximum of transmission efficiency is achieved is not changed with variation of the initial electron spatial distribution.
Typically in the simulations the trajectories for 10000 electrons are calculated.

2.5.4 Microchannel Plates

To detect several secondary electrons produced from the foil and to get a measurable signal, two microchannel plate detectors are used. MCPs are made from a dense stack of about 10^6-10^8 individual parallel micro-channels (Figure 2.6), each of them works like an electron multiplier with a typical gain of about 10^4. While the front and the back surface of the MCP is coated with a metal, the inside of the channels is covered with a semi-conducting layer that tends to emit secondary electrons under the bombardment of primary energetic particles or charged particles as electrons. By biasing

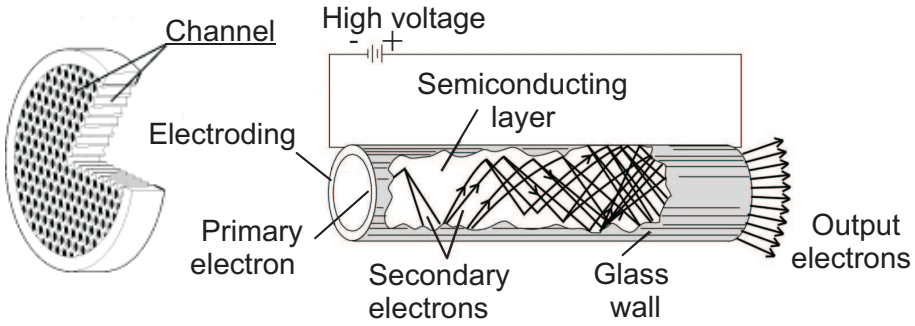

Figure 2.6: Cross sectional view of the microchannel plate [Enc]. Principle of the electronic multiplication.

the MCPs surfaces with a typical voltage of 1000 V, each of the secondary electrons gains enough kinetic energy to liberate more electrons when it hits the wall. An avalanche of the electrons is forming along the channel length and finally exiting the pore. An approximate gain g is dependent on the coating layer of the channels and given by

$$g = \exp(G_0 \alpha). \tag{2.47}$$

Here, $\alpha = \frac{L}{d}$ is the ratio of the channel length (L) to the channel diameter (d) and G_0 is the secondary emission characteristics of the channel wall,

called gain factor. The gain factor is an inherent characteristic of the channel wall material and represented by a function of an electric field intensity inside the channel.
When the even higher gains are required two or three MCPs are used in stacked configurations. The two-stage MCPs offers gain higher than 10^6 and three-stage MCP higher than 10^7. To prevent an effectiveness of incident particles from passing through the channels the MCPs are used in chevron configuration, have a bias angle [Wiz 79]. The bias angle is an angle formed by the channel axis and the axis perpendicular to the plate surface and an optimum value is usually from 5° to 15°.
The detection efficiency of the microchannel plates is different for different particles and their energies. For electrons in the range of 300 V to 1000 V the detection efficiency approximately equal to an Open Area Ratio (OAR) of the microchannel plate. The Open Area Ratio is a ratio of the the open area to the total effective area of the MCP area and is usually at least 60% [Bru 97].
What makes the MCP unique is the localization of the charge cloud into one tiny pore and the presence of a fast number of pores over a large area that operate independently. So, due to the small size of each individual channel the timing of the particle impact can be determined very accurately. In this work MCPs from Photonis Group were used [Phob]

2.5.4.1 Timing Characteristics of MCP

Micro-channel plates are widely used for detection of charged particles in different subjects where the accuracy of picosecond level in timing characteristics is required.
The rise time of the MCP assemblies is very small, usually it is less than 1 ns. The width of the MCP signal is mainly determined by the electrodes, anode construction and limited by temporal characteristics of electronics used to detect an electron avalanche.
The model of Fraser [Fra 88] suggests that the transit time spread through a single MCP with a fixed L/d ratio would vary linearly with a pore diameter. If to compare the signal shapes from the MCP plates with the same active diameter but with different pore sizes one could expect slightly better rise time from the MCPs with smaller channel diameter. Thus, taking the MCPs with smaller channel diameter one shortens the electron transit time and improves the rising slope quality [Ina 06] [Leh 07].
On the other hand according to eq. 2.47 the gain of the MCP is determined by L/d ratio, thus the outer size of the MCP can be reduced while keeping

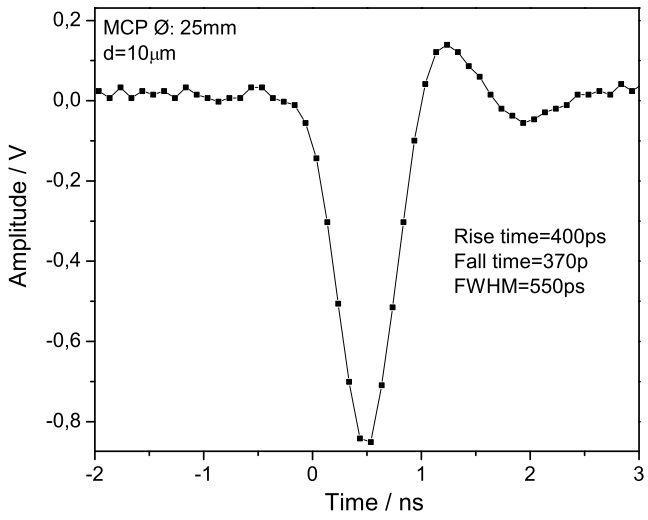

Figure 2.7: Measured signal from the MCP with 25 mm outer diameter, 10 μm channel diameter and length-to-diameter ratio of L/d=40:1. By reducing the outer diameter of the MCP one also can improve the shape of the signal, namely rise/fall time and FWHM.

the gain at a constant value [Ham 06]. Figure 2.7 shows signal of two-stage MCPs with outer diameter of 25 mm and 10 μm channel diameter measured with 1 GHz LeCroy oscilloscope (10 Gs/s). By using MCPs with smaller active diameter in the set with smaller electrodes and anode respectively, one can achieve excellent time response characteristics.
The quality of the MCP signal shape influences on the time accuracy of the detection systems. Thus, a smaller pore size of the MCPs results in a better time accuracy [Leh 07]. Figures 2.7 proves that further reduction of the rise / fall time and FWHM of the MCP signal is possible to achieve. This issue is to be investigated in Sec. 3.1.2 and Sec. 3.1.3.

2.5.4.2 Detection Efficiency of Secondary Electrons

In most experiments on electron emission the electron spectra is measured with silicon detectors [Mon 88]. A model about an approximation of an electron detection yield is described in [Bru 97]. This model assumes that the probability P_n of emitting an average number of electrons $\bar{n}_{se}$ from the surface follows a Poisson law distribution of the type

$$P_n = \frac{\bar{n}_{se}^n}{n!} e^{-\bar{n}_{se}}, \tag{2.48}$$

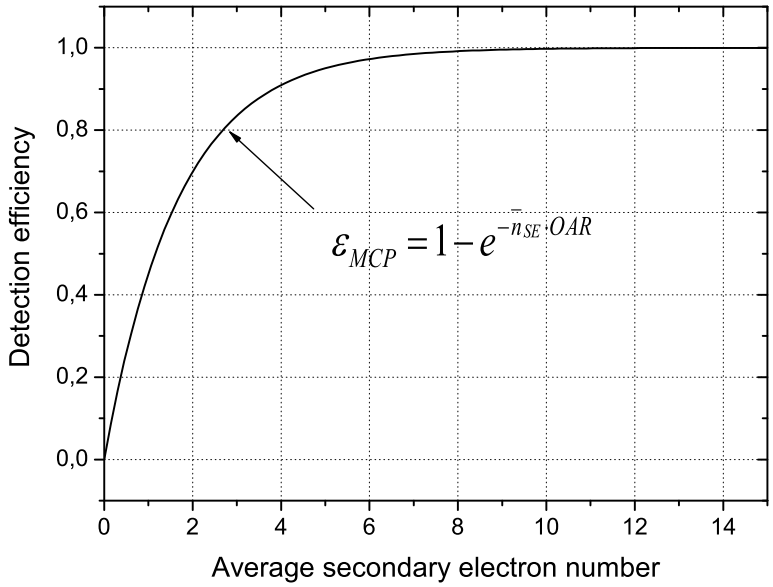

Figure 2.8: Calculated dependence of detection efficiency on the average number of created secondary electrons. According to eq. 2.52 the detection efficiency depends on the number of created SE and open area ratio of the MCP (OAR). At about 6 produced secondary electrons the detection efficiency is optimized till 100%. Further increase of the number of secondary electrons does not lead to the higher detection efficiency.

where n_{se} is the number of emitting electrons from the surface.
The probability of not emitting any electrons is given by

$$P_0 = e^{-\bar{n}_{se}}. \tag{2.49}$$

If the detection efficiency on the MCP surface is ε_{MCP} then the probability of detecting n electrons becomes

$$P_n = \frac{(\bar{n}_{se}\varepsilon_{MCP})^n}{n!} e^{-\bar{n}_{se}\varepsilon_{MCP}}. \tag{2.50}$$

The probability of detecting at least one electron is equal to

$$P_e = (1 - P_0) = 1 - e^{-\bar{n}_{se}\varepsilon_{MCP}}. \tag{2.51}$$

The detection efficiency of the MCP in eq. 2.51 is given by the whole open area ratio of the microchannel plate. The electrons will be detected by the MCP only in that case if at least one electron was produced from the solid surface and hits within the open area of the MCP. In this case the detection efficiency can be written as

$$\varepsilon_{MCP} = 1 - e^{-\bar{n}_{se}OAR}. \tag{2.52}$$

OAR of the MCP corresponds to about 60% [Bru 97].
Figure 2.8 illustrates the dependence of the detection efficiency on the produced electron number. According to the calculations from eq. 2.52 the detection efficiency reaches 100% at 6 produced electrons.

2.5.4.3 Rate Capability of MCP

The range of application of microchannel plates operation is often cased by the limitation of the channel plates themselves. Due to the dead time of MCPs there are two effects contributing to the limit of the rate acceptance, which have to be considered.
On one hand, when a large output current is drawn from the MCP, the channel walls near the exit end are charged due to a large amount of secondary electron emission. The strip current flowing through the channel walls neutralizes this charging effect. The strip current of the MCP is the current flowing through the MCP supplied by the power supply. However, this neutralization takes time because the strip current is small due to the high resistance of the channel walls. The time required for this neutralization is termed dead time. The gain decrease is called saturation effect, and begins when the output current reaches 5% to 6% of the strip current.
On the other hand a geometrical effect caused by the finite number of channels in the microchannel plate limits the rate acceptance. When a second electron enters the channel within the time needed to recharge the channel walls, exited channels are not able to recharge sufficiently. Therefore the channels do not respond to the new incoming particle. Both effects lead to the same result: the measured count rate of the detector is different from the real rates of electrons or ions and the gain drops.
The electron cloud emerging from a single MCP consists of a collection of electrons whose average number is equal to the average gain of the MCP at the operating voltage. In case of using MCP in Chevron configuration one has to take into account the size of the electron cloud when it hits the second MCP. As one channel in the first MCP excites 10-100 channels in the second MCP so the effective rate the MCP could take is less than the number of channels in the first MCP. The approximate width D of an electron cloud when it hits the second MCP can be calculated according to the theoretical model [Rog 82].

$$D = d + 4[\sqrt{E_N + U_G} - \sqrt{U_N}]\frac{L}{U_G}\sqrt{E_T}. \tag{2.53}$$

The electrons emerge from a single MCP channel with average transverse emission energy E_T of about 0.2 eV and normal component E_N of about 50

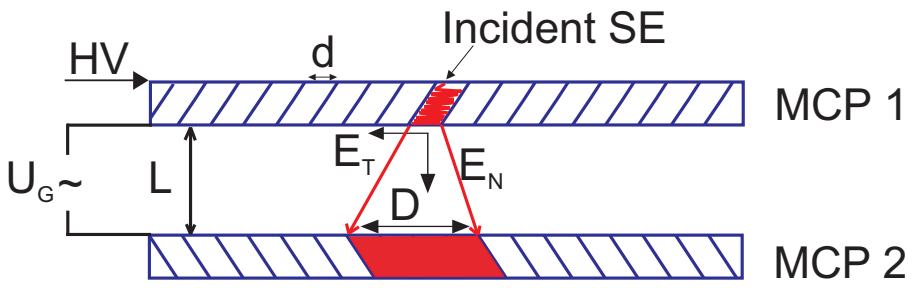

Figure 2.9: Schematic view of the spread of the electron cloud emerging from the first MCP and being detected by the second one. The transverse energy causes the cloud to spread out as it travels between the MCPs. The approximate width of the electron cloud can be calculated in terms of the gap size (L), voltage across the gap (U_G), and the transverse energy of the electrons(E_T). Model described by [Rog 82].

eV (measured by [Ebe 80]). Where d is the channel diameter of the MCP, U_G and L are the applied voltage and distance between two microchannel plates respectively. Schematic view of the spread of the electron cloud with described parameters is shown in Figure 2.9. The number of excited channels in the second MCP will be

$$N_{Exc} = \frac{(d + 4[\sqrt{E_N + U_G} - \sqrt{U_N}]\frac{L}{U_G}\sqrt{E_T})^2}{d^2}. \tag{2.54}$$

Assuming that every single channel behave like an ideal capacitor with typical dead time τ_{channel}, so depending only on its resistance and the capacity [Sha 89], one can describe the gain, count rate and the MCP current. The total dead time of the microchannel plate is given as

$$\tau_{MCP} = \frac{\tau_{channel}}{N_{effective}} = \frac{\tau_{channel} N_{exc}}{N_{total}}, \tag{2.55}$$

where $N_{\text{effective}} = N_{\text{total}}/N_{\text{exc}}$ is the ratio between the total number N_{total} of available channels in the MCP and the number of excited channels N_{exc}. The approximate gain q of an MCP is given by eq. 2.47. Depending on the particle count rate the incoming current is given by

$$I_{in} = qf, \tag{2.56}$$

where q and f is the the charge and the count rate of the incoming particles. In case of electrons $q = e$. The gain is the ratio of the MCP outgoing I_{out} and incoming I_{in} current

$$g = \frac{I_{out}}{I_{in}}. \tag{2.57}$$

The average gain, which may be identified from an experiment as the maximum amplitude of symmetric pulse-hight distribution (PHD) can be written as

$$g = \frac{g_0}{1 + f\tau_{MCP}}. \tag{2.58}$$

From the equation one can see that for lower count rate and $\tau_{MCP} \approx 10^{-7}s$ the dominator can be neglected, then $g = g_0$. But for higher rate the gain decreases because of the finite recharge time. If to solve equation (2.5) for the output current then

$$I_{out} = \frac{fgg_0}{1 + f\tau_{MCP}}. \tag{2.59}$$

Under the simplified assumption that should show the experimental count rate in dependency on the actual count rate, formula for the experimental count rate can be written analogous to the MCP current as

$$f_{exp} = \frac{f}{1 + f\tau_{MCP}}. \tag{2.60}$$

However it should be mentioned that this is an assumption which may differ from actual experiments. The real count rate measurement process is a difference between the current measurement and the determination of the count rate.

One of the important parameter to observe influence of the high rate on the MCP is the change of the pulse-height distribution. The pulse-height distribution is an abundance histogram of the measured signal amplitudes. If all the participating channels of the MCP are unsaturated, as is the case if only a small number of electrons enter each channel, the resulting PHD is exponential. But, as more and more participating channels saturate, the PHD changes from from a negative exponential to a quasi-Gaussian and the modal gain of the output pulses increases.

Examination of the pulse-hight distribution of output signals from the MCP detector presents an important information about the relative detection efficiency of ions. At higher rates while decreasing the gain the mean of the PHD also shifts to smaller amplitude values and changes its shape [Giu 94], [Fra 91], [Fra 92]. It leads to more amplitudes to drop under the threshold and the area under the pulse-hight distribution decreases and so does the detection efficiency.

Investigation of the behavior of the PHD at different electron rates will be discussed in Sec. 3.3.2.

Chapter 3

Offline Experiments

For better performance of the time-of-flight detector, the performance characteristics of a duplicate of the detector at Gießen University (Figure 3.1) have been investigated and improved in offline experiments. Particular in this work the timing performance and the rate capability have been measured and enhanced. The detection efficiency improvements developed in previous work [Fab 08] have been varified.
To substitute the ions circulating in the ESR and passing through the foil in the laboratory conditions the alpha emitter source ^{241}Am was used. A kinetic energy of the alpha particles is 5.486 MeV. The energy spectrum from ^{241}Am also contains less intense lines as 5.443 MeV (abundance of 12.8%) and others with an abundance less than 2% each. As this alpha source is covered with about 2 μm thick noble metal, the kinetic energy of the alpha particles when they hit the carbon foil is 4.58 MeV [Tro 93].

3.1 Timing Performance of the TOF Detector

The timing performance of the time-of-flight detector is a critical parameter as it influences on the mass measurement accuracy. The intrinsic time accuracy of the TOF detector was investigated in the coincidence time-of-flight measurements between forward and backward MCP detectors. It amounts to about σ_{coin}=67 ps for the standard settings. One revolution in the ESR has a duration of about 500 ns. Due to the many revolutions in the ring the uncertainty of the mean revolution time can be reduced to less than a picosecond. Note that this uncertainty is required for the mass of 100 GeV to achieve a mass accuracy of a 100 keV (eq. 2.10).
By ITSIM (Sec. 2.5.3) simulations and experimental measurements for dif-

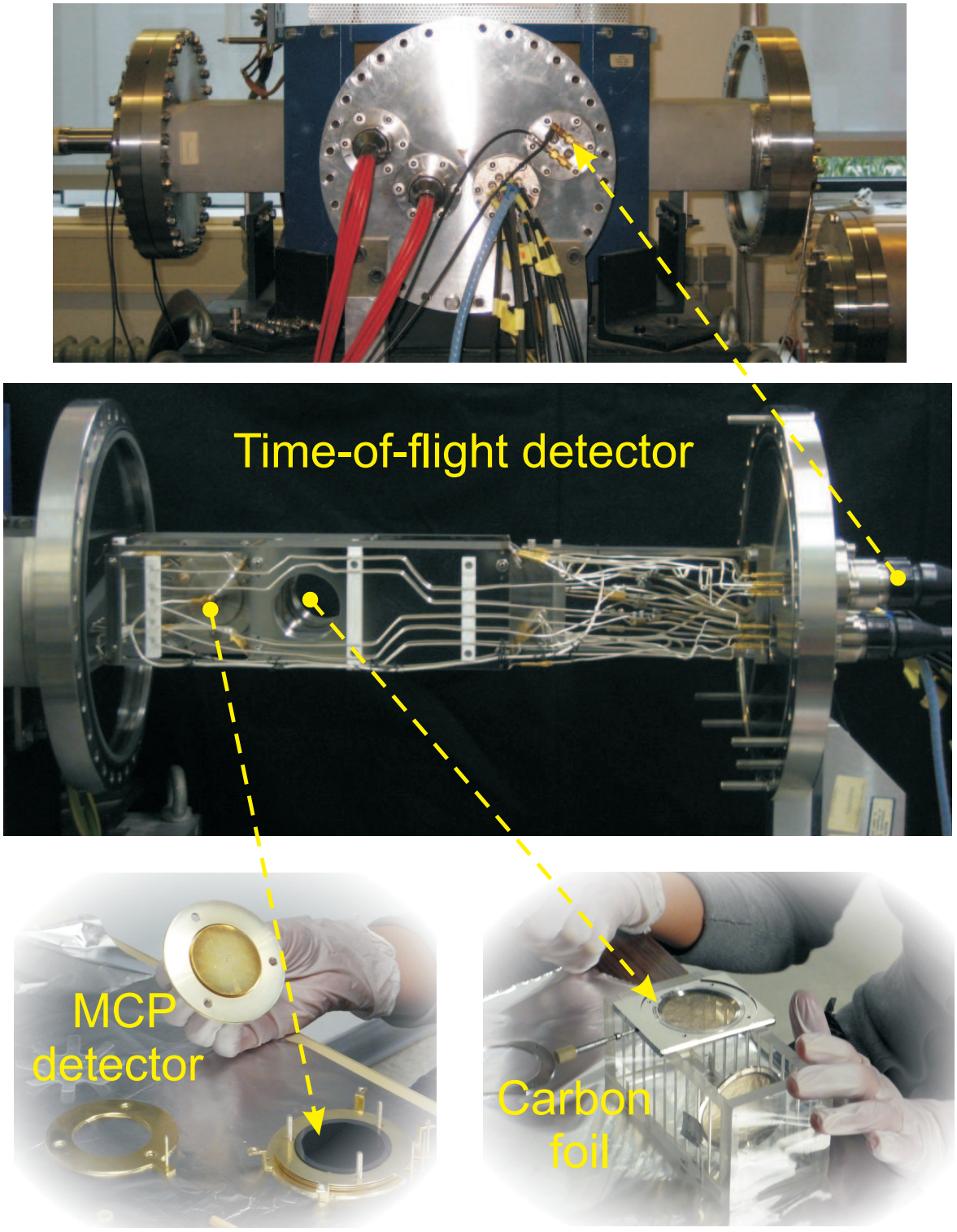

Figure 3.1: Front view of the Time-of-Flight detector in IONAS group at Gießen University. The main components as the carbon foil, MCP detector, dipole magnet and cables for the voltages are indicated with callouts.

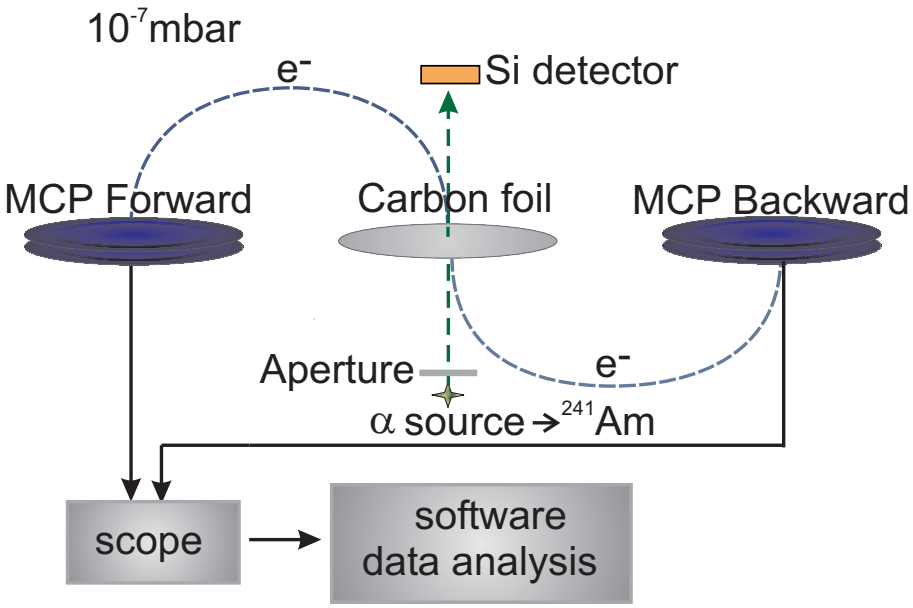

Figure 3.2: Setup used for the offline measurements of coincidence time-of-flight between forward and backward detectors. ^{241}Am source emits alpha particles, which hit a thin carbon foil. The secondary electrons produced in forward and backward directions in sense of the α particles direction are guided to the MCP detectors by electric and magnetic fields. The detector is placed in vacuum. The operation pressure is about $1{\cdot}10^{-7}$ mbar.

ferent contributions that influence on the TOF detector timing precision were investigated and can be written as a quadratic sum of the following contributions:

- Transport of the SE from the foil to the MCP detector: σ(Transport)
- Transit time of SE through the MCP channels: σ(MCP)
- Event time determination (determination of the time of the event from the MCP signal, ETD): σ(ETD)

$$\sigma = \sqrt{\sigma^2(Transport) + \sigma^2(MCP) + \sigma^2(ETD)}. \tag{3.1}$$

Timing characteristics were tested by measuring the coincidence between the time-of-flight of the secondary electrons to the backward and forward MCP detectors with a setup shown in Figure 3.2. So the alpha particles passing a thin carbon foil [10 $\mu g/cm^2$] release secondary electrons (Sec. 2.5.1.1), which are transported in forward and backward directions by electric and magnetic fields.
The time definition for the timing measurements is explained in Figure 3.3. Ideally it is interesting to know the time when an ion exactly passes through

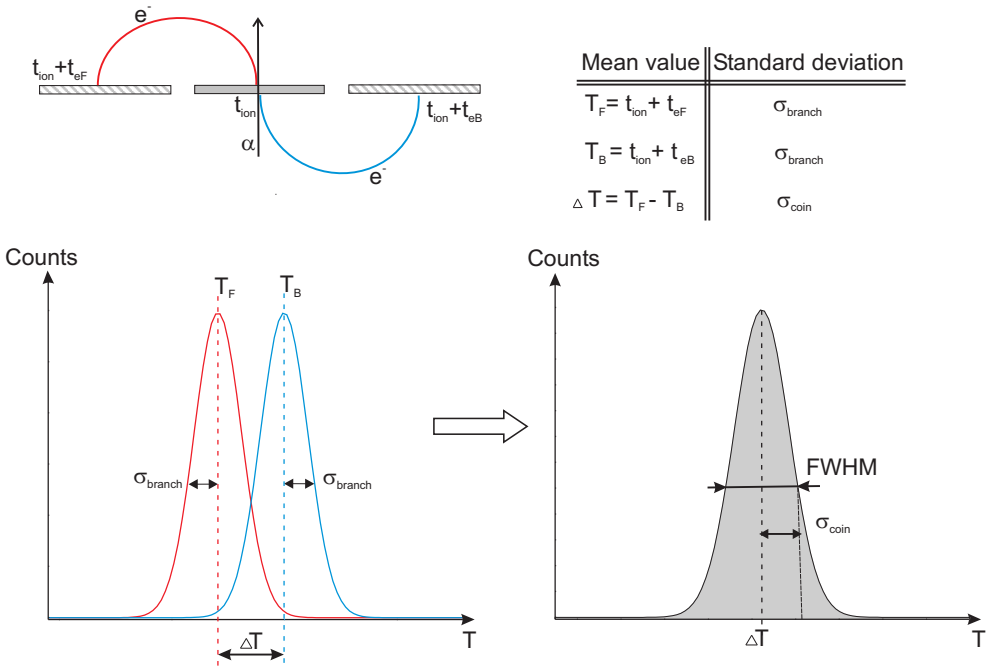

Figure 3.3: Schematic explanation of the time definition in the experimental measurements of the time-of-flight distribution. In the measurements the time when the SE are detected by forward $T_F = t_{\text{ion}}+t_{\text{eF}}$ and backward $T_B = t_{\text{ion}} + t_{\text{eB}}$ MCPs is determined. Then every corresponding time event from both detectors are subtracted from each other and the result is plotted in a histogram. The resulting distribution with mean value ΔT is a coincidence time-of-flight distribution with standard deviation σ_{coin}. The σ_{coin} defines the time spread between two detectors and determines the timing precision of the TOF detector.

the foil t_{ion} and the secondary electrons are created. In our coincidence time-of-flight measurements the time difference ΔT between the time, when the electrons are detected by forward T_F and backward T_B MCP detectors, was measured. The distribution of ΔT is then the coincidence time-of-flight distribution, from which the Full-Width-at-Half-Maximum (FWHM) or the standard deviation σ_{coin} is determined. Later to characterize the timing performances of the TOF detector, the standard deviation of the coincidence time-of-flight distribution σ_{coin} will be used. This standard deviation defines the time spread between forward and backward MCP detectors.
In an ideal case the detector is isochronous and the secondary electrons produced in the foil should be transported to both MCP detectors simultaneously. Since these two transport times T_F and T_B are independent events, it is reasonable to assume that

$$\begin{aligned} \sigma_F^2 + \sigma_B^2 &= \sigma_{coin}^2 \Longrightarrow \sigma_{coin}^2 := 2\sigma_{branch}^2 \\ \sigma_{coin} &= \sqrt{2}\sigma_{branch}. \end{aligned} \tag{3.2}$$

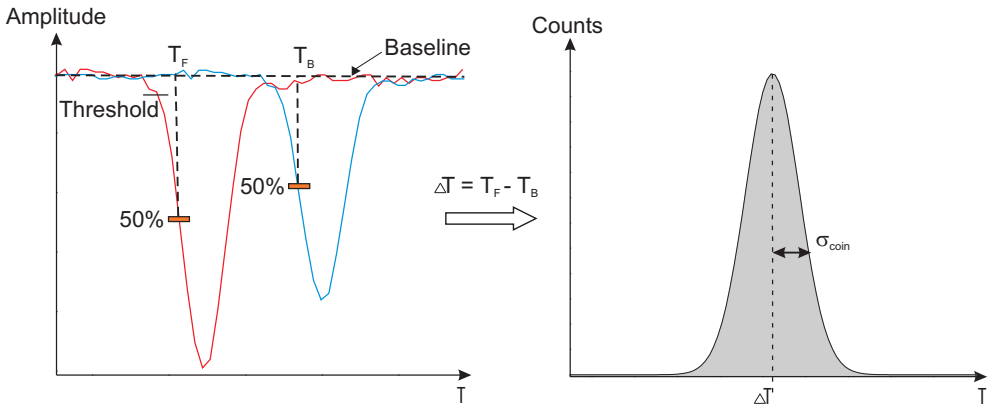

Figure 3.4: Principle of the time-of-flight determination with *Ddelay* math function on the digital oscilloscope. The function first determines 50% of the amplitude from the MCP forward and MCP backward detector signals. Then the corresponding time level T(at 50%) is calculated. Two timing events are subtracted from each other and the difference ΔT is plotted in a histogram. The resulting distribution is fitted with a Gaussian function and the standard deviation σ_{coin} is determined.

The corresponding standard deviation for a single detector branch (forward or backward) will be denoted as σ_{branch}. This assumption (eq. 3.2) is confirmed by simulations [Diw 11] and shows, that σ_{branch} can be calculated from the measurements of the coincidence time-of-flight.

One of the methods to estimate the time spread between two MCP detectors is to measure the time difference with *Ddelay* math function on the digital oscilloscope (LeCroy Waverunner 6100A). The principle of this method is shown in Figure 3.4. This function first determines 50% amplitude fraction from the threshold level for forward and backward signals. Then the exact time corresponding to those amplitude levels is determined and subtracted from each other. According to our time definition in this method the difference ΔT between T_F(at 50%) and T_B(at 50%) is measured. Base line determination, time interval as well as the time interval accuracy for this method is explained in the Appendix. About 1000 measurements of ΔT is plotted in a histogram and the distribution is fitted with a Gaussian function. The standard deviation σ_{coin} is calculated from the Gaussian fit function.

The second method is to store the signal acquisitions with an oscilloscope and to analyze the data with *Extract_Timestamps* software that was developed at GSI especially for the IMS data analysis [Hau 99] [Sun 08a]. The Constant-Fraction Discriminating method implemented in the software was used in this work to determine the coincidence time-of-flight distribution (Sec. 4.3.1).

3.1.1 Electron Transport Time

Before proceeding to the simulation of electron transport time, which is one of the limiting contribution to the accurate time measurement in the TOF detector, it is necessary to explain the physical origins which cause the time spread:

- Foil and MCP detectors have different applied potentials to provide an acceleration of SE and to detect them with a certain kinetic energy (in standard case 700 eV). Moreover, the detectors are displaced relative to the plane of the foil so that the secondary electrons impinge on the detectors with enough energy to be detected with good efficiency (Sec. 2.5.2).
- Because of not ideally homogeneous electric field, different points of origin of the secondary electrons in the foil cause different transport time of them to the MCP detectors (see Figure 3.6).
- Secondary electrons are emitted from the foil with different initial kinetic energies [Dre 96] (see Figure 3.5).
- Secondary electrons are emitted from the foil with different angles [Dre 96].
- A non-perfect flatness of the foil can cause different horizontal starting position of the secondary electrons and therefore influences the transport time. As the carbon is a conducting material, the surface of the carbon foil influences the electric field. In the simulations an ideally flat foil is assumed and the real foil surface structure is not included.

First two statements can be considered as contributions from spatial distribution of SE as they are emitted from the foil, the next two are belong to the limitations caused by the velocity distribution of secondary electrons. These two contributions will be discussed below.
So, the contribution from the electron transport is mainly described by:

- Spatial distribution of the secondary electrons: σ(spatial)
- Initial velocity spread of the secondary electrons: σ(velocity).

Then the contribution from the electron transport σ(Transport) in eq. 3.1 has two components:

$$\sigma(Transport) \propto \sqrt{\sigma(spatial)^2 + \sigma(velocity)^2}. \tag{3.3}$$

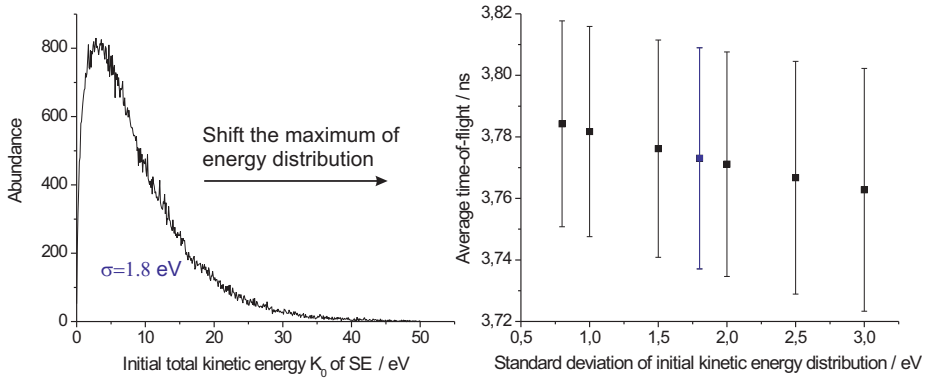

Figure 3.5: a) Initial total kinetic distribution of SE as they are produced from the foil is set as Maxwellian distribution in the Itsim simulations with a standard deviation of 1.8 eV. b) Simulation of an average time-of-flight of SE as a function of standard deviation of the total initial kinetic energy distribution K_0=0-50 eV. By the error bars the standard deviations of the corresponding time-of-flight distributions are given. The acceleration voltage between the foil and MCP detector is set as 700 V.

The dispersion in the time-of-flight of the secondary electrons due to their initial velocity spread and their spatial distribution after emission from the surface of the foil was studied in the simulations. As one of the initial conditions for the simulations the energy spread of the electrons after they are emitted from the foil is chosen as Maxwellian distribution with a standard deviation of 1.8 eV (Sec. 2.5.1.3)(Figure 3.5 a). Figure b) shows the change of an average time-of-flight of SE with the change of standard deviation of the Maxwellian distribution. By varying the σ the mean value K_0 of the total initial kinetic ener-gy is varied. It follows that increase in kinetic energy decrease the average time-of-flight of SE.
In Figure 3.6 the average time-of-flight of SE to the MCP detector is shown according to their point of emission from the X-coordinate of the foil surface along Y=0. The middle of the foil is indicated as 0 mm. One can see that the difference in the average transport time between SE produced in the middle of the foil and at the edges (X=17 mm) is about 65 ps.
Figure 3.7 summaries the result of simulation including initial energy distribution and homogeneous spatial distribution of secondary electrons. The simulation is done for optimized for efficiency potential difference between foil and MCP detector of 700 V. The standard deviation σ_{branch}(Transport) of the time-of-flight distribution caused by the transport of SE from foil to the MCP detectors equals 36 ps. For the present geometry of the TOF detector this contribution is more like a property of the system and can

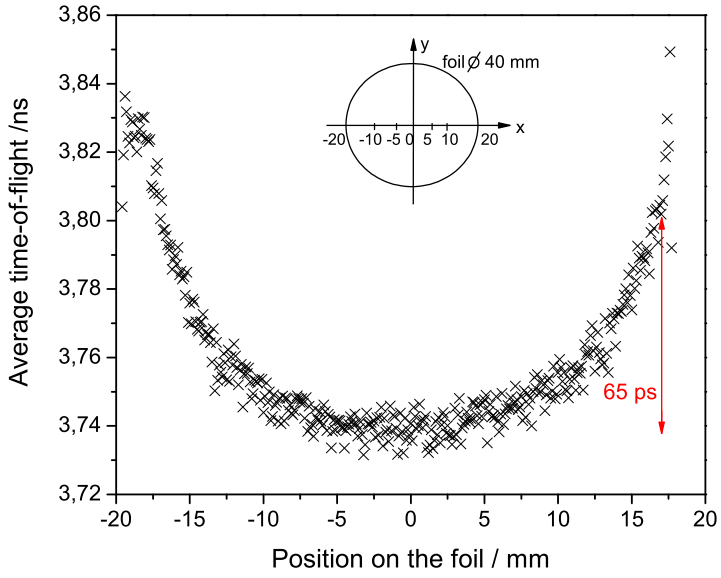

Figure 3.6: Simulated average time-of-flight of SE to the MCP detector as a function of their point of emission from the X-position along Y=0 of the foil surface. The middle of the foil is indicated as 0 mm. The difference in the average transport time between SE produced in the middle of the foil and at X=17 mm is about 65 ps. 17 mm is taken because the SE emitted at this position on the foil surface still can be detected with reasonable efficiency.

not be completely excluded. However, it is possible to reduce the absolute transport time-of-flight of the SE and therefore to reduce this contribution. Two sets of simulations were performed to estimate σ(spatial) and σ(velocity) independently:

1. The initial position of SE on the foil is set as homogeneous. Initial energy distribution of SE is excluded, therefore electrons fly to the MCP detector with K_0=0. In such simulations the contribution from spatial distribution of SE to the transport time is estimated as σ_{branch}(spatial)=31 ps for K=700 eV (see Figure 3.8 a).

2. To simulate a contribution from the velocity spread of SE, *ITSIM* parameters were set in such way that all electrons start from one point in the middle of the foil with Maxwellian distribution of initial velocities. In this way the spatial distribution is neglected and the contribution from the velocity spread is calculated as σ_{branch}(velocity)=18.5 ps for K=700 eV (see Figure 3.8 b).

The functional dependence between time spread and contributions from initial spatial and velocity distributions of secondary electrons is expected

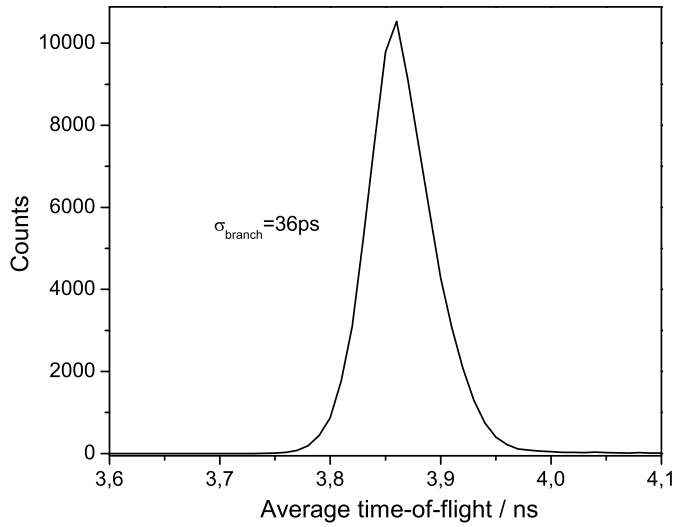

Figure 3.7: Result of the simulated transport time-of-flight distribution of 10^4 electrons by *ITSIM*. In the simulation homogeneous distribution of SE on the foil surface and initial kinetic energy distribution K_0=0-50 eV is included. σ_{branch} is calculated for K=700 eV and is equal to 36 ps. Note that the simulation includes only the contribution from the electron transport.

as

$$\sigma(Spatial) \propto T \propto \frac{1}{v} \propto \frac{1}{\sqrt{K}}. \tag{3.4}$$

$$\sigma(velocity) \propto T \propto \frac{1}{v^2} \propto \frac{1}{K} \tag{3.5}$$

In Figure 3.8 a) and b) the simulated contributions from initial position of electrons on the foil surface and initial velocity spread is shown with black squares in dependence on the kinetic energy. The results of the simulations for K=700 eV kinetic energy are indicated with violet color. From the figures it is clear that by increasing the kinetic energy K the time spread decreases in both cases. The red lines show the fit functions according to eq. 3.4 and eq. 3.5. These functional dependencies describe well the simulated results, the relative uncertainties are estimated as 8% and 2.5% respectively. By adding up quadratically both components σ(spatial) and σ(velocity), eq. 3.3 for the timing contribution from electron transport can be written as

$$\sigma(Transport) \propto \sqrt{\frac{C_{\text{spatial}}}{K} + \frac{C_{\text{velocity}}}{K^2}}, \tag{3.6}$$

where $C_{spatial}$ and $C_{velocity}$ are constants.
In Figure 3.9 the results of the simulations including both components are shown with blue circles. The blue line indicates a fit function according to eq. 3.6.

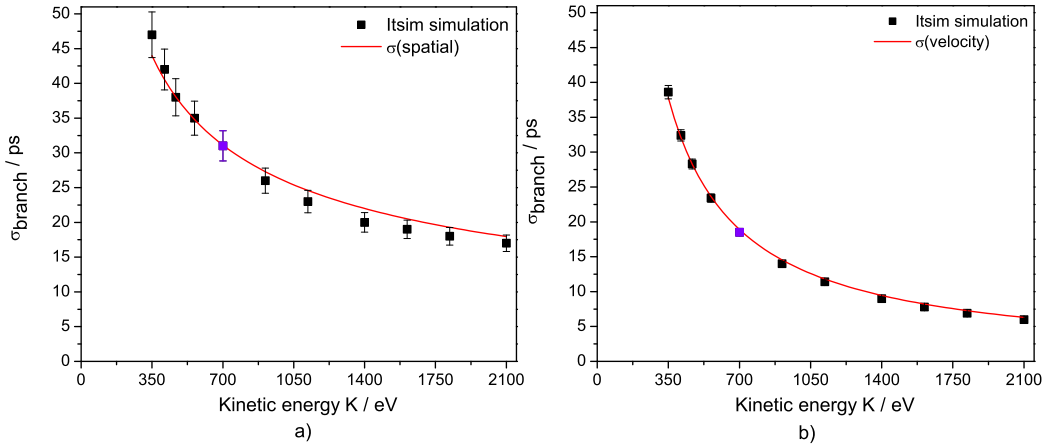

Figure 3.8: a) Simulated σ_{branch} caused by the spatial distribution of SE on the foil in dependence on their kinetic energies K. In the simulations all SE start with homogeneous spatial distributed on the surface of the foil and K_0=0. b) Simulated σ_{branch} caused by the velocity spread of SE as they are emitted from the foil. In this case all SE are emitted from one point in the middle of the foil and start with Maxwellian distribution of initial velocities. In both cases the kinetic energy of SE K is varied by changing the acceleration voltage between the foil and MCP detector. Simulated values are shown with black squares and the red curves indicate the fit functions from eq. 3.4, eq. 3.5.

To observe the relation between the transport time-of-flight of SE and their kinetic energy the coincidence time-of-flight distribution was experimentally measured for the range of kinetic energies K=350 - 1400 eV. For this purpose the TOF detector was currently upgraded for the higher values of electric and magnetic fields. More detail explanation of all technical components is presented in [Diw 11]. The measured corresponding standard deviation for the range of kinetic energies mentioned above is shown with red triangles in Figure 3.9. It is certainly seen that the σ_{branch} is reduced from 62 ps (at K=350 eV) to 37 ps (at K=1400 eV). From these results it follows that increase in potential difference between the foil and MCP detectors leads to a decrease in time spread cased by the contribution from the transport time of SE (eq. 3.3). Experimental data were measured for MCPs with 10 μm pore size with α-particles using *Ddelay* math function. The error of the experimental data are calculated as quadratical sum of the errors from the Gaussian fit, bin size and a statistical error over 1000 events and it is in the order of ±2-4 ps.

Comparison between the simulations and the experiments shows the presence of additional contributions, that are the transit time of SE through

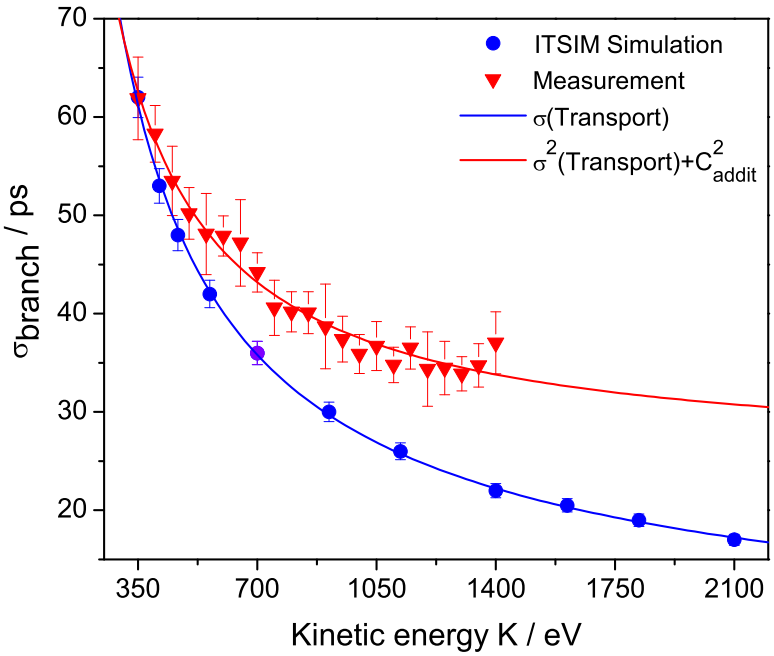

Figure 3.9: Results of simulations (blue circles) and measurements (red triangles) of the spread in time-of-flight of SE between forward and backward MCP detectors as a function of kinetic energy. The kinetic energy K is varied by changing the acceleration voltage between the foil and MCP detector. Note that the simulations include only the contribution from the transport time of SE. At the measured range of kinetic energies K=350-1400 eV the corresponding time spread σ_{branch} is reduced from 62 ps to 37 ps. The red and blue lines show the fit of the measured data and simulated data of σ(Transport) according to eq. 3.7 and eq. 3.6.

the MCPs and contribution from event time determination, which cause the time spread in time-of-flight, and which were observed in the experiment additional to the electron transport time, that is included in the simulations. By fitting the experimental data with a function from eq. 3.6 and adding quadratically additional constant C_{addit} one can estimate the contribution from those two components (eq. 3.3) to the time spread

$$\sigma_{branch} = \sqrt{C_{spatial}/K + C_{velocity}/K^2 + C_{addit}^2}. \tag{3.7}$$

The result of the fit is shown with a red curve and C_{addit} is equal to

$$C_{addit} = \sqrt{\sigma^2(MCP) + \sigma^2(ETD)} = 25ps. \tag{3.8}$$

For further improvements in transport time of SE, namely reduction of σ_{branch}(Transport) to a value down to 17 ps, the TOF detector is under

preparation for the measurements with 3 times higher electron kinetic energies (2100 eV) than the present value.
To see the effect from reduction of spatial contribution of SE the coincidence time-of-flight between the forward and backward MCP detectors was measured with coincidence to the silicon (Si) detector. The Si-detector is installed behind the foil and has smaller active diameter of 15 mm compared to the 40 mm foil diameter (Figure 3.2). First the number of counts from the MCP detectors were measured in coincidence with the Si-detector ($N_{MCP_F\&MCP_B\&Si}$) and according to the illuminated area of the Si-detector the area of the foil illuminated in the measurements were calculated. Then two different apertures with ∅=4 mm and ∅=2 mm were installed in front of the Si-detector and the measurements were repeated. The results of the measurements are summarized in Table 3.1.

∅ Si	N_{Si}	$N_{MCP_F\&MCP_B\&Si}$	∅ foil	σ_{branch}
15 mm	13620	7592.5	11.2 mm	46 ps
4.6 mm	1468	668	3.3 mm	43 ps
2 mm	354	166	1.4 mm	41 ps

Table 3.1: Summary of the measurements of the count rate from the MCP detector in coincidence with Si detector $N_{MCP_F\&MCP_B\&Si}$. Complete area of the Si-detector (∅ 15 mm) and reduced with ∅ 4 mm and ∅ 2 mm apertures was illuminated to estimate the corresponding illuminated area of the carbon foil by α-particles used in coincidence time-of-flight measurements.

In the coincidence time-of-flight measurements by triggering on the Si-detector with certain area (Table 3.1) one selects coincidence signals from the inner part of the foil what makes possible to estimate the time spread as a function of the illuminated foil area. According to the simulations (Figure 3.10, black squares) by illuminating the inner part of the foil one decreases the contribution from the spatial distribution of the SE over the foil area. Figure 3.10 (red circles) shows the results of the measured coincidence time-of-flight as a function of illuminated foil diameter. σ_{branch} is obtained as 46 ps for illuminated ∅ 11.2 mm (98.46 mm^2), 43 ps for illuminated ∅ 3.3 mm (7.56 mm^2) and 41 ps for illuminated ∅ 1.4 mm (1.5 mm^2) of the foil by α-particles.

3.1.2 MCP Transit Time

To investigate the contribution $\sigma(MCP)$ from the transit time of secondary electrons through the MCP channels the measurements of the signal shape are performed using MCPs with the same active diameter of 40 mm but

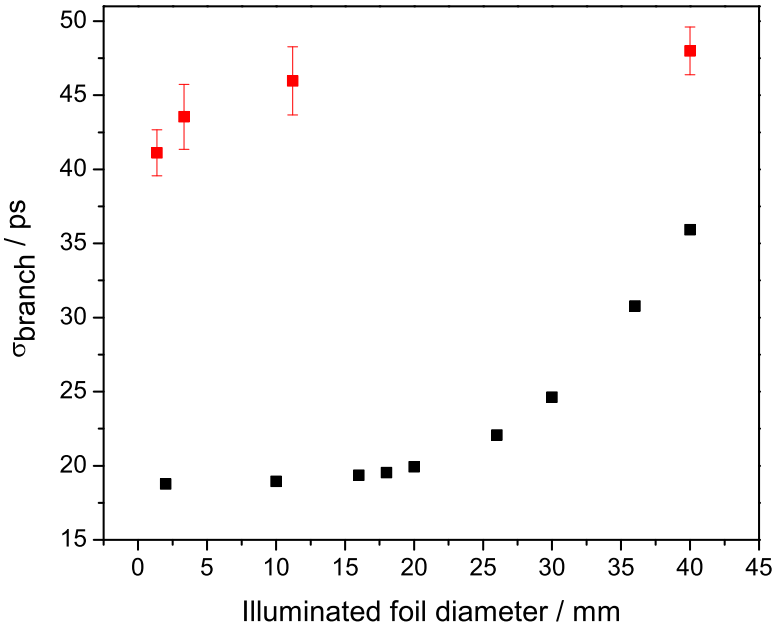

Figure 3.10: Simulated a) and measured b) σ_{branch} of the coincidence time-of-flight distribution as a function of the illuminated foil diameter by α-particles. Note that in the simulations only contribution from the transport time of SE is included and in the measurements additional contributions according to eq. 3.1 appear. The illuminated diameter of the foil is calculated from the coincidence count rate measurements with Si-detector (Table 3.1).

with 10 μm and 5 μm channel diameters. The assembly in both cases uses a two-stage MCP in chevron configuration. Used MCPs with 5 μm pore size have L/d=60:1, while the MCPs with the channel diameter of 10 μm have L/d=40:1. The thicknesses of two-stages MCP are very small, 0.3 mm and 0.4 mm respectively, which corresponds to the electron transit distance. Comparison between MCP signal shapes indicates slightly better rise time of 480 ps for the MCPs with 5 μm pore size than 593 ps measured using MCPs with 10 μm pore size. What is about 20 % difference. Additionally the rise time of the MCP signals is influence by the bandwidth of the detector. This contribution will be investigated in the next section.
The emission of secondary electrons in the MCP channel is a random process giving rise for different trajectories of different electrons. Each of the electrons have different transit time through the channels. If there are many SE, created from the foil, the mean transit time will not vary very much from event to event. In case of a few initial SE the mean transit time of them will vary significantly from event to event giving a large spread in

transit times through the MCP. The time spread in the electron transit time through the MCP channels scales proportionally to the channel diameter and inversely proportional to the number of secondary electrons

$$\sigma_{MCP} \approx \frac{d}{\sqrt{n_{se}}}, \tag{3.9}$$

where d is the diameter the MCP channel, n_{se} is the number of secondary electrons produced from the foil and detected by first microchannel plate [Ina 06] [Vav 08]. In particular, this means that depending on the charge number of the projectile different numbers of SE will be emitted from the foil and thus the electrons will propagate through the MCP with different spreads in transit time. The calculated results for the dependence of forward (F) and backward (B) electron yields on the carbon foil thickness are presented in Figure 3.11 a) for $^{91}Kr^{36}$ ions of 382 MeV/u (blue lines) and α-particles of 1.145 MeV/u (red lines). The results concerns the evolution of the yield of fast δ electrons with projectile velocity. This holds for thicker targets, where both charge equilibrium and complete development of the secondary electron cascade are reached. For thinner targets, the contribution is smaller, but increase with increasing target thickness [Jun 96].
The coincidence time-of-flight between forward and backward MCP detectors as a function of forward secondary electron yields was measured with α-particles. The energy of the secondary electrons were equal to K=700 eV. The results of the measurements are shown in Figure 3.11 b). The corresponding foil thicknesses are indicated as 10 for 10 $\mu g/cm^2$, 37 for 37 $\mu g/cm^2$ and 55 for 55 $\mu g/cm^2$. In case of the measurements with the carbon foils (black squares) slightly better σ_{branch} of 44 ps is measured for 37 $\mu g/cm^2$ compared to 46 ps measured using thickness of 10 $\mu g/cm^2$. But both results coincide within the error bars. For a foil with a Cs-compound on the surface (pink square) with thickness of 55 $\mu g/cm^2$ the standard deviation is measured as 31 ps. The measurements were performed using *Ddelay* math function on LeCroy digital oscilloscope (1 GHz, 10 Gsamples/s). Examples of the time-of-flight distributions measured with 10 $\mu g/cm^2$ carbon foil and a foil of 55 $\mu g/cm^2$ with a Cs-compound on the surface are shown in Figure 3.12. The standard deviations σ_{branch} according to eq. 3.2 were calculated from the Gaussian fit functions (red curves). The results are explained by emission of about 28 secondary electrons from the foil with a Cs-compound on the surface, that is more than 9 times higher than in case of carbon foil. For this case the number of emitted secondary electrons is determined by comparison between the mean signal amplitude obtained from the pulse-height-distribution of the signals from forward MCP detector from a carbon foil and a foil with a Cs-compound on the surface. The number of SE emit-

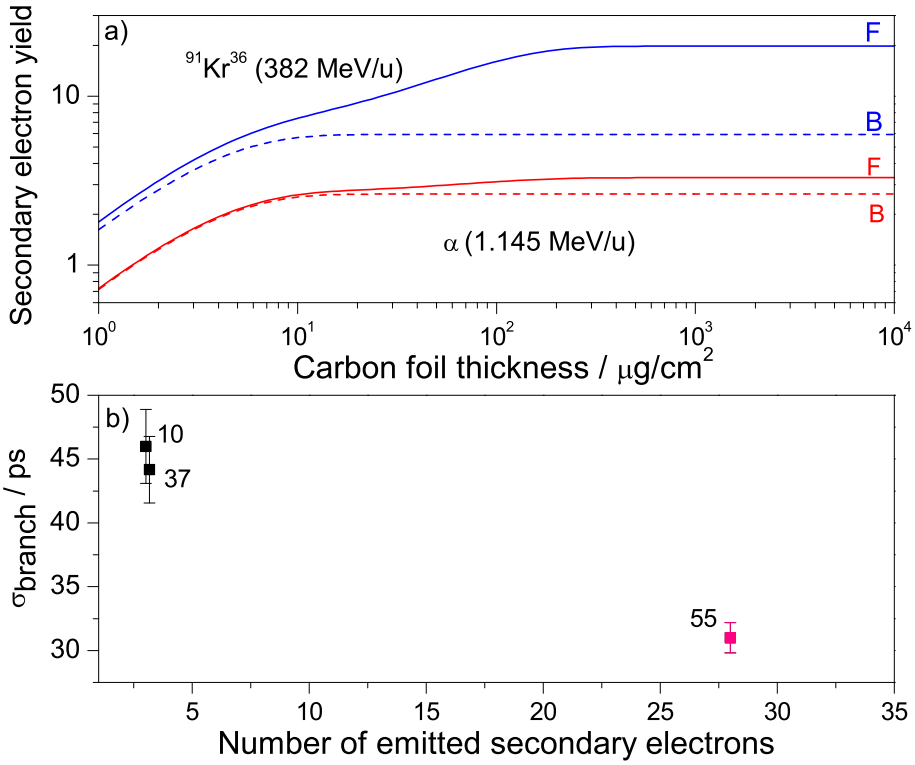

Figure 3.11: a) Calculated results for forward (solid lines) and backwards (dashed lines) electron yields obtained with $^{91}Kr^{36}$ projectile of 382 MeV/u (blue lines) and α-particles of 1.145 MeV/u (red lines) as a function of carbon foil thickness. Both the foil thickness and yield scale are logarithmic. b) Measured σ_{branch} of the coincidence time-of-flight distribution between MCP forward and backward detectors with α-particles as a function of the forward secondary electron yields. By 10 and 37 the thicknesses of the carbon foils of 10 $\mu g/cm^2$ and 37 $\mu g/cm^2$ are indicated. The number of SE from the carbon foils is calculated according to eq. 2.28. By 55 the thickness of a foil of 55 $\mu g/cm^2$ with a Cs-compound (pink square) on the surface is indicated. For this foil determination of the number of SE is explained in the text. The complete foil area was illuminated by α-particles.

ted from the carbon foil is calculated according to eq. 2.28.

For twice higher kinetic energy of the secondary electrons of K=1400 eV the standard deviation σ_{branch} with this thick foil is measured as 27 ps. Note, that with this thicker foil and higher kinetic energies of the secondary electrons, both contributions from the transport time of SE σ(Transport) and from the transit time of SE through the MCP channels σ(MCP) are improved.

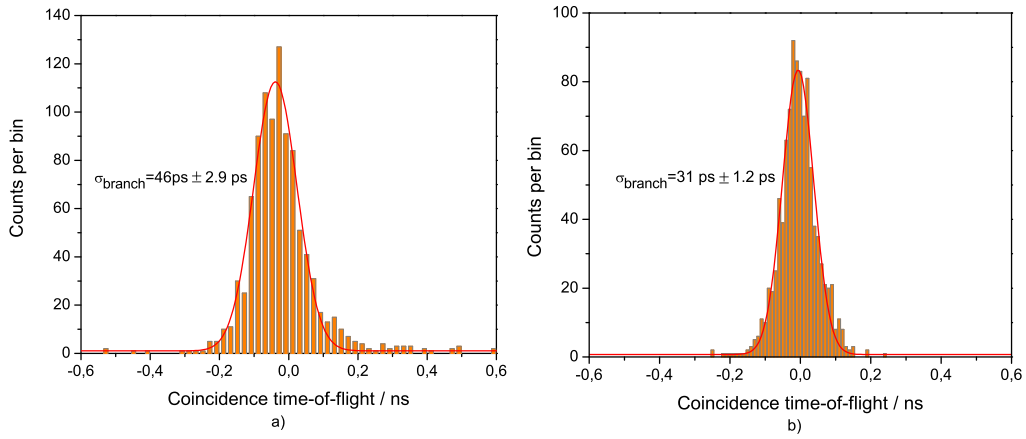

Figure 3.12: Measurement results of the time-of-flight distribution between forward and backward MCP detectors with a) carbon foil of 10 $\mu g/cm^2$ and b) a foil of 55 $\mu g/cm^2$ with a Cs-compound on the surface. The measurements were done using *Ddelay* math function and with an aperture of the α-source to fully illuminate the foil. The kinetic energy of the secondary electrons was equal to K=700 eV. The event times for forward and backward detectors were subtracted and plotted as a histogram (red color). In the histogram the sizes of a bin are chosen to be 20 ps and 10 ps, respectively. The standard deviations of the coincidence time-of-flight distributions are calculated from the Gaussian fit functions (red curve) and indicated in the figure together with the errors.

3.1.3 Event Time Determination

For the measurements with the MCP detectors one has precisely determine the event time of each individual signal. Certain difficulties can appear in the signal treatment and one has to take care about the following:

- Amplitude / rise time walk effects lead to the error in the determination of the event time of the signal (Figure 3.13);
- A suitable sampling rate of the acquisition system has to be chosen. To accurately digitize the incoming signal, the oscilloscope's real-time sample rate should be at least three to four times the oscilloscopes's bandwidth [Nat 09];
- To minimize amplitude / rise time walk effects an appropriate timing algorithm have to be applied for accurate event time determination of the signal (see Sec. 4.3.1 and Appendix).

The main difficulties in the precise event time determination caused by amplitude and rise time walk effects are explained in Figure 3.13. In the

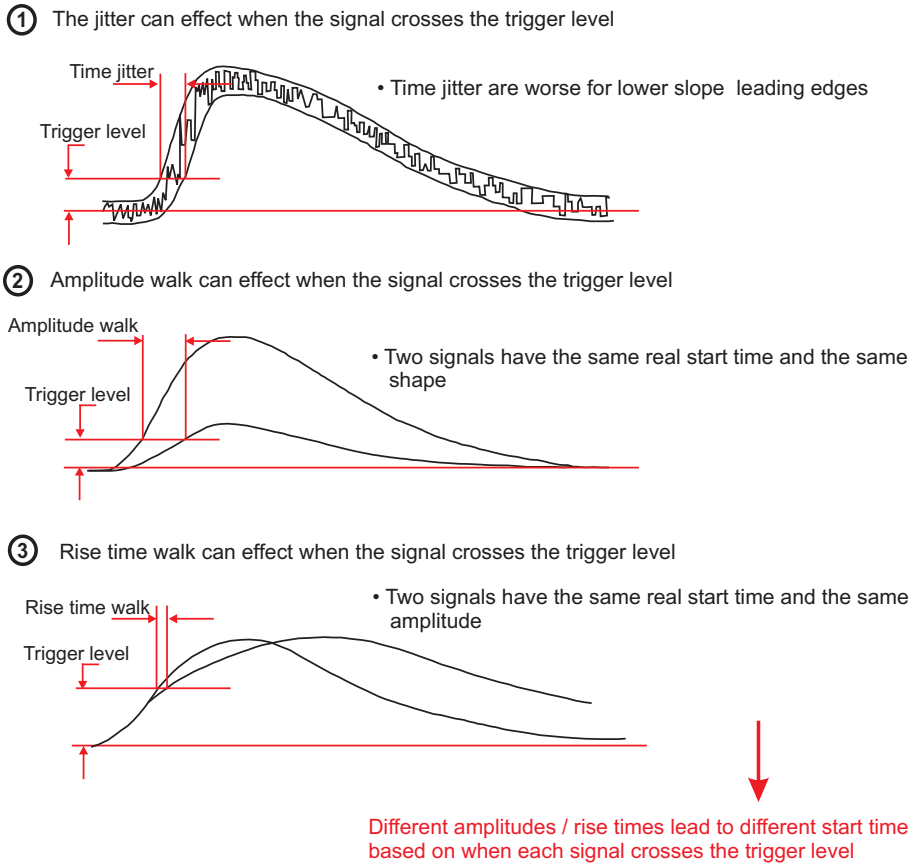

Figure 3.13: Main errors in determination of the event time. When the arrival time of the signal is of more interest than the signal amplitude one has to minimize those uncertainties. Time jitter, amplitude and rise time walk effects are explained [Edw 07].

following only the signal shape will be investigated and optimized.
Simulations with CST MICROWAVE STUDIO [CST] of the MCP detector show that the bandwidth of the detector and thus the timing performances are limited by the design of the anode as well [Aye 10] [Aye 11]. Large parasitic capacitances between the anode cup, anode plate and MCPs prevent high frequency signals (small rising slope) from passing through the microchannel plate detector and from being detected by the anode. Based on this knowledge, a new improved anode design was developed to optimize the bandwidth of the detector and with this the MCP signal quality.
Figure 3.14 shows the simplified schematic view of the MCP detector with parasitic capacitances. For better timing performance one has to decrease all values of capacitances and inductors as much as possible. Also the ratio between those values has to be taken into account. For instance C_{dAS1}, C_{dAS2} and L_{dAS1} depends on the length between the anode plate and anode cup d_{AS1}. In case of increase of d_{AS1} the capacitance C_{dAS1} decreases, while the inductance L_{dAS1} will increase as it scales proportionally to d_{AS1}.

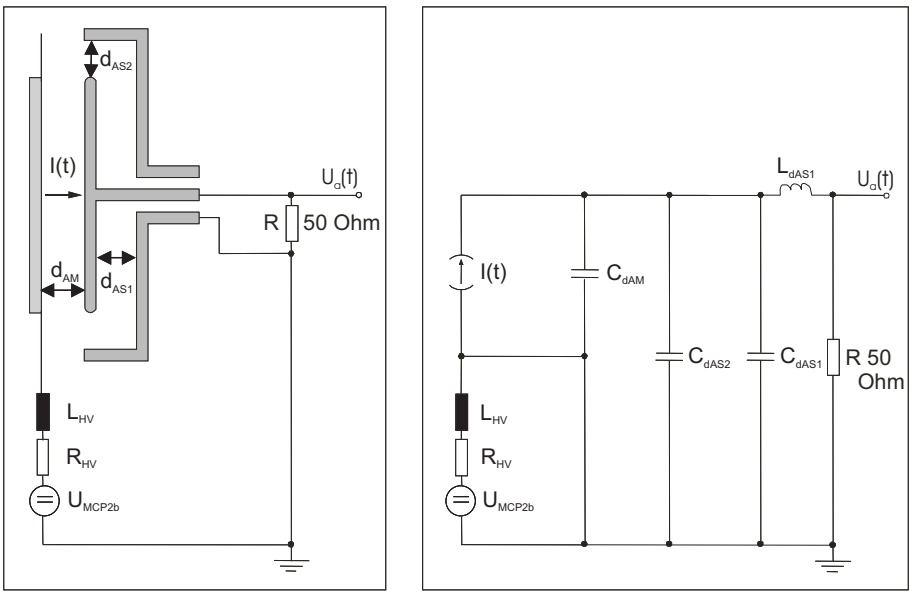

Figure 3.14: Simplified circuit diagram of the MCP detector [Pla 09]. The values C_{dAS}, C_{dAM} and L_{dAS1} are parasitic capacitances and inductance. The ratio of distances d_{AS1}, d_{AS2}, d_{AM} influences on the anode bandwidth and has to be improved.

Figure 3.15: Picture of the previous (left part) and new optimized for signal shape (right part) anode designs for the MCP detector.

Figure 3.15 shows the pictures from previous and new optimized anode designs.

On the left part of Figure 3.16 cross sections of the MCP detector anode used in the simulations using CST MICROWAVE STUDIO [CST] are shown. In the simulations an input signal with certain power is applied through the circulator to the SMA connector of the MCP detector and flows through the anode. The frequency was swept through the anode. The power of the signal transmitted through the anode (blue curve) and the power of the reflecting signal were simulated. At the reference level of -3dB the cut-off frequency f_C was determined as $f_{C1} \approx$ 0.5 GHz for previous (upper part) and $f_{C2} \approx$ 3 GHz for new (lower part) anode designs. The cut-off frequency

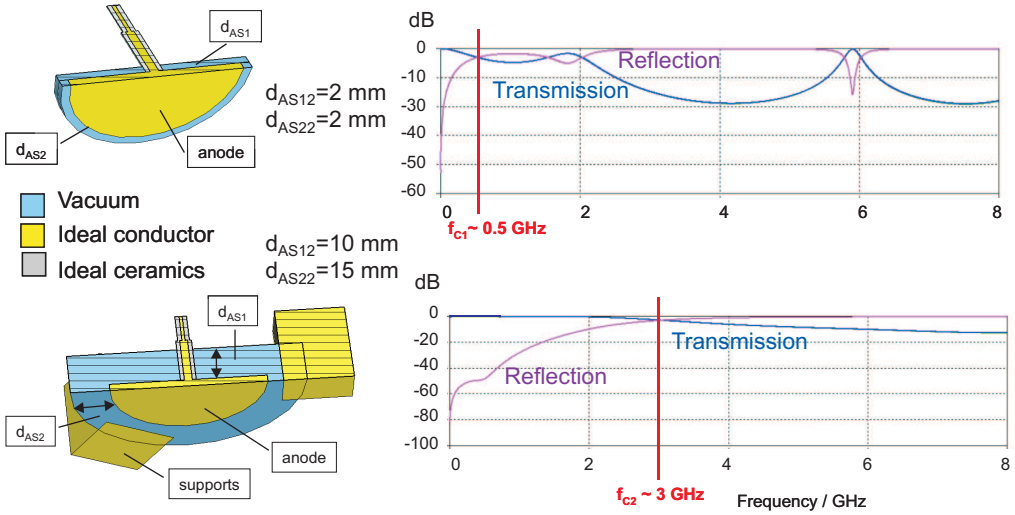

Figure 3.16: Schematic view of the anode designs and results of the simulations with *CST MICROWAVE STUDIO* [Aye 10]. The distances d_{AS1}, d_{AS2} influence on the anode capacitance and have to be reduced. The reflecting power was determined in the simulations for the previous (upper part) and for the new (lower part) anode designs. The blue curve corresponds to the signal power that flows to a 50 Ω termination connected to the ground; pink curve shows the signal power, which was reflected. At the reference level of -3dB the cut-off frequency f_C is calculated, which corresponds to the fall of the signal power by about half value.

f_C is the frequency either above or below which the power flowing through the system begins to be reduced (or reflected) rather then passing through. Referred to -3dB level the f_C corresponds approximately to the reduction of the power by half. The cut-off frequency defines the anode bandwidth.
To verify the predictions from the simulations a test with a *NETWORK ANALYZER* (RF Power Meter Wiltron 6747A) [Aye 10] [Aye 11] was performed (Figure 3.17). The test was done with the signal from the opposite side of the anode while during the real experiment the charge is collected on the anode plate. The test with *NETWORK ANALYZER* is done in a similar way as the simulations with *CST MICROWAVE STUDIO* program. An input signal with a certain power is applied through a circulator to the SMA connector of the MCP detector and flows through the anode cup to a high performance 50 Ω termination connected to the ground. The frequency was swept (RF Sweeper Wiltron 561) through the anode and the power of the reflecting signal was measured. If we assume that the power of input signal is equal to 1, the power of the signal which flows to the 50 Ω termination equals x and of the reflecting signal equals y, then $1 = x + y$. This assumption fulfills the condition for an ideal system without losses and can be applied to our anodes due to the small path length of the signal.

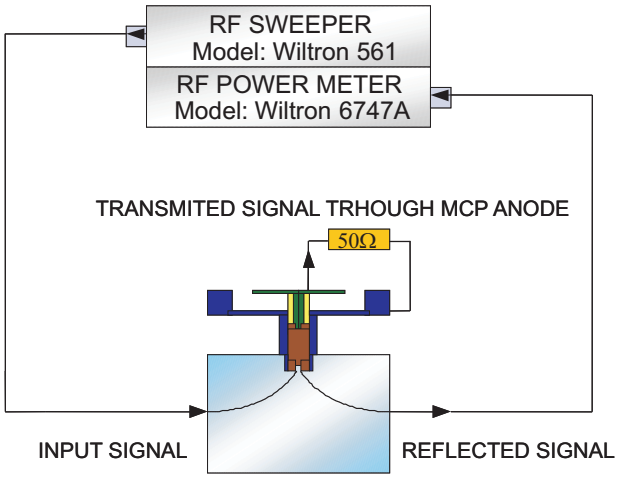

Figure 3.17: MCP anode test with a *NETWORK ANALYZER* [Aye 10]. An input signal with a certain power is applied through a circulator to the SMA connector of the MCP detector and flows through the anode cup to a high performance 50 Ω termination connected to the ground. The power of the reflecting signal is measured and supposed to be equal to the one of the input signal. The limiting bandwidth is a range of frequencies in which the power of the reflecting signals are still the same as the ones from the input signals. For a new anode it is equal to approximately -2dB and is about 2 times higher than from the previous anode construction.

At the reference level of -3dB the cut-off frequency f_C was measured for previous as 900 MHz and 2 GHz for new anode designs. Therefore, the new anode should improve the bandwidth of the MCP detector by a factor of 2. In terms of signal quality f_C at -3dB level corresponds to the half width at half maximum of the signal as [Phoa]

$$FWHM_{min} = \frac{1}{f_C(-3dB)}. \tag{3.10}$$

The MCP signals with previous and new anode constructions were investigated at the setup with an electron source (Figure 3.22). Figure 3.18 shows the comparison between the signal shapes from the MCP detector with both anode designs.

During the test with the new improved anode design signals with better rising slope and width were observed. The measurements show that with optimized ratios between capacitances C_{dAS} and C_{dAM} of the anode the FWHM of the signal peak can be reduced by a factor of up to two (in this case from 1 ns to 600 ps) and rising slope improved by about of 20% (from 600 ps to 460 ps).

Table 3.2 summarizes the results from the simulations with *NETWORK ANALYZER* and from measurements. As one sees the measured width of

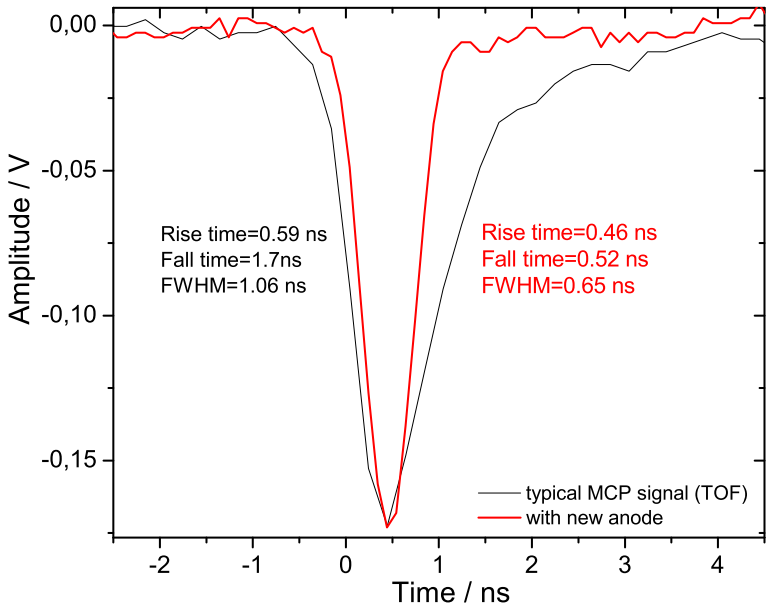

Figure 3.18: Signal shapes from the previous (black line) and new (red line) anode designs measured at the setup with an electron source (Figure 3.22). The tests show that by decreasing the capacitance between the anode and the MCPs the peak width can be reduced by a factor of up to two and the rise time improved from 600 ps to 460 ps, which is about 20%. Note that the signals were acquired by a 1GHz oscilloscope.

the MCP signal is broader than the calculated one. The difference is explained by the fact that simulation is an ideal case where ideal conductors and ideal ceramics were considered as components of the anode design. In the real measurements every component in the system needs to have a bandwidth greater than the -3dB bandwidth of the signal. A simple rule is to have a frequency -3dB bandwidth greater than 0.44/FWHM(signal). So, the signal width one measured depends on the convolutions of many bandwidth, including those of the signal and the oscilloscope. It means that even the fastest scope will have an internal $FWHM_{scope}$. To maintain the fidelity of the measurements in first order one has to subtract the internal $FWHM_{meas}$ of the oscilloscope from the measured value. It has to be considered that for these measurements a digital oscilloscope with a bandwidth of 1 GHz was used. The calculated results is shown in the third column. Further reduction of the measured MCP signal parameters is expected for the measurements with an oscilloscope with larger bandwidth.
The time walk effects are smaller for signals with smaller rise times [Vav 08].

Anode design	$FWHM_{calc}$	$FWHM_{meas}$	$\sqrt{FWHM^2_{meas} - FWHM^2_{scope}}$
Previous	1.1 ns	1.06 ns	964 ps
New	500 ps	646 ps	473 ps

Table 3.2: Calculated and measured timing parameters of the MSP detector signals from the previous and new anode designs. With new optimized anode design the FWHM of the signal peak is reduced by a factor of up to two. The third column shows the $FWHM_{meas}$ of the measured signal with subtracted internal $FWHM_{scope}$ of the oscilloscope.

Thus the improvements of about 20% in rising slope of the signal from the new anode design should improve precision of the event time determination of the MCP signals by 20% and so the mass measurement accuracy. While with smaller value of the falling slope a better separation of close lying, in particular of significant different amplitude signals can be performed during a data analysis.

3.2 Efficiency Measurement with a Laser Beam

The first settings of the electric and magnetic fields applied in the TOF detector was optimized empirically by [Tro 93] and used for several years. Simulations by [Fab 08] showed that new optimized electrode voltages and magnetic field setting increases the active foil area to produce secondary electrons and so increases the detection efficiency up to 80%. Table 3.3 summarizes main potentials and magnetic fields applied in the TOF detector according to setting by J. Trötscher and B. Fabian.

Detector settings	U^{++}	U^{-}	U_{Foil}	U_{MCP}	I_{Magnet}
Previous by [Tro 93]	5244 V	-2016 V	-3400 V	-2700 V	1.7 A
New by [Fab 08]	5100 V	-2700 V	-3400 V	-2700 V	1.8 A

Table 3.3: Electrode potentials and magnetic fields for the previous optimized empirically and for the new optimized by simulations TOF detector settings.

To confirm the simulation results, position sensitive measurements with a laser beam were performed.
The secondary electrons generated by photons can only overcome the surface barrier, if their energy exceeds the work function Φ. In case of a carbon foil the work function is equal to 4.5 eV. To obtain enough photon energy the suitable wavelength of λ=266 nm (E=4.66 eV) is available from manufac-

tures. For the measurements a nitrogen laser MNL 100 (LTB Lasertechnik Berlin) was used with a wavelength of 372 nm and 3 ns pulse width. The maximum energy of the laser was measured with a Micro Joule Meter (LTB Lasertechnik Berlin) and it is about 65 μJ. The laser system was calibrated according to this value. The main parameters of this laser is summarized in the Table 3.4.

Laser parameters	Specification	Used in measurements
Wavelength	337.1 nm	337.1 nm
Pulse energy	65 μJ	1.15 μJ
Average power	2 mW	11.5 μW
Repetition rate	10 - 30 Hz	10 Hz
Pulse - FWHM	3 ns	3 ns
Beam dimension	3 x 4 mm	3 x 4 mm

Table 3.4: Main parameters of the nitrogen laser MNL 100. In the second column the performance of the laser according to the specification is shown. The laser parameters used in these measurements are indicated in the third column.

To produce several secondary electrons from the carbon foil the energy of the laser beam was set to 1.15 μJ and 10 Hz repetition rate. As the energy of the photons from this laser is not enough to emit the SE from the carbon foil but the signal is observed at each laser pulse it is assumed that the part of the carbon foil was evaporated by an ablation and detected by the MCP detectors. It was enough to produce visible single ones and to count it.
The schematic view of the set up used for the efficiency measurements is shown in Figure 3.19. The foil area was scanned with a laser beam and the efficiency on the different parts of the foil was measured. NIM signals from both MCP detectors were produced with CFDs (CANBERRA QCFD 454) and set into coincidences with a logic AND-module (C.A.E.N Quad Coincidence Logic Unit 455). The frequency of the laser was set to 10 Hz. One of the detector was used as a START signal and the other as a STOP signal. Coincidences between START and STOP signals were counted by counters (ORTEC Dual Counter/Timer 994).
The laser beam was focused by a lens with a focal length of 400 mm. To produce a parallel beam the aperture in front of the focusing lens was used. The windows with a good transmission of electromagnetic radiation in UV range were installed from both sides of the TOF detector chamber on the path of the laser beam. To monitor the beam position a special paper was placed on the opposite side of the chamber. Schematic top view of the apparatus for the efficiency measurements with laser beam is shown in Figure

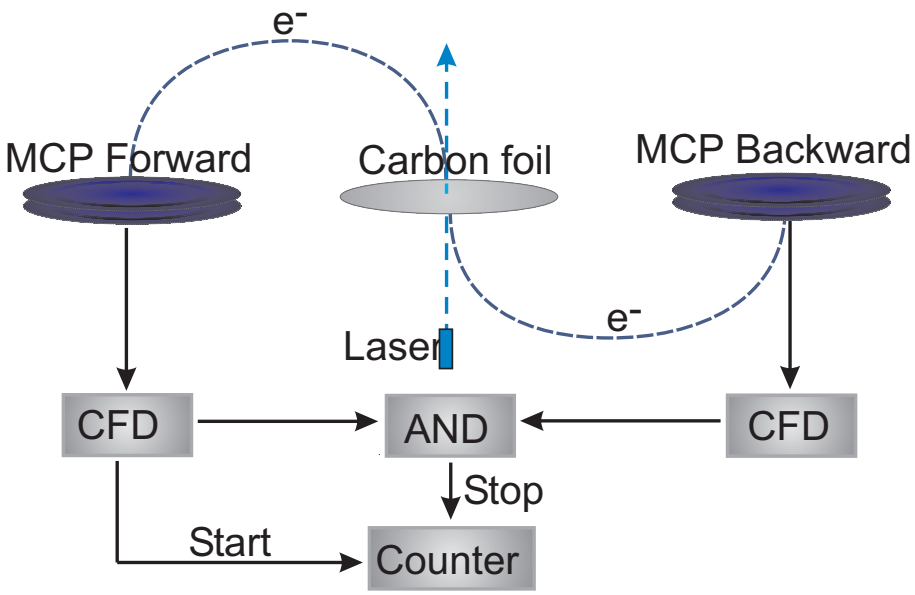

Figure 3.19: Schematic view of the setup used for efficiency measurements with a laser beam. As a result of an atomic ablation after shooting the laser beam on the foil the secondary electrons were produced and detected by both MCP detectors. With the Constant Fraction Discriminator standard NIM signals were produced and set into coincidences using a logic AND-module of the company CAEN. The laser was set to produce pulses during one minute. One of the detector with maximum number of counts was used as a START signal and the other as a STOP. The coincidences between START and STOP signals are counted by ORTEC Counters.

3.20.

The efficiency is measured for previous and new optimized by simulations voltage and magnetic field settings. The results of the measurements (lower part) as well as corresponding simulations (upper part) are shown in Figure 3.21.

The experimental measurements confirm the simulation results that with previous empirical setting of the voltages and magnetic fields the foil area was asymmetrical and only the electrons produced at one part of the foil could be detected by the MCP detectors. For the new optimized by simulations setting [Fab 08] the measurements show that the SE produced from the whole foil area will be detected by the MCP detector and therefore the detection efficiency is increased up to 80%.

3.3 Rate Capability of the MCP Detector

Because of the high revolution frequencies of the ions in the ESR (∼2 MHz), the rate acceptance of the TOF detector is an important performance pa-

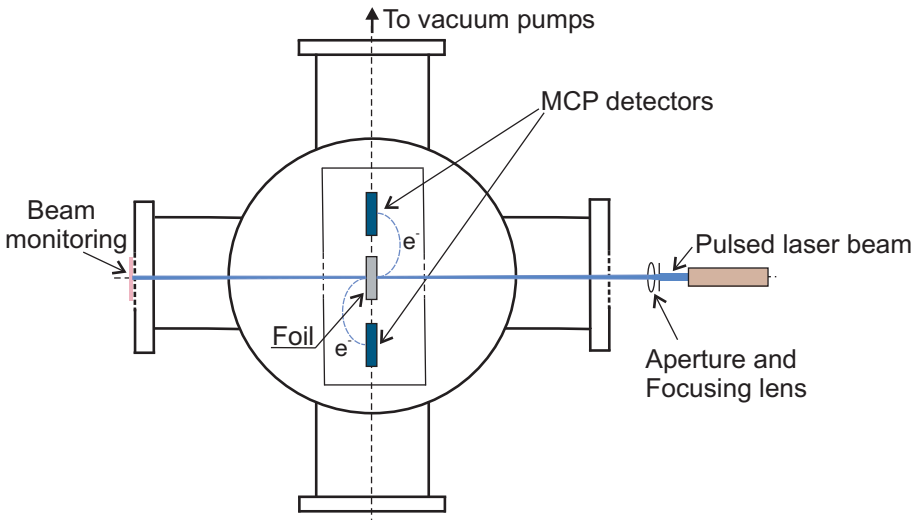

Figure 3.20: Schematic diagram of an apparatus for the efficiency measurements with a laser beam at the TOF detector. The chamber of the TOF detector, placement of the laser, an aperture and focusing length is shown.

rameter. It was determined and increased by a factor of 4.
A technique for making the channel diameter smaller is recently a promising method for improving the saturation characteristics of microchannel plates. The number of channels in the MCP N_{total} can be estimated as

$$N_{total} = \frac{\pi R^2}{\pi r^2}, \tag{3.11}$$

where R is the radius of the whole MCP and r is the radius of the single channel. If one decreases the channel diameter by 2, the number of channels in the MCP with the same area will increase by a factor of 4

$$N'_{total} = \frac{\pi R^2}{\pi (\frac{r}{2})^2}, \tag{3.12}$$

so $N'_{total} = 4N_{total}$. According to eq. 2.55 the dead time τ_{MCP} of the microchannel plate will be decreased proportionally with the number of channels.

3.3.1 Experimental Setup

The influence of the dead time effect on the rate capability of the MCP detector was examined experimentally on a setup with an electron source with variable electron beam (constructed by [Fab 08]). The cathode, in this case a tantalum wire, is heated by the current to a temperature high enough to cause electron emission as described by the Richardson equation

$$J = AT^2 e^{-\frac{W_e}{k_B}T}, \tag{3.13}$$

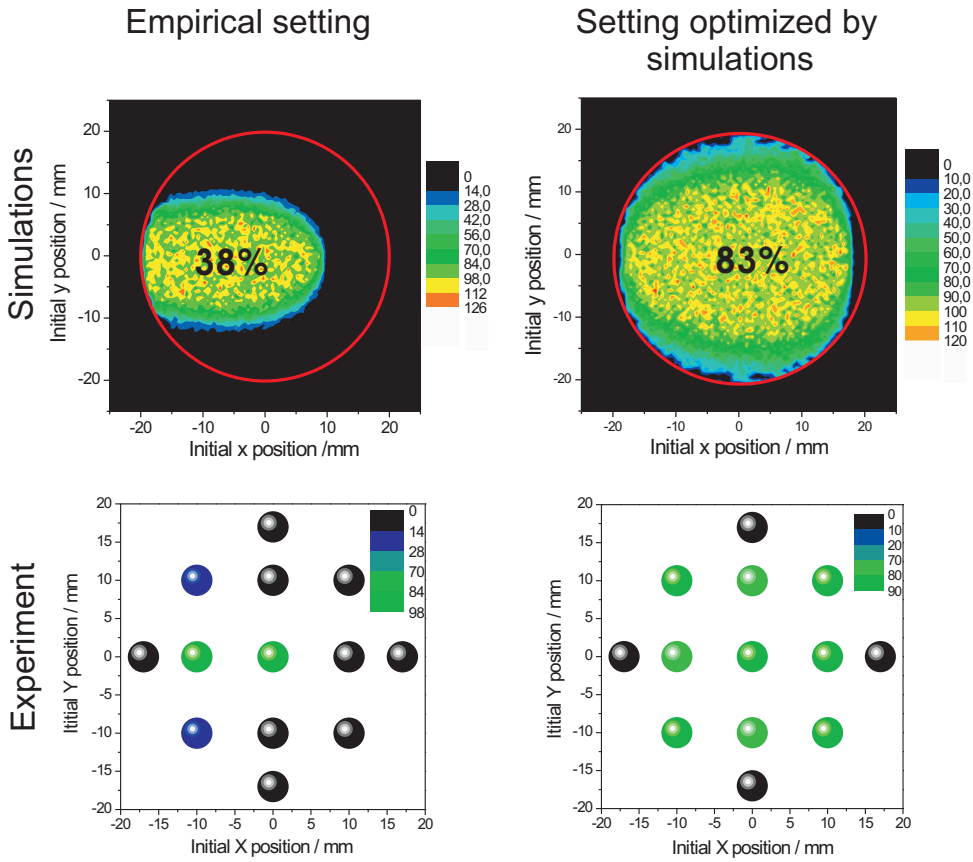

Figure 3.21: The results of the efficiency measurements (lower part) with a laser beam and corresponding simulations (upper part) [Fab 08]. The laser beam was moved to scan the whole area of the foil to the right, left and upper directions. As the detector is mirror symmetric the lower part was assumed to be equal with upper one. The efficiency values are indicated with a color spectrum and increase from black to green. Experimental measurements (lower part) confirmed the results of the simulations (upper part) that using previous empirical setting (left part) the active foil area was asymmetric while for a new setting the homogeneous active are of the foil is achieved (right lower part).

where J is the current density of the emitted electrons, A is the Richardson constant, W_e the work function, k_B the Boltzmann's constant and T the temperature.

Produced electrons are guided with the help of the potentials U_{Repeller}, U_{Plate}, $U_{\mathrm{Lens1,2,3}}$ and U_{Pipe} to the MCP detector as it shown in the Figure 3.22. Different heating currents (I_{Heating}) are applied to the tantalum wire to vary the number of electrons emitted and to be detected by MCPs. To make these measurements comparable to the experiment at the ESR the potential differences are chosen in such way that electrons arrive to the MCPs with about 700 eV. This 700 eV corresponds to the approximate

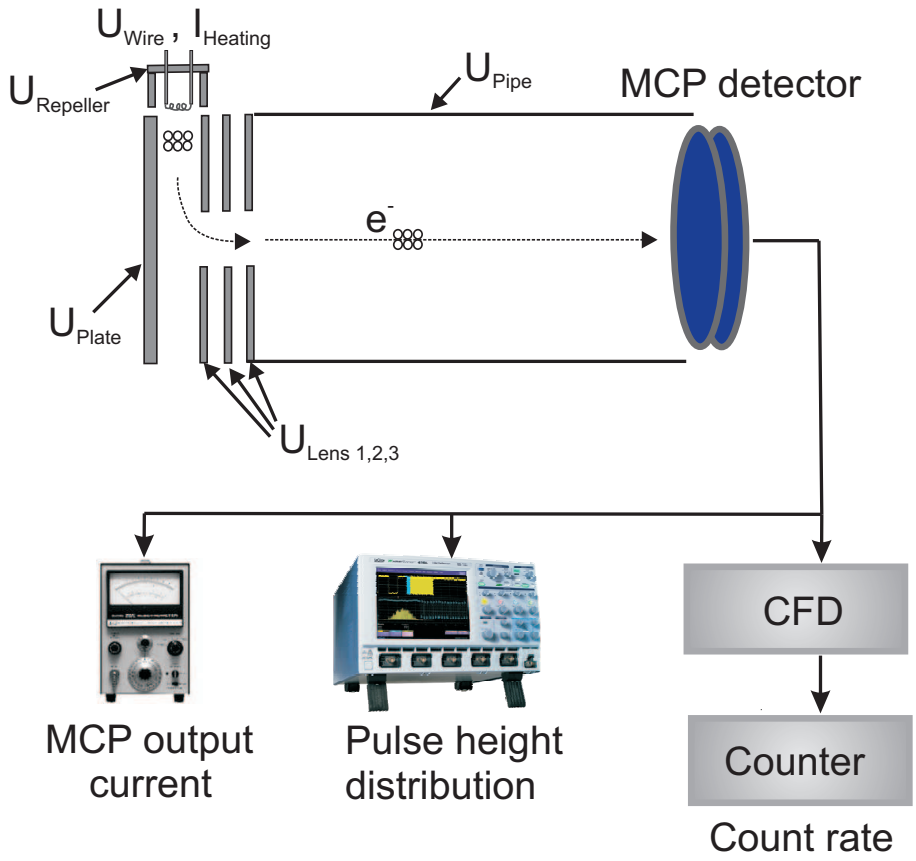

Figure 3.22: Schematic representation of the measurement setup and additional electronic devices for the count rate, MCP current and PHD measurements. By applying the heating current I_{Heating} to the tantalum wire electrons are produced by a thermal emission. With the help of potentials U_{Repeller}, U_{Plate}, $U_{\mathrm{Lens1,2,3}}$ and U_{Pipe} the electrons are guided through the drift tube to the MCP detector.

energy of the secondary electrons when they hit the MCPs in TOF detector at the ESR [Fab 08].

The MCPs set in Chevron configuration used in the measurements is shown in Figure 3.23. Because of the inhomogeneity of the beam in radial direction it was cutted with an additional diaphragm installed in front of the MCP plate with a diameter of 15 mm. All the results were scaled to the whole MCP area with a diameter of 40 mm. Some of the values were checked in the measurements without an aperture and they are in a good agreement with the scaling [Diw 09].

According to the previous studies the distance between two microchannel plates is chosen as L=1 mm and was a fixed parameter in the measurements. Variable resistances were connected to the bottom and top of the electrodes holding the MCPs. These resistances were used to set the voltages applied to every microchannel plate and to vary the voltage drop across the gap

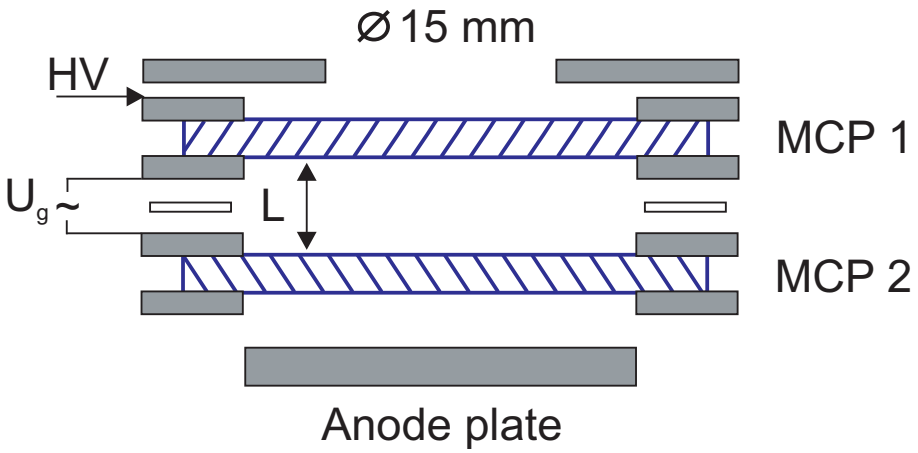

Figure 3.23: Cross sectional view of the MCP detector used in the measurements. Before the MCP plates the diaphragm with a diameter of 15 mm is installed to obtain a homogeneous electron beam distribution. The distance between the plates L=1 mm was fixed parameter in the measurements and the gap voltage U_g between the plates were varied from 7 V to 400 V.

between the plates. The acceleration voltages were applied to observe the influence from the strip current of the MCP and number of excited channels (Sec. 2.5.4.3). The following accelerating voltages between two MCPs were used: U_g=7 V, 100 V, 200 V and 400 V.

The rate of electrons hitting the MCP detector was varied by changing the heating current. For every applied heating current the number of counts per time, output current from the MCP detector anode and the pulse-height distribution were measured. The counts per time were measured by using a Constant Fraction Discriminator (CANBERRA QCFD 454) in combination with a counter (ORTEC Counter and Timer 871) for 1 minute. The MCP current was measured with Picoamperemeter (Keithley 610C Electrometer). The PHD was acquired and saved for every measurement with a digital oscilloscope (LeCroy Waverunner 6100A). An oscilloscope saves 1000 measured signal amplitudes in a histogram.

Our measurements show that the gain of the MCPs changes over time, in a nonlinear way. This aging effect is caused by the changes of the microchannel plate wall secondary emission coefficient, due to the electron scrubbing [Ref 05]. The MCP is only capable of emitting a limited number of electrons during its lifetime, and after a large number of electrons have been emitted, the gain is gradually reduced. To measure this aging effect and to avoid an influence of it on our studies the MCPs were bombarded continuously with electrons produced by a heating current of 1.6 A. At this heating current the count rate for the interplate voltage of 214V is approximately equal to

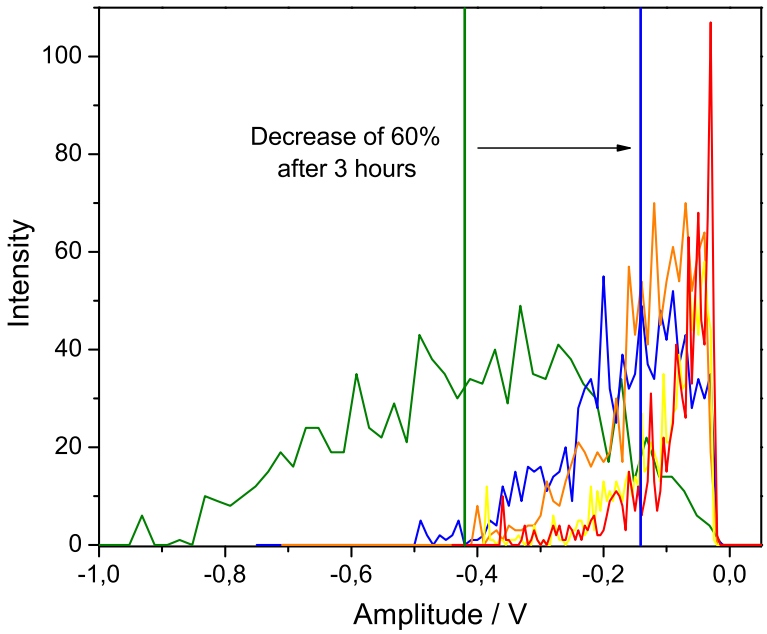

Figure 3.24: The PHD at the beginning of the measurements (green curve) and after 3 (blue curve), 4 (orange curve), 5 (yellow curve) and 6 (red curve) hours of impinging high electron flux on the MCP plates. During the measurements the same voltage per plate U=945 V and the same gap voltage U_g=214 V was applied. Strong decrease of the mean amplitude is observed already after 3 hours of operation and equal to about 60% from initial value.

$3.3{\cdot}10^5$ electrons per seconds. After 3, 4, 5 and 6 hours of bombarding the MCPs with electrons the PHD was acquired and saved. In Figure 3.24 a comparison between the corresponding pulse-height distributions is shown. Already after 3 hours of operation the mean signal amplitude of the MCPs decreases by 60% of its initial value.

By analyzing the decrease of the mean amplitude of the pule-height distribution as a function of the number of electrons impinging on the MCPs one can investigate the percentage of the amplitude reduction during 2 weeks of experiment at the ESR. For instance, every 2 s 5 ions will be ejected in the ESR and they will circulate in the ring with 2 MHz about 1 ms. This means, that every 2 s 10000 ions will hit the MCP detector. If there is now interruption during these two weeks overall about $6 \cdot 10^9$ ions will hit the MCPs. Our studies show that after two weeks the amplitude of the MCP signals will be reduced to about 80% of the original amplitude [Diw 09].

The age effect is irreversible and can only be corrected with higher voltages

applied to the microchannel plates. An example of aging effect compensation with higher voltages per MCP plates can be found in [Diw 09]. Every set of measurements for the specific count rate was done during about 1 hour. So the error between the measured points due to the age effect - amplitude decrease was estimated as 15%.

3.3.2 Measurement of the Rate Capability

To convert the measured count rate to a real count rate, the rate is plotted against the corresponding heating current and fitted with a linear function (Figure 3.25). The difference between the measured rate and the real rate is explained by the fact that at higher count rates compared to the lower count rates the MCP gain drops because of the dead time effect (Sec. 2.5.4.3). During the dead time the MCPs are not responding to newly incoming electrons. That is why one observes the break of linearity between the measured count rate and the heating current applied to the electron source. At the rate of about 10^6 Hz with a further increase of the heating current the count rate does not increase but reaches a plateau (saturation level). From the linear fit the real rate is calculated for every gap voltage U_g, MCPs with 5 μm and 10 μm channel diameter. Figure 3.26 shows the real rate against the measured rate for the measurement using MCPs with 5 μm channel diameter and U_g=214 V. The blue curve fits the experimental data with a theoretical function according to eq. 2.60. One can see that the theory is in a good agreement with an experiment.
One of the important parameters to observe an influence of the high rate on the MCP is the change of the pulse-height distribution (Sec. 2.5.4.3). The pulse-height distribution was measured for every heating current using MCPs with 5 μm and 10 μm pore sizes. In both cases applied voltage per plate was equal to U=953 V and the gap voltage between two plates was varied. During the analysis it was also observed that at the count rate, when the MCP output current linearity violate, the PHD peak shifts to the lower amplitude value. The dependence of real rate from an output current from the MCP bombarded with electrons of certain rate is shown in Figure 3.27.
In Figure 3.28 the development of the pulse-height distribution such as peak shape, the shift of the peak and drastic decrease of it is presented for MCPs with 5 μm pore size and for different rates. The gap voltage in these measurements was set to U_g=214 V. One can see that at the middle region of the count rate (between 10^2 and 10^4 Hz) in our measurements the PHD is peaked and looks almost the same. At the count rate of $3.3{\cdot}10^6$ Hz the

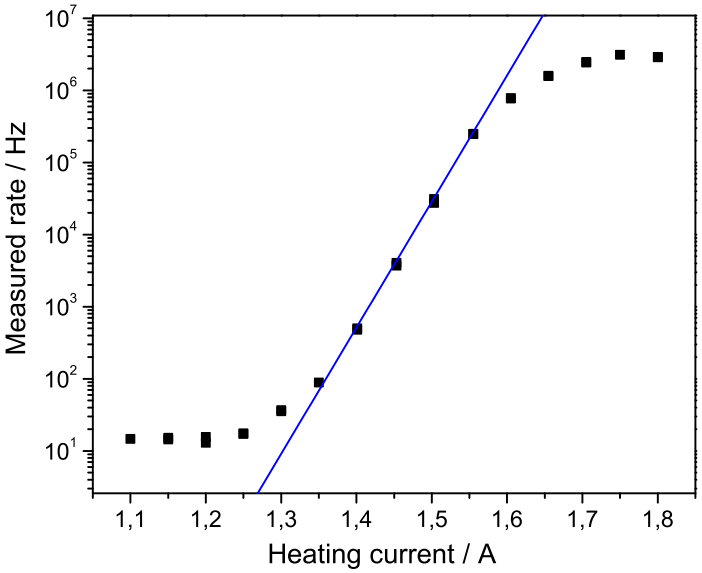

Figure 3.25: The measured count rate using MCPs with 5 μm pore size in dependence on the heating current applied to the electron source shown in logarithmic scale. The gap voltage between two MCPs was set to U_g=214 V. Linear agreement between the measured rate and applied heating current breaks at a point when less gain is supported from the MCPs. It happened because of the dead time effect. The blue line represents the linear fit, which is used to recalculate the real rate.

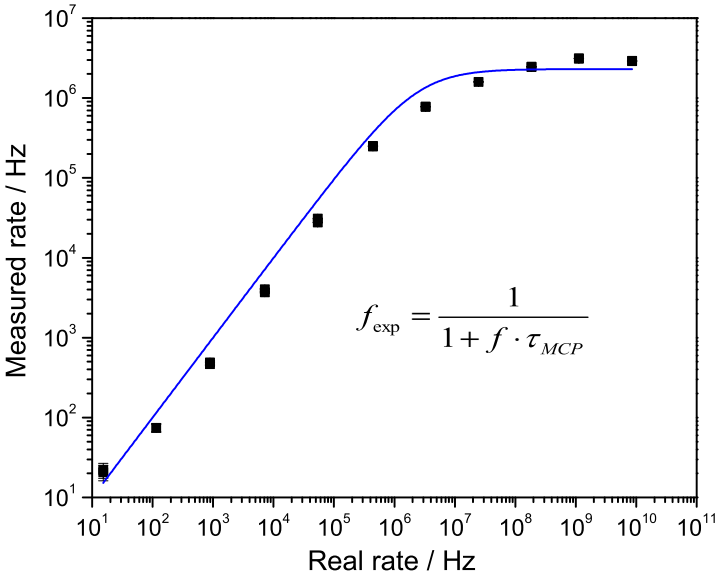

Figure 3.26: Double logarithmic representation of the measured rate against the real rate. The blue line describes the behavior of the real rate data points according to the theoretical model, described with eq. 2.60. The measurement is shown for MCPs with 5 μm pore size and U_g=214 V.

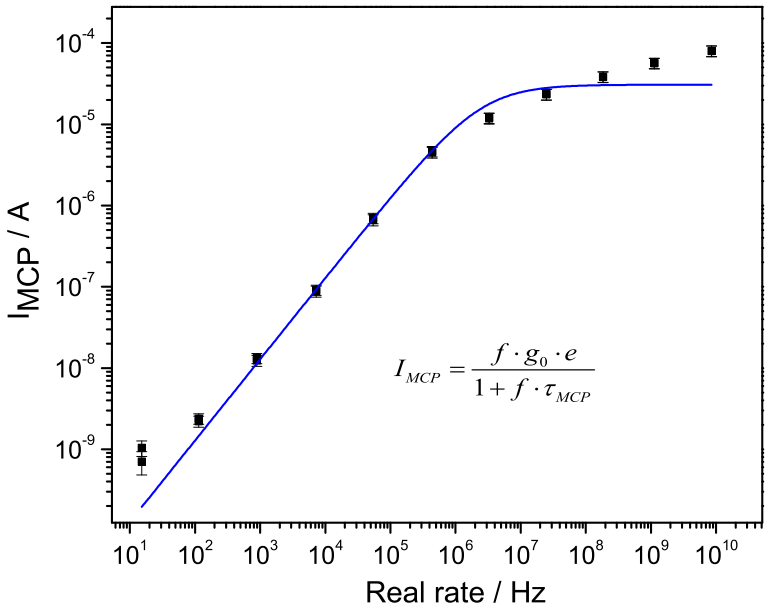

Figure 3.27: Double logarithmic representation of the real rate against the output current from the MCP. The blue line describes the behavior of the outgoing current from the MCP by bombarding with electrons with a certain rate according to eq. 2.59. The measurement is shown for MCPs with 5 μm pore size and U_g= 214 V.

PHD loses its peaked shape and moves to the lower amplitude values. With further increase of the rate the PHD losses completely its peaked shape. The rate at which the PHD changes the shape significantly is taken as a critical rate for these MCPs. An average count rate (from $1.1 \cdot 10^2$ Hz till $3.3 \cdot 10^6$ Hz) detected by the MCPs during these measurements (see Figure 3.28) is about $6.3 \cdot 10^5$ Hz and it is similar to the rate of $3.3 \cdot 10^5$ Hz where the shift of the PHD was observed after 3 hours continuous bombardment of the MCP with electrons (Figure 3.24).
The comparison between the rate limits for MCPs with 5 μm and 10 μm pore size is summarized in Figure 3.29 as a function of different gap voltages U_g. In the measurements with two types of MCP channel diameters was observed that indeed microchannel plates with 5 μm pore size are about 4 times more resistant to higher rates than the plates with commonly used 10 μm channel diameter.
Different gap U_g voltages between the microchannel plates do not change the result significantly. Probably the strip current effect and geometrical effect (finite number of excited channel in the MCP) compensate each other in

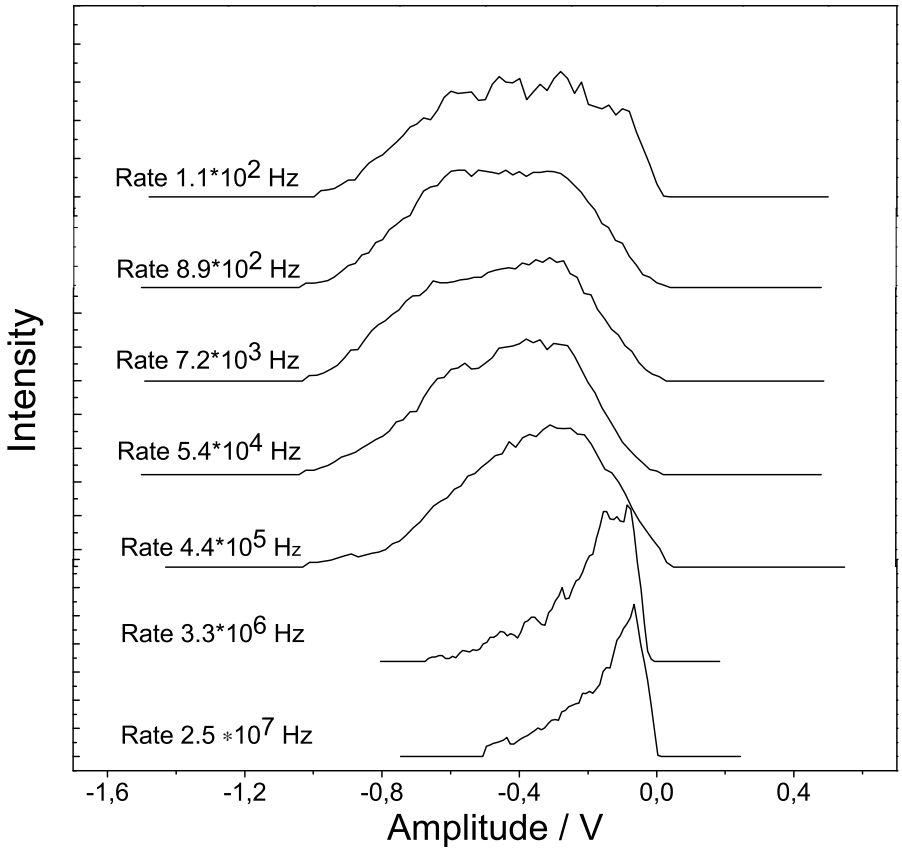

Figure 3.28: Change of the pulse-height distribution for different count rates for MCPs with 5 μm pore size and the interplate voltage of 214 V. At the rate between $1{\cdot}10^2$ - $5.4{\cdot}10^4$ Hz the PHD has a peak shape. From the count rate of $4.4{\cdot}10^5$ Hz the PHD starts to shift to the lower amplitudes and at $2.5{\cdot}10^7$ Hz changes completely to the exponential shape. The last value of the rate is taken as a critical rate for these types of MCPs.

the variation of the potential difference between two microchannel plates.

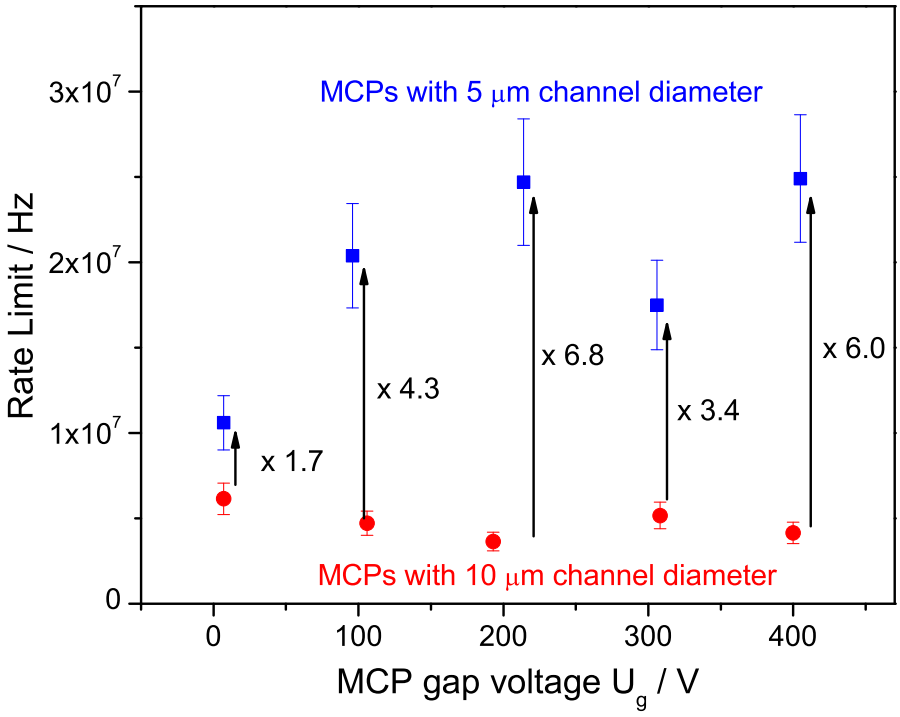

Figure 3.29: Comparison between the critical rate (onset of shift of PHD) of MCPs with 5 μm (blue squares) and 10 μm (red circles) pore sizes at different acceleration voltages U_g between the plates. The error of the measurements is about 15% and estimated as an error from the aging effect. From the results of the measurements follows that MCPs with 5 μm channel diameter have about 4 times higher rate capability than commonly used MCPs with 10 μm pore size. Different applied gap voltages U_g between the microchannel plates do not change the result significantly.

Chapter 4

Online Experiments

More than 100 turns are needed in order to obtain a reliable revolution time of each circulating ion. The revolution frequency of the ESR, f_{ESR}, is about 2 MHz, then the rate of impinging on the TOF detector proportional to

$$f \approx f_{ESR} \cdot N_{ion} \cdot \bar{n}_{se}, \tag{4.1}$$

where N_{ion} is the number of stored ions and $\bar{n}_{se}$ is the number of secondary electrons produced from the foil. For instance, 10 ions of $^{20}Ne^{10+}$ beam in the ring will generate $1.6{\cdot}10^8$ hits/s on the detector. Therefore, it requires a high rate capability detector. As it described in Sec. 2.5.1.2 the secondary electron yield n_{se} is proportional to the electronic energy loss of the projectile. The calculated results for the dependence of average n_{SE} on the charge number Z_p of the projectile in carbon foil with the thickness 10 $\mu g/cm^2$ are presented in Figure 4.1. The projectile energy per mass unit is taken as E_p/M_p=381.913 MeV/u. For the comparison the $\bar{n}_{SE}$ is indicated for the α-particle ($\times$) with 1.145 MeV/u.

Because of the thin carbon foil the energy loss of the ions passing through it will be smaller than in previously used carbon foil of 17 $\mu g/cm^2$ coated with 10 $\mu g/cm^2$ of CsI on both sides and therefore, longer ion revolutions in the ring is expected. With higher number of turns in the ring one will increase the detection efficiency and therefore the mass measurement accuracy. Two experiments have been performed with $^{20}Ne^{10+}$ primary beam and with $^{238}U^{73+}$ fission fragments in the ESR. In these experiments for the first time a thin carbon foil with the thickness of 10 $\mu g/cm^2$ and MCPs with 5 μm pore size were installed in the Time-of-Flight detector.

According to the offline experiments (Sec. 3.3) MCPs with a 5 μm pore size can accept a higher count rate than MCPs with the same active diameter

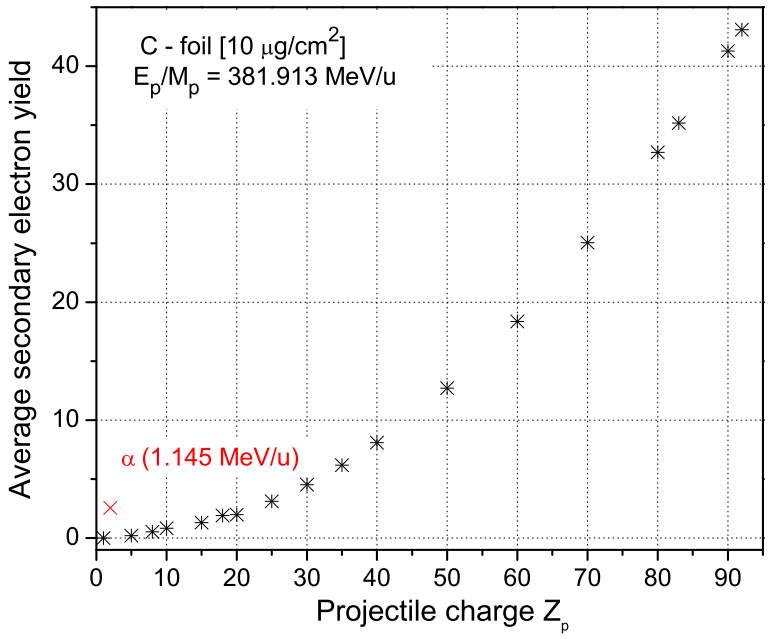

Figure 4.1: Calculated an average secondary electron yield (∗) from the surface of carbon foil with the thickness 10 $\mu g/cm^2$ as a function of the projectile charge number Z_p. The projectile energy per mass unit is E_p/M_p=381.913 MeV/u. For the comparison $\bar{n}_{se}$ is indicated in case of α-particle (×) with 1.145 MeV/u.

but with a commonly used pore size of 10 μm .
Two dedicated experiments will be discussed in following sections.

4.1 Experiment with 322.8 MeV/u $^{20}Ne^{10+}$ Projectiles

In the first experiment a $^{20}Ne^{10+}$ stable beam was used to investigate the rate capability of the MCP detector with smaller pore size microchannel plates.
A second reason was also to investigate online the rate acceptance of the TOF detector with 5 μm pore size MCPs and to compare the results with previously made experiment, where 10 μm pore size MCPs were used [Fab 08].
The experimental facility which was used in the measurements with $^{20}Ne^{10+}$ stable beam is shown in Figure 4.2, the main parameters of the setting are highlighted with blue color. The $^{20}Ne^{10+}$ beam is accelerated up to 11.388

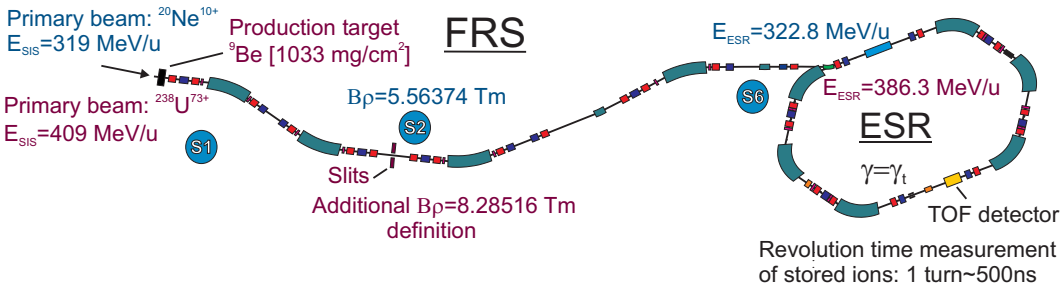

Figure 4.2: Schematic representation of the FRS - ESR facility with indicated main parameters used in the measurements with $^{20}Ne^{10+}$ stable beam and $^{238}U^{73+}$ fission fragments. In the first experiment the FRS is used as a pure magnetic rigidity analyzer with $B\rho$=5.56374 to transmit and to inject the $^{20}Ne^{10+}$ stable beam into the ESR. In the second experiment the exotic nuclei were produced via fission reaction of $^{238}U^{73+}$ primary beam in the ^{9}Be production target of thickness 1033 mg/cm^2. The indicated parameters with blue color belong to the setting of the experiment with stable beam while the parameters with maroon color were set in the measurements with uranium fission fragments.

MeV/u in the UNILAC and injected for further acceleration into the heavy ion synchrotron SIS. In the SIS the ions are accelerated till 319 MeV/u. In this experiment the FRS is used as a pure magnetic rigidity analyzer with $B\rho$=5.56374 Tm to transmit and to inject bare $^{20}Ne^{10+}$ ion beam into the ESR. The ESR is operated in isochronous mode and the revolution time of stored ions are measured with the TOF detector. The energy of the storage ring was set slightly higher than FRS and it is equal to 322.8 MeV/u.
The frequency dependence on the magnetic rigidity or on the cooler voltage is called an isochronicity curve. The measured isochronicity curve obtained using $^{20}Ne^{10+}$ primary beam is shown in the upper part of Figure 4.3. It is obvious that there is a direct relation between the cooler voltage and $B\rho$, as the former determines the energy and consequently also the $B\rho$ of the ions (eq. 2.7). Therefore the isochronicity curve is identical in both representations. The lower part of the Figure 4.3 shows the dependence of the revolution time on the $B\rho$ change. Only for small $B\rho$ region ($\Delta(B\rho)/(B\rho) = 1.5 \cdot 10^{-4}$) as it indicated with blue shaded area in Figure 4.3 the isochronous condition is fulfilled. The isochronicity of the ring was checked and it was isochronous for m/q=2.1.
After an injection into the ESR the oscilloscope saves a spectrum with a length of 400 μs and according to the frequency of the ESR it is about 800 ion revolutions. The digital oscilloscope LeCroy Waverunner 6100A with a bandwidth of 1 GHz was used. The sampling rate of the oscilloscope of 2.5 Gsamples/s was chosen to cover 400 μs record length of the spectra.

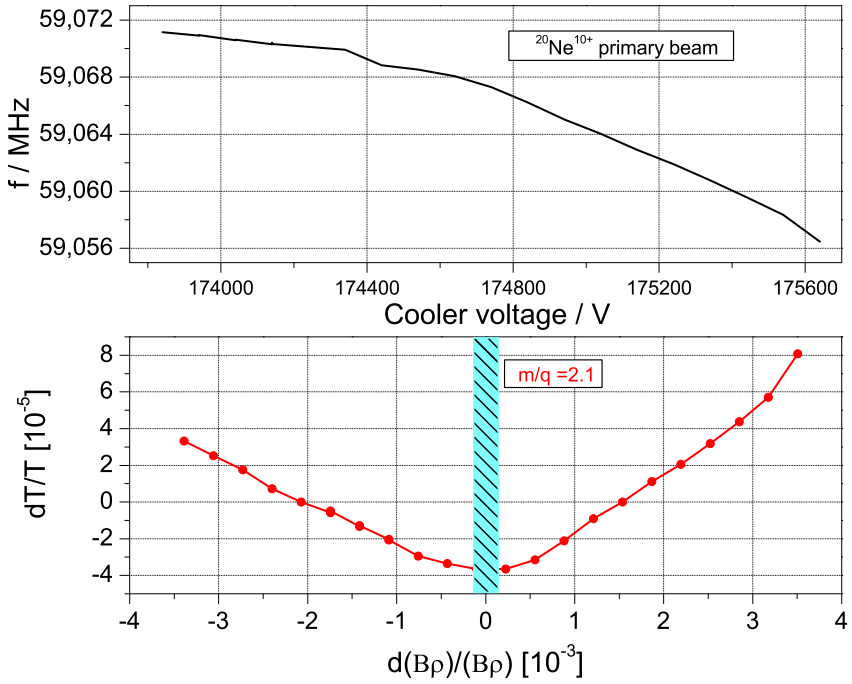

Figure 4.3: The isochronicity curve measured with the $^{20}Ne^{10+}$ primary beam is shown in the upper. The cooler voltage was changed step by step and the corresponding frequencies of the ions determined. With these frequencies the revolution times were calculated and plotted against the corresponding magnetic rigidities on the lower part. It was checked that the ring was isochronous for m/q=2.1.

According to numerous offline measurements the voltages for the MCP detectors U_{Forward} and U_{Backward} were chosen so, that measured corresponding pulse-height distributions have a peaked shape and equal to U_{det}=3115 V that is about 0.990 kV per MCP plate. The voltages U^{++}, U^{-}, U_{Foil} and the magnetic field were set according to the optimized by simulations [Fab 08] setting (Table 3.3).

The main voltages applied to the TOF detector were remotely controlled with a Labview software developed for IMS experiments. So those main voltages could be set during the experiment without entering the experimental hall.

In this online experiment the rate capability of the MCP detector and influence of the reduced energy loss in thin carbon foil as well as a timing performances of the TOF detector were investigated. In these measurements about 58 injections were saved and analyzed.

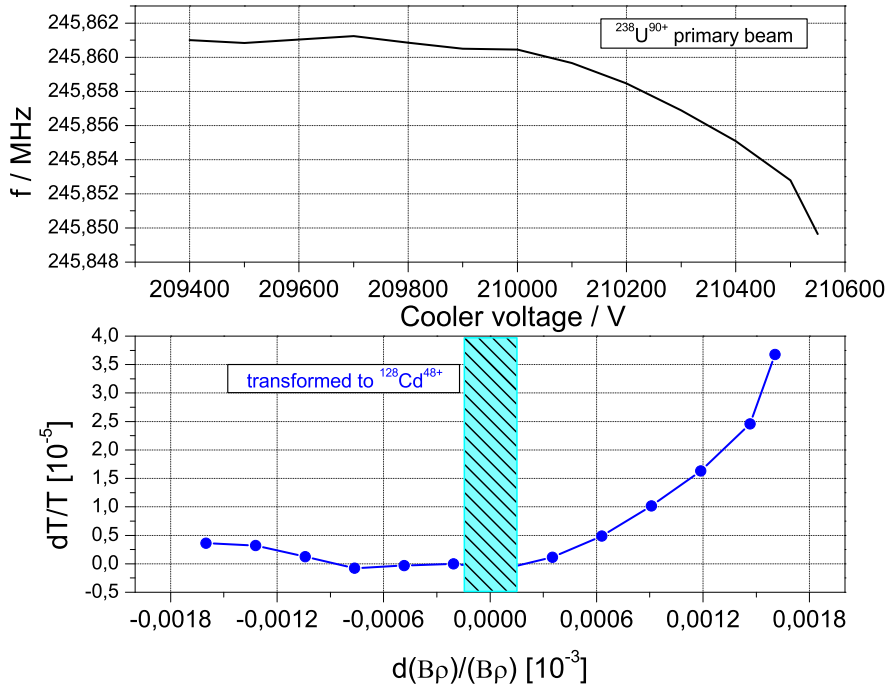

Figure 4.4: The isochronicity curve, cooler voltages versus frequencies (upper part) obtained using $^{238}U^{90+}$ primary beam. On the lower part the transformed isochronicity curve in $B\rho$ versus revolution time is calculated for the reference fragment $^{128}Cd^{48+}$.

4.2 Experiment with Uranium Fission Fragments

In the second experiment the rate capability of the TOF detector was investigated with ^{238}U fission fragments. The primary beam $^{238}U^{73+}$ was accelerated by the heavy-ion synchrotron SIS to the relativistic energy of 409 MeV/u. Then the primary beam impinged on a 1033 mg/cm^2 beryllium target, placed at the entrance of the FRS for fission productions. The experimental setup as well as main parameters of the settings (maroon color) are indicated in Figure 4.2.

By applying the $B\rho$ tagging method [Kno 08] the fission fragments will be transmitted through the FRS. At the middle focal plane S2 the slits were moved inside on a gap of 2 mm, so then only the ions which satisfy the chosen $B\rho$ window of $\Delta B\rho$ / $B\rho \approx 1.5 \cdot 10^{-4}$ (indicated as a blue shaded area) will fly through and transmitted into the ESR. The $B\rho$ setting of 8.23158 Tm for fragments centered to $^{128}Cd^{48+}$ was applied to the FRS - ESR.

As a trigger for the oscilloscope an injection trigger into the ESR was used. The ESR was set to the energy of 386.3 MeV/u.

The primary beam $^{238}U^{73+}$ after passing through the beryllium production target changes its charge state. Therefore the isochronicity curve, cooler voltages versus frequencies (upper part of Figure 4.4) was measured using $^{238}U^{90+}$ beam. The isochronicity curve transformed from the measured curve to the reference nuclei $^{128}Cd^{48+}$ is shown in the lower part of Figure 4.4. It is shown as a function of $B\rho$ and revolution time.
After an injection into the ESR the oscilloscope acquired a spectrum with a length of 800 μs corresponding to about 1600 ion revolutions. The sampling rate of the oscilloscope of 5 Gsamples/s was used.
To confirm the effect of higher number of turns we compared the revolution times of the fission fragments measured with thinner carbon foil and 5 μm pore size MCP with fission fragments from former measurement [Kno 08] [Sun 08a] with a 17 $\mu g/cm^2$ carbon foil coated with CsI of 10 $\mu g/cm^2$ on both sides and MCPs with a channel diameter of 10 μm.

4.3 Data Analysis

The data acquisition for the experiment is shown in the Figure 4.5. Figure 4.6 shows an example of the stored spectrum from the measurements with $^{238}U^{73+}$ fission fragments.
The first step for the data analysis is to extract the event times of each signals recorded by the oscilloscope. Then the determination of the revolution time for every ion has to be done. After determination of the ions revolution times in the ring the identity of the of the ions can be detrmined.

4.3.1 Timing with the Constant Fraction Method

The software *Extract_timestamps* (previous PhD works of [Hau 99] [Kno 08] [Sun 08a]) for the TOF data analysis was extended to determine precision ion arrival time from the online experimental data and from the offline data. With a help of the software it is possible to analyze the whole spectra from the the online experimental data as well as single signals from the offline experiments. The software modified to accept data acquired with different oscilloscopes with different sampling rates. Two main event time determination methods are included in to the software: Constant Fraction Discrimination (CFD) method and extrapolation to zero [Kno 08] [Sun 08a]. In this work the CFD method was used.
An arrival time of the signal - event time is of a high interest in the ion revolution time measurements. The main uncertainties of the event time determination are summarized in Figure 3.13.

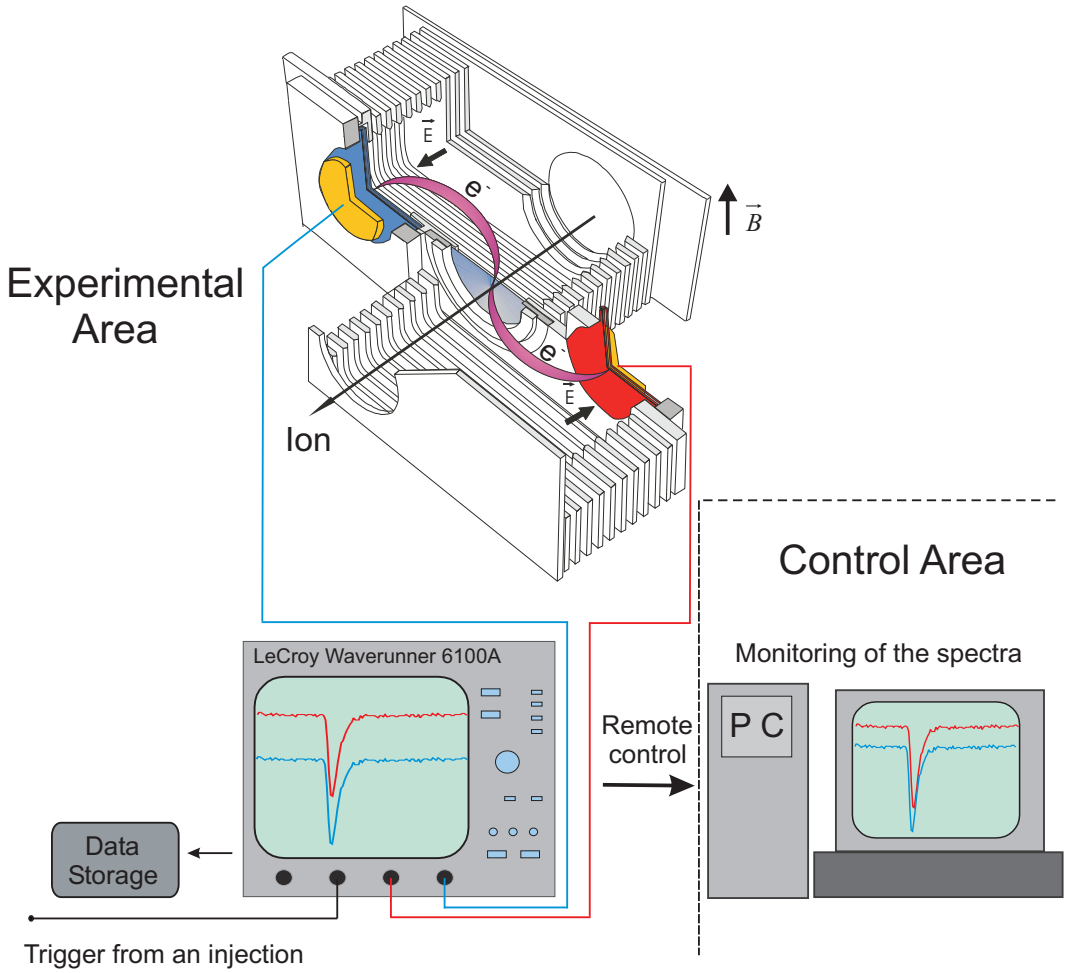

Figure 4.5: Data acquisition system used in the online experiment. In the experimental area the signal from the anode connected with a cable to the oscilloscope that digitized the signal spectra and saved on the external harddrive. The voltages for TOF detector as well as the scope setting can be set and viewed directly in the control area remotely. As a trigger for the oscilloscope an injection trigger into the ESR is used.

In the TOF detector an electron charge produced from the MCPs is collected on the anode and can vary drastically. It means that the amplitude varies significantly from signal to signal also the rise time can vary somewhat. In Figure 4.7 two signals with different amplitudes are shown from the online experiment. To minimize walk effects the experimental data have to be treated with an appropriate timing method. The CFD method is one of the most efficient and flexible method of the event time determination. In this method, the logic signal is generated at a constant fraction f of the peak height to produce essential walk-free timing signal [Leo 87]. The technique by which the CFD method is achieved is shown in the Figure 4.8. To determine the baseline the amplitudes of all signals are histogrammed to get the noise distribution [Mat 04]. The Constant Fraction Discriminating

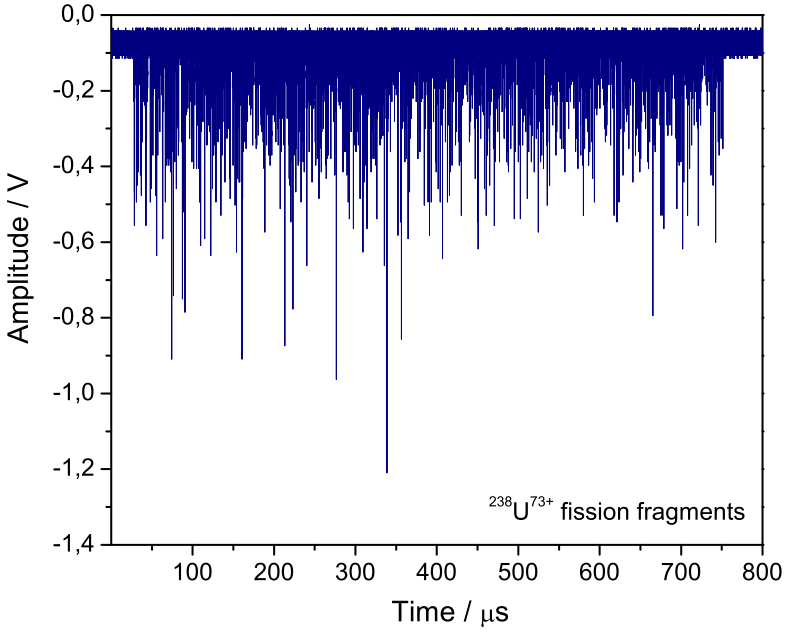

Figure 4.6: Online spectrum of stored ions with LeCroy oscilloscope in the experiment with ^{238}U fission fragments. An oscilloscope was set to store the spectrum with record length of 800 μm what corresponds to about 1600 revolution turns in the ESR.

method depends on two main parameters: the fraction factor f and the delay b. The original signal is split into two components. At first one of the component is attenuated with a certain fraction f and shifted by time b in such way that $0 \ll b \leq t_{rise}$ (blue curve), the other component is inverted (green curve). These two components are summed (red curve) and the zero crossing with a baseline defines the event time (Figure 4.8).
In the analysis of the online data with the CFD method in this work the following parameters were used: f=0.5, b=3. An optimal selection of those parameters is a guarantee for a good timing determination. A more detailed explanation of significance and right choice of the CFD parameters one can find in [Mat 04].
The timing precision of the TOF detector was determined by measuring the jitter in time difference between two coincidence signals from forward and backward MCP detectors. Time-stamps recorded from both MCP detectors, corresponding to the same time event were subtracted from each other and plotted as a histogram. The coincidence time-of-flight distribution in the case of $^{20}Ne^{10+}$ beam (upper part) and ^{238}U fission fragments (lower part) is shown in the Figure 4.9 and Figure 4.10.

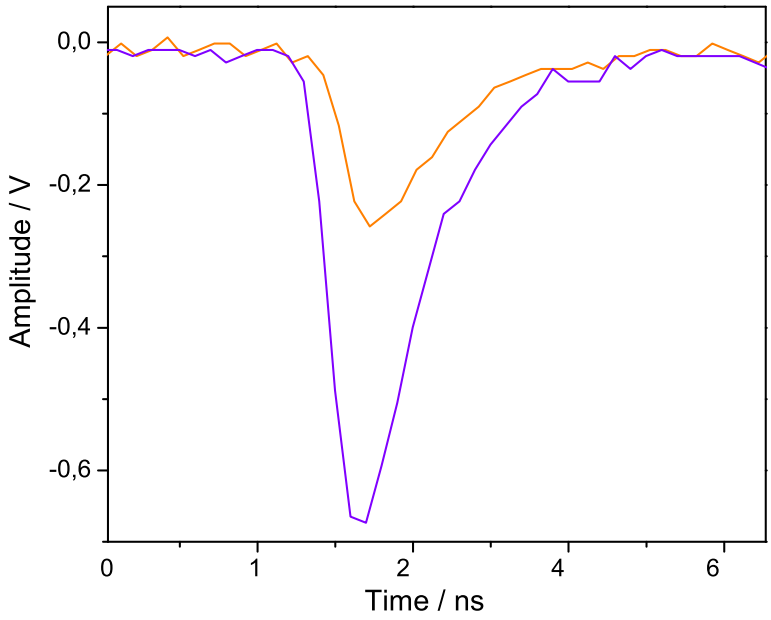

Figure 4.7: Comparison of two signals from one particle with different amplitudes. The signal indicated with violet color needs a longer time to reach its maximum than the one with orange color. This effect, which will cause the time jitter in the event time termination, is called amplitude walk and can be minimized by the Constant Fraction Discriminating method.

From the coincidence time-of-flight distribution for the data with $^{20}Ne^{10+}$ beam one can see an additional artifact on the right tail of the distribution indicated with blue color. The signals corresponding to those coincidences were investigated more detailed. It was observed that those signals belong to the truncated signals. Truncated signals are the signals with the amplitudes larger than the maximum voltage range of the oscilloscope display setting. In those cases the correct signal maximum and so the correct CFD technique can not be applied. Therefore this artifact was not taken into analysis and the distribution indicated with grey color was fitted with a Gaussian function (red curve). A standard deviation of $\sigma(\mathrm{Ne})_{\mathrm{branch}}$=48 ps is calculated. For the experiment with uranium fission fragments (Figure 4.10) the sigma of coincidence time-of-flight distribution is obtained as $\sigma(\mathrm{fiss.frag.})_{\mathrm{branch}}$=45 ps. For both experiments the same number of coincidences were taken; 1272 coincidences were analyzed. These standard deviations obtained from both online experiments are in a good agreement with the results from the offline experiments.

An uncertainty distribution of each event time determination using the CFD

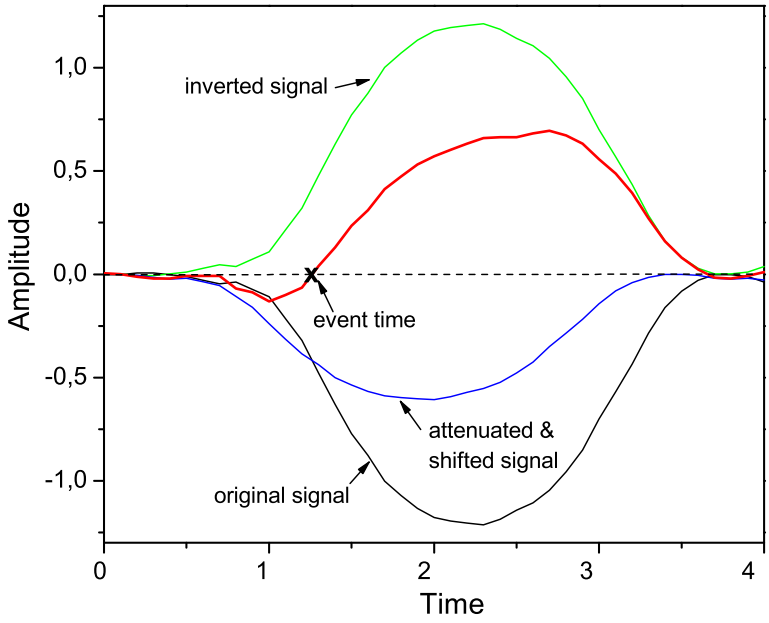

Figure 4.8: The principle of the constant fraction discriminating technique. One component of the signal is attenuated with a certain fraction f and shifted by time b (blue curve), the other component is inverted (green curve). Finally both components are summed (red curve) and the timing is determined as a zero crossing with baseline.

method is shown in Figure 4.11. The error calculation for the data treated with the CFD method implemented in the software is explained in [Mat 04]. In case of the measurement with $^{20}Ne^{10+}$ stable beam (upper part) the uncertainty in the event time determination is equal to about 8 ps. In the experiment with uranium fission fragments it is equal to 11.5 ps. In the calculation of the event time uncertainty the error of the signal amplitudes is assumed to be equal to the standard deviation $\sigma(U_0)$ of the distribution obtained for the baseline determination [Mat 04]. From the Figure 4.11 one notice that the uncertainties for the event times determination for forward detector are larger than for the backward detector in both experiments. This is explained by the voltage settings of the channel of the oscilloscope. In both experiments 200 mV/div was set in the channel where the spectra from the forward detector were acquired and 50 mV/div for the backward channel. Therefore the noise level of the spectrum and thus the $\sigma(U_0)$ in case of the forward detector is larger.

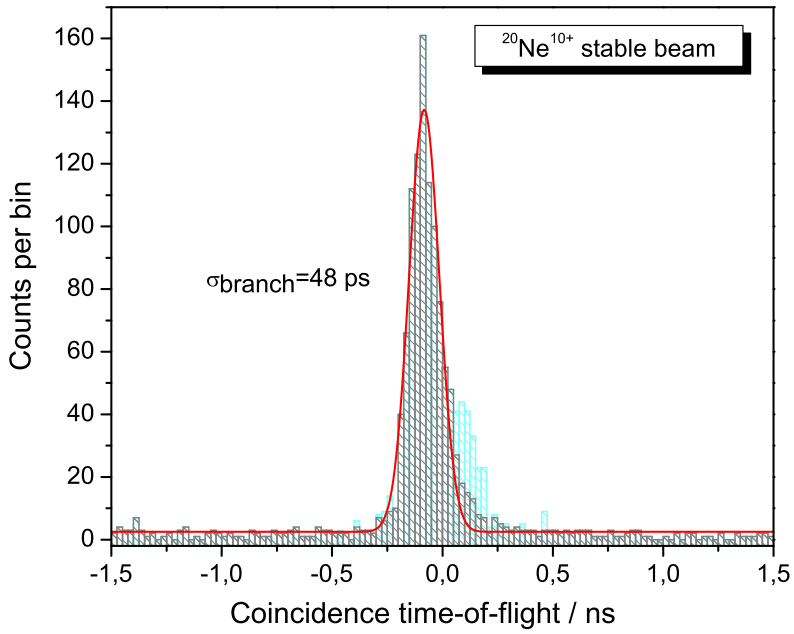

Figure 4.9: Coincidence time-of-flight determination for the data obtained with $^{20}Ne^{10+}$ stable beam. The spectra are stored for both detectors and the event times are calculated with the CFD software method. Then the event times corresponding to the same event subtracted between each other and plotted as a histogram. The standard deviation is calculated with the Gaussian fit function (red curve). An additional artifact on the right part of the distribution indicated with blue color corresponds to the coincidences which belong to the truncated signals. Those signals were not taken into analysis and the sigma σ_{branch}=48 ps is calculated from the distribution shown with grey color.

4.3.2 Revolution Time Determination

After determination of the event times the revolution times of individual ions have to be determined. In the further analysis a list of event times is analyzed with the *mtrace* program that was developed in earlier PhD works [Hau 99] [Sun 08a]. To determine the revolution time of each ion first all event times have to be assigned to the corresponding ions. The *mtrace* software includes a pattern recognition algorithm that seeks for a series of equidistant intervals [Hau 99] [Sun 09]. Here helps the periodicity of the event times as a result of the ions circulating in the ring.

The revolution period of the ESR is about 500 ns which corresponds to a revolution frequency of about 2 MHz. The program searches for the event times which are equidistantly distributed in the spectrum within the time

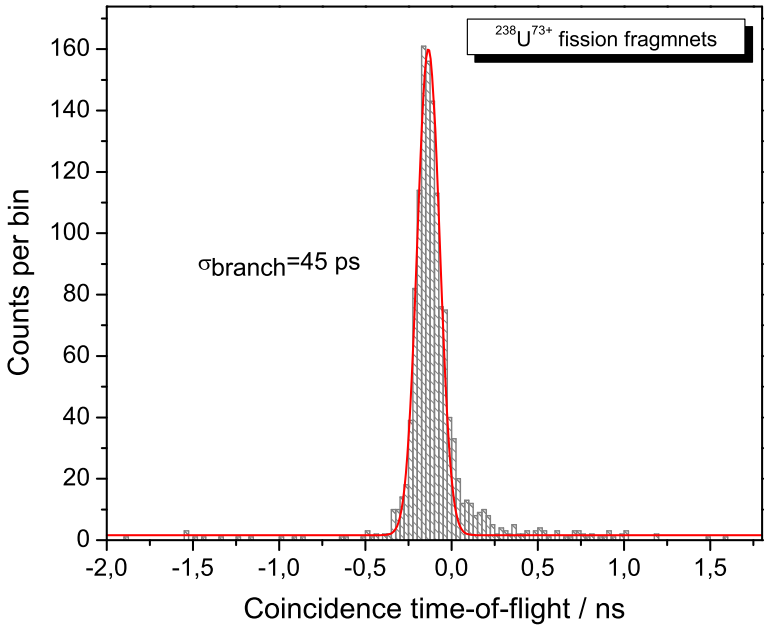

Figure 4.10: Coincidence time-of-flight distribution of the event times determined in the measurements with ^{238}U fission fragments. The standard deviation is equal to σ_{branch}=45 ps.

window of 440-550 ns. It is assumed that between two event times which are belong to one ion only an integer number of turns can be found. However one has to take into account that some ions make only several revolutions in the ring and get lost quickly. It happens due to the energy loss of the ions passing through the foil at every turn and also because those ions are injected into the ESR with bad isochronicity.

To avoid the determination of the revolution times of the ions, which are already lost after several turns the program starts a tracing algorithm from a very last signal in a spectrum and searches for a corresponding one from previous signals. There are several parameters, which have to be set in the *mtrace* program for each experiment. If the suitable signals are found within the window between "l"=440 and "u"=550 ns, the revolution time is fixed. Then the rest of the spectrum is scanned with the expected trace of the found revolution time. It is often the case that for a certain found revolution time several event times can suit with a distant between each other of tens of picoseconds. In such case the ion with most appropriate event times will be assigned to this revolution time and the procedure of searching is repeated till all ions are traced. There are also revolution times

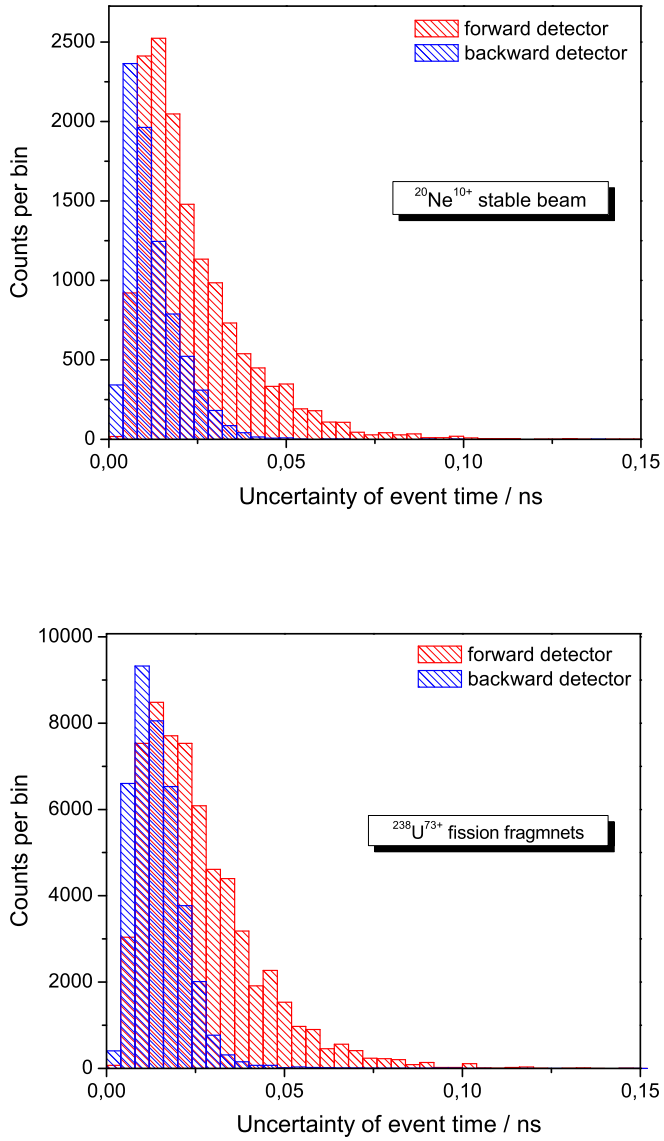

Figure 4.11: Distribution of the uncertainties of event times determination with CFD method implemented into *Extract_Timestamps* software. On the upper part the uncertainty distribution for forward (red bins) and backward (blue bins) detectors is shown for the measurements with $^{20}Ne^{10+}$ beam and σ(E.T.D) is estimated as 8 ps. In the lower part the uncertainty distribution is shown for the data with ^{238}U fission fragments in the same colors and is estimated as 11.5 ps. The difference in uncertainties of event time determination between forward and backward detectors is explained in the text.

found with less amount of appropriate event times. If no other event times are found, the calculated revolution time was not correct and the procedure is repeated again until an appropriate revolution time is found [Mat 04].
In general the time-of-flight is determined as a difference between two signals at the beginning and at the end of the measuring time. Since there are revolution times in the ring with less than 50% detection efficiency, it can happen that one event time can be a stop for one revolution time of an ion and conversely just the beginning for another ion. The minimum efficiency "f" is required for particles to be considered valid. In a chain of event times which belong to one revolution time can be a break of about "t"=25 turns. During this time the ion is not detected, but after it the ion appears in the trace again and the program adds this ion to the previously found event time chain. This new added chain should consist in minimum of 7 event times.
Each event time has an uncertainty as it was discussed in previous subsection. To determine the ion revolution time more precisely one has to investigate a time dependence on a turn number (left upper part of the Figure 4.12). The dependence is shown for a single ion. To investigate the deviation between the event times and corresponding turn number the data is fitted with a linear function

$$T = A + B \cdot n_T, \tag{4.2}$$

where n_T is the turn number. The corresponding coefficients are taken to recalculate the event times and the residuals are plotted against the turn number. Figure 4.12 shows the residuals for the 1^{rst} (right upper), 2^{nd} (left lower) and 3^{rd} (right lower) orders of polynomial functions. Further increase of the parameters would not give an improvement, therefore the 3^{rd} order polynomial was used

$$T = A + B \cdot n_T + C \cdot n_T^2 + D \cdot n_T^3 \tag{4.3}$$

and the error for recalculated event times is taken as

$$\begin{aligned} \Delta T &= \sqrt{\Delta A^2 + (n_T \cdot \Delta B)^2 + (n_T^2 \cdot \Delta C)^2 + (n_T^3 \cdot \Delta D)^2} + \\ &+ \sqrt{((B + 2C \cdot n_T + 3D \cdot n_T^2) \cdot \Delta n_T)^2}, \end{aligned} \tag{4.4}$$

where Δn_T is the error of the turn number determination. As the revolution time used for the further analysis is determined from the slope of the fitted function the Δn_T is negligible and not considered in the error calculation. The fitting procedure is based on finding a minimum chi-square χ^2 for every parameter. If an ion satisfies the isochronous conditions, the parameters will

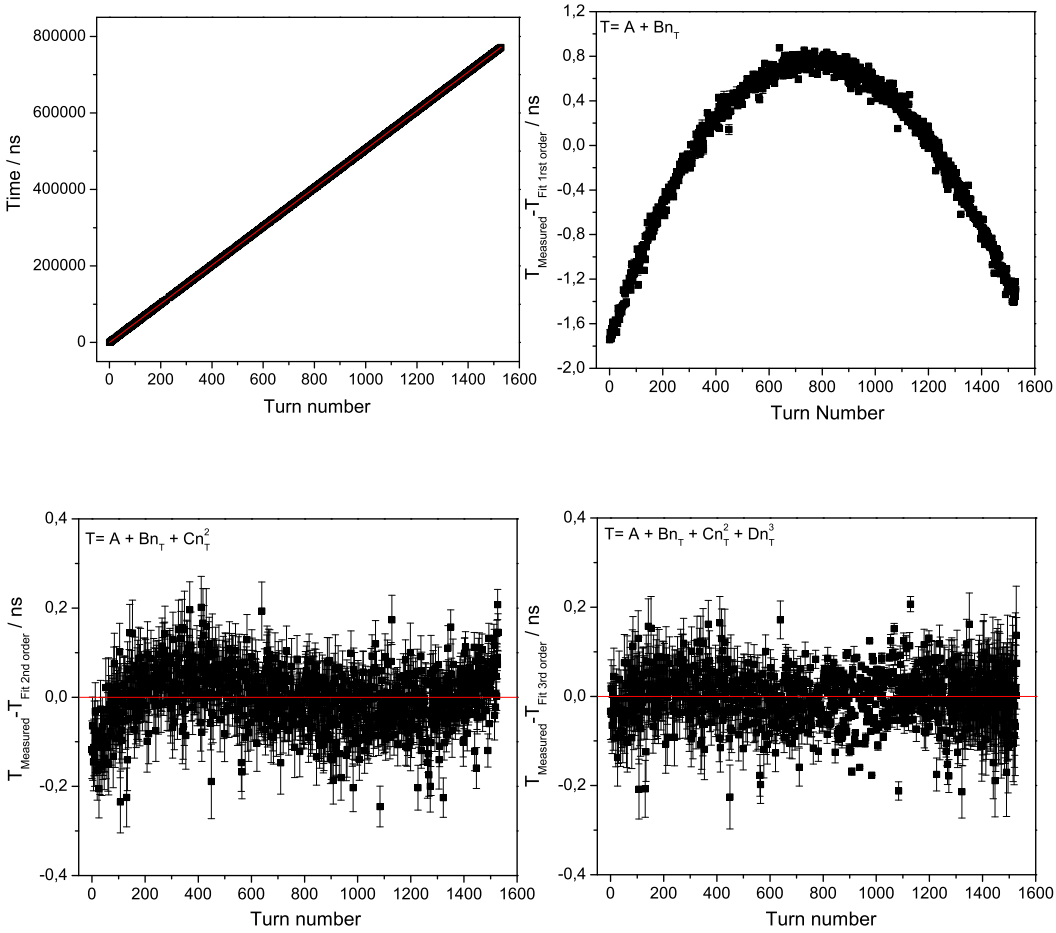

Figure 4.12: The dependence of event times for a single ion on the turn number determined by *mtrace* program. The data is fitted with first order polynomial function and the residuals are plotted on the upper right part. The residuals for the second order polynomial is shown on the lower left part. The revolution time is determined using the fit with 3^{rd} order polynomial (lower right part).

be close to zero and a relationship between time and the number of turns would be a linear function. From the polynomial fit the revolution time is determined, which corresponds to the slope of the polynomial fit. The revolution times for all ions are extracted from the 50^{th} turn number. This number is chosen as a good compromise between an ion optical stability and the energy loss of the ion in the foil [Kno 08] [Sun 08b].

4.3.3 Particle Identification

The next step is to histogram the revolution times of each ion calculated from the previous step according to their occurrence in a spectrum and thus

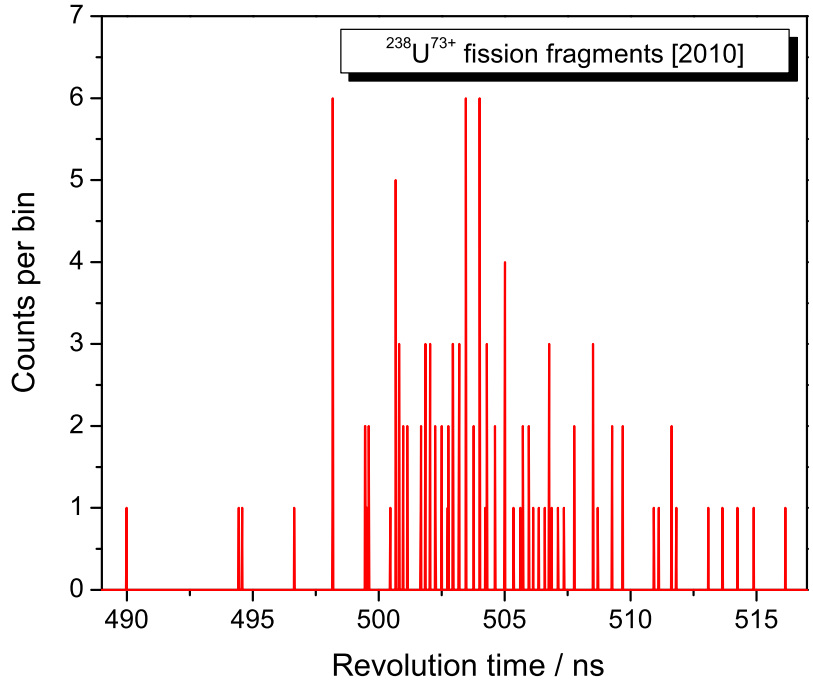

Figure 4.13: Time-of-Flight spectrum produced from the histogram of all determined revolution times in 2010 experiment with ^{238}U fission fragments. The TOF spectrum contains 119 particles from 324 injections.

to obtain a time-of-flight spectrum. In Figure 4.13 such a TOF spectrum is presented. According to the definition of the isochronicity (Sec. 2.2) all nuclei of the same species are supposed to have the same revolution time, therefore every peak consist of particles of the same species. Once all particles are found and their revolution times are determined, the identity of the ions can be determined.
In reality the isochronicity of the ring is not perfect and the revolution time varies slightly around a central revolution time value. To perform an identification some additional complex approach is required. Some restrictions can be applied to the m/q list based on the experimental conditions as below:

1. *Irregularities in m/q values.* This could be seen from the plot of possible mass-to-charge ratios of nuclei from the chart of nuclei. The Figure 4.14 shows the distribution of known m/q in the range of 2.4-2.7 u/e [Aud 03]. One can notice that there is a gap in the region of $m/q \approx 2.5$. Since this range of m/q is also measured in this experiment (Sec. 4.2), one expects to observe the same gap in the TOF spectrum.

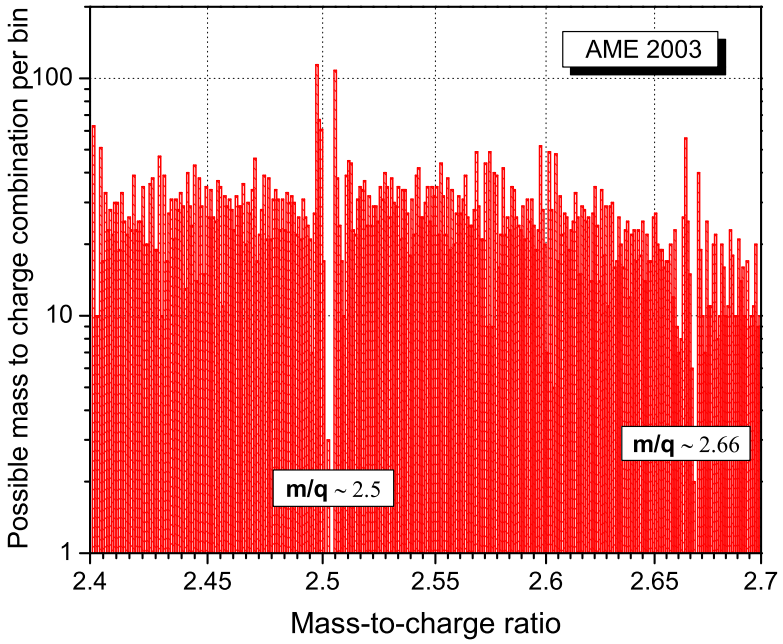

Figure 4.14: Distribution of mass-to-charge ratio in the range of 2.4-2.7 u/e. The data are taken from AME 2003 [Aud 03]. Because of the ion-optical setting of the ESR the measured m/q spectrum lies in the same range. So the irregularities in m/q spectrum can help to identify the ions.

2. *Ion-optical setting of the FRS.* The production and separation of the fragments in the FRS can be simulated with the help of the Monte-Carlo code *MOCADI* [Iwa 97]. *MOCADI* implements the production cross-sections, the reaction kinematics, atomic interactions with matter and ion optical properties of the FRS. One can learn about the expected abundances of the interested nuclei. By finding the most abundant peak in the experimental spectrum, one can find the same in the simulated spectrum and this gives an additional information about mass-to-charge ratio to which this peak belongs. In this experiment the FRS has been centered to transmit $^{128}Cd^{48+}$ produced by $^{238}U^{73+}$ fission. Mainly the fragments of uranium fission in the rage of proton number Z=31-55 are transmitted.

3. *Ion-optical setting of the ESR.* The isochronicity curve, cooler voltages versus frequencies is measured before every IMS experiment with the primary beam. In this work in case of experiment with uranium fission fragments the isochronicity curve was measured with a $^{238}U^{90+}$ primary beam (Figure 4.4). Before the measurements the magnetic

rigidity of the ESR is set to the reference fragment, in our case it is $^{128}Cd^{48+}$. The cooler voltage is related to the magnetic rigidity, as it determines the energy and consequently the $B\rho$ of the ions. Since m/q and velocities are known the magnetic rigidity acceptance of the ESR can be determined. Therefore the measured m/q values are expected in the range from 2.4-2.8 u/e.

4. *Systematization in Z and A change.* Another support in the identification of the peaks, even in case of weak intensity can be found. For instance, within the recorded data, the expected Z-2, A-5 or Z+2, A+5 systematic helps to continue m/q identification in the whole spectrum [Kno 08].

The relation between the revolution times and mass-to-charge ratio for the ions is given by eq. 2.10. Similar to the Schottky mass measurement method in an isochronous mass measurement nuclei with unknown as well as known masses can be stored and measured simultaneously.

4.4 Results of Online Experiments

In this section the results obtained from the online experiments are presented.
The rate capability of the microchannel plates with 5 μm channel diameter was investigated online with $^{20}Ne^{10+}$ stable beam using thin carbon foil with a thickness of 10 $\mu g/cm^2$ in the time-of-flight detector. The results were compared with the data from previous experiment where $^{64}Ni^{26+}$ stable beam was used, as well as MCPs with 10 μm pore size and thicker carbon foil [17 $\mu g/cm^2$] coated with 10 $\mu g/cm^2$ of CsI on the both sides (CsI:C:CsI).
The second experiment was performed with uranium fission fragments to observe higher number of turns of circulating ions in the ring using MCPs with 5 μm pore size and a thin carbon foil. The results of the experiment were compared to previous experiment results [Sun 08a] [Kno 08] where ions with the same mass-to-charge ratio region were measured but using MCPs with 10 μm pore size and a thicker carbon foil coated with CsI.

4.4.1 $^{20}Ne^{10+}$ - Projectiles

To investigate the impacts of a thinner foil and MCPs with smaller channel diameter (Sec. 3.3), the change in the number of detected ions per turn was investigated for present experimental data and compared to the results of

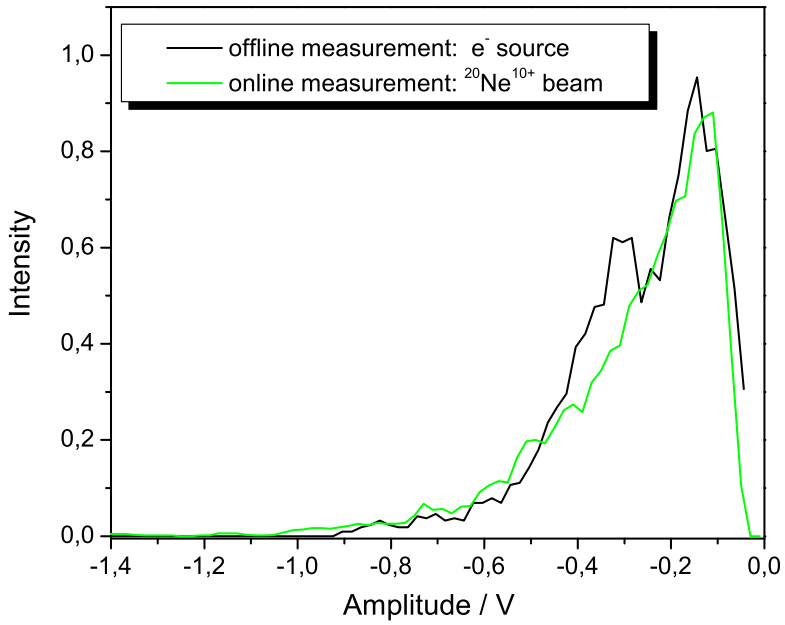

Figure 4.15: Comparison between measured pulse-height distributions from the offline and online experiments. In the offline experiments the MCPs were bombarded with electron beam. In case of the online measurements the MCPs detected the $^{20}Ne^{10+}$ ion beam. The rate in both experiments is similar $5 \cdot 10^6$ Hz and $6.54 \cdot 10^6$ Hz, respectively.

a previous experiment [Fab 08].

Figure 4.15 shows comparison between pulse-height distributions from MCP detector bombarded with electron beam in the offline (black curve) and with $^{20}Ne^{10+}$ beam (green curve) in the online experiments. One can see that at similar rate, the shape of the PHD is similar.

The number of event times (Sec. 4.3.1) is histogrammed and with an average revolution time (Sec. 4.3.2) the corresponding turn number was calculated. To compare an experimental data with simulation a Monte-Carlo code *MOCADI* (Sec. 2.4) used to estimate the number of surviving ions per turn in the ring. The simulations include the ion optics, apertures in the ESR and the energy loss of the ion in the foil.

To explain the behavior of the experimental results the simulations that contain an ion optics of the ring and energy loss in the foil is not sufficient. Because of the finite recharging time of an MCP channel one observes a saturation effect at higher rates, as it is described in Sec. 2.5.4.3 and Sec. 3.3. To compare the experimental data the *MOCADI* simulations are combined with a model which includes the dead time effect [Fab 08]. This model de-

scribes a loss of detection efficiency at high rates, which also depends on the energy loss in the foil and on the number of emitted SE (eq. 4.6).
In Figure 4.16 the average number of ions found per turn for experimental data with $^{20}Ne^{10+}$ stable beam using 5 μm pore size MCPs in the TOF detector and thin carbon foil [10 $\mu g/cm^2$] are shown with green squares. The black line shows the number of ions $N_{\text{ion-optics}}$ according to *MOCADI* simulations. The simulated curve is scaled at turn number 10 to the calculated ion number N_{ion}=3.7 in the ring using the program *mtrace* (Sec. 4.3.2). The red circle-line represents the expected number of the detected ions N_{Detected} that combines the simulation and the model for the dead time effect of the MCPs and can be written as

$$N_{Detected}(t) = N_{ion-optics} \cdot \varepsilon_{Detection}(t), \tag{4.5}$$

where $\varepsilon_{\text{Detection}}$ is the detection efficiency and equals

$$\varepsilon_{Detection}(\varepsilon_{MCP}(t), \bar{n}_{SE}) = 1 - e^{-\varepsilon_{MCP}(t, f_{ESR}) \cdot \bar{n}_{SE}} \tag{4.6}$$

Here ε_{MCP} is the detection efficiency of the microchannel plate and $\bar{n}_{SE}$ is the average number of secondary electrons emitted from the foil. The number of SE does not change with the turn number, but the detection efficiency of the MCP drops from 60% to about 10% at a rate of about 100 MHz. From the offline data [Fab 08] the MCP detection efficiency at this rate is approximately given by

$$\varepsilon_{MCP}(t, f_{ESR}) = 0.5e^{-t/\tau} + 0.1, \tag{4.7}$$

where τ is time constant for saturation effect which has to be determined experimentally. The transmission probability is assumed to be 100%.
The experimental data include all information about detection efficiency drop according to eq. 4.5. To separate those effects and to examine only drop of the detection efficiency due to the MCP dead time effect the ratio of smoothed experimental data (blue solid curve) and the result of *MOCADI* simulation (black solid curve) is calculated. This ratio $\frac{N_{\text{detected}}(t)}{N_{\text{ion-optics}}}$ is plotted with a pink dashed curve and fitted with the function from eq. 4.6. The time constant $\tau_{\text{efficiency}}(5\mu m)$ was determined from this fit and is equal to 463 turns. The blue dashed line indicates the calculated detection efficiency according to eq. 4.6 with determined time constant. It is clearly seen that theoretical calculation is confirmed by the experiment, as the detection efficiency curve deduced from the experimental data (dashed pink curve) is coincide very well with calculated one (dashed blue curve).
Comparison between experimental data obtained using MCPs with 5 μm

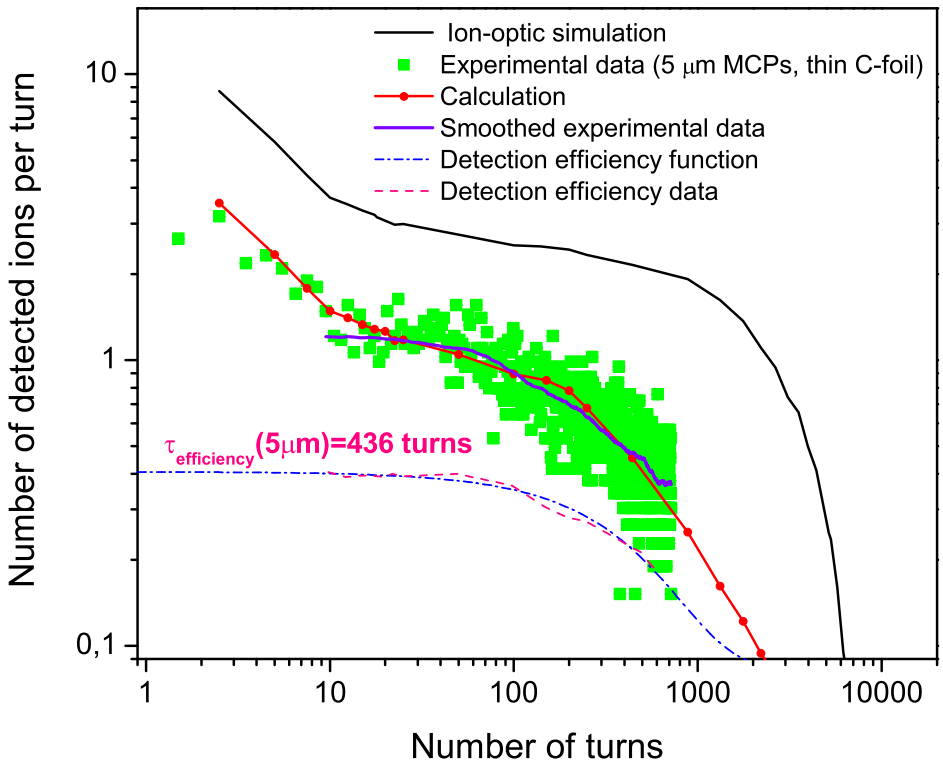

Figure 4.16: Change in the average number of detected ions in the ring per turn. The experimental data for the $^{20}Ne^{10+}$ beam with 5μm pore size MCPs and thin carbon foil [10 $\mu g/cm^2$] is shown with green squares. The record length of the acquired spectrum was set to 400 μs what corresponds to about 800 turns in the ESR. The simulated curve (solid black curve) is scaled to the calculated number of ion N_{ion}=3.7 at turn number 10. The experimental data were smoothed over 100 points and shown with a blue solid line. The pink curve indicates the ratio of experimental data and *MOCADI* simulations. The time constant $\tau_{\text{efficiency}}(5\mu m)$ is determined from the fit of this ratio with detection efficiency function and is equal to 463 turns. The blue dash-dotted curve shows the time development of the MCP detection efficiency function (eq. 4.6). The red line-circle curve represents the calculation that includes ion-optic *MOCADI* simulation and model for the dead time effect eq. 4.5.

pore size and thin carbon foil and the data from a previous experiment is shown in the Figure 4.17. The present experimental data indicated with green squares are compared to the experiment with $^{64}Ni^{26+}$ stable beam, in which 10 μm pore size MCPs and thicker CsI:C:CsI [10:17:10 $\mu g/cm^2$] foil were used (shown with black squares). To be comparable both experimental data are normalized to 14 ions at turn number 10, this number of

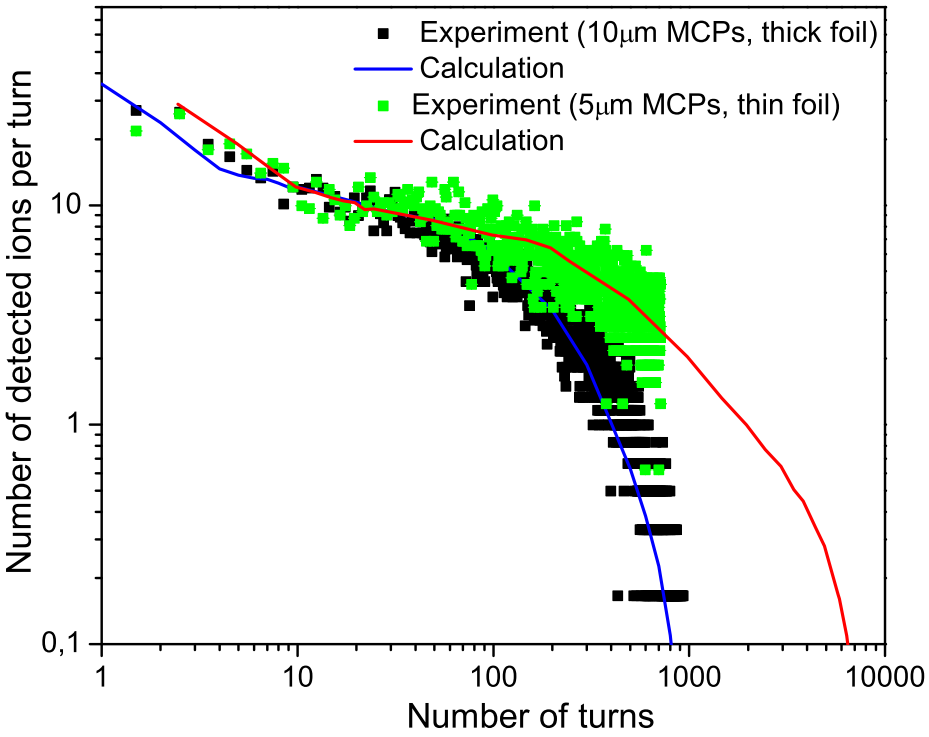

Figure 4.17: Development of the average number of detected ions in the ring per turn for two sets of experimental data. The present experimental data obtained using MCPs with 5 μm pore size and thin carbon foil [10 $\mu g/cm^2$] (green squares) are compared to the experimental data with $^{64}Ni^{26+}$ stable beam where MCPs with 10 μm pore size and CsI:C:CsI [10:17:10 $\mu g/cm^2$] foil were used. The red and blue curves represent the calculations that include ion-optics *MOCADI* simulation and dead time model (eq. 4.5) for both cases. The data and the calculations are scaled to 14 ions at turn number 10.

ions was measured in the previous experiment [Fab 08]. The analysis of both experimental data confirms that the calculated function with an exponential decrease of detection efficiency (red and blue curves) describes the data within a reasonable agreement. According to calculated decay constants $\tau_{\text{efficiency}}(5\mu m)$=463 turns and recalculated for previous experiment $\tau_{efficiency}(10\mu m)$=120 turns.

Achieved results prove the predictions from offline measurements and calculations that less energy loss in thinner carbon foil and about 4 times higher rate resistant MCPs with 5 μm pore size significantly improve an ion survival in the ring. By having more ion revolutions in the ring one increases the detection efficiency and therefore an accuracy of the mass measurement.

4.4.2 Uranium Fission Fragments

The saturation effect in microchannel plates and influence of thinner carbon foil were also investigated in the experiment with ^{238}U fission fragments. The data from a the present experiment were compared to the data from the previous IMS experiment 2006 [Sun 08a] [Kno 08], which was done using MCPs with 10 μm pore size in the TOF detector and a thicker carbon foil coated with CsI on both sides. In the 2006 experiment the FRS-ESR settings were set for the centering fragments $^{133}Sn^{50+}$. The data from uranium fission fragments from both experiments were analyzed in similar way as the data from the $^{20}Ne^{10+}$ stable beam.

To make a comparison between two experiments with uranium fission fragments the development of an average number of detected ions over the turns was investigated for the same mass-to-charge ratio range for both experimental data set. Table 4.1 summarizes the ions which were identified in this experiment with ^{238}U fission fragments. Unfortunately according to the lack of statistics (measurement time $\sim$ 7 h), a determination of the mass values could not be performed. In the 4th and 5th columns the mass values (ME) and corresponding errors (ΔM) are given from the reference sources which are shown in the last column. In case of ^{114}Rh it is not clear whether the measured mass value applies to the ground or to the excited isomeric state [Hag 07a]. The nuclides ^{88}As, ^{94}Br, ^{122}Ag and ^{164}Gd with unknown masses were identified in this work and indicated with bold and red color. For ^{122}Ag the ground state can be affected by an relatively long-lived isomeric state with a half-live of 1.5 s according to [Aud 03].

As the m/q values directly proportional to the revolution times (eq. 2.10) it is sufficient to compare revolution time spectra from both experiments to be sure that the same m/q range is used for the analysis. The description of revolution time determination is explained in Sec. 4.3.2. Figure 4.18 shows the comparison between the revolution time spectrum of the present experiment (labeled as 2010 with red color) with the spectrum from the previous one (Experiment 2006, black color). To make a comparison the intensity of the revolution time spectrum from 2006 was normalized to 104 and from 2010 to 6. As one can see the range of revolution times from both experiments coincides quite well. To make sure that the number of ions per injection will not influence the detection efficiency only the injections with one ion inside are used in the analysis. Figure 4.19 shows the development of an average detected number of ions per turn for the data from both IMS experiments with uranium fission fragments. At turn number 10 the results of both experiments were normalized to 1.6 ions. From the figure it

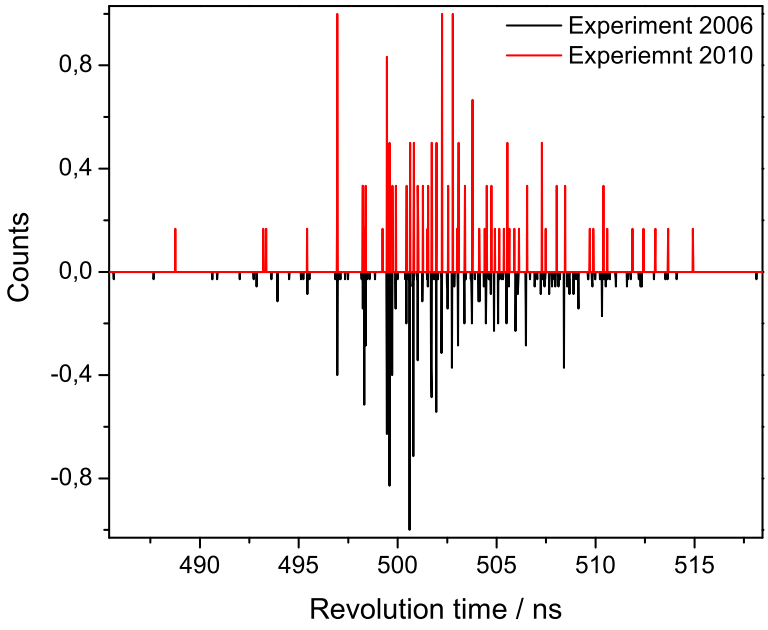

Figure 4.18: Comparison of revolution time spectra from present (indicated as 2010 with red color) and from previous (2006, black color) experiments with uranium fission fragments. Because of difference in intensity the revolution times from 2010 spectrum was normalized to 104 and from 2010 spectrum to 6. The spectrum for previous experiment is inverted for better comparison. Two spectra coincide quite well meaning that the same mass-to-charge ratio range of the ions in both experiments is observed.

is obviously seen that the experimental data measured using MCPs with 5 μm pore size and thin carbon foil (violet squares) is almost constant over about 1000 turns, while for the experiment where MCPs with 10 μm pore size and thicker CsI:C:CsI foil (black squares) were used, this dependence drops already at turn number 100. For the carbon foil with a thickness of 17 $\mu g/cm^2$ coated with a CsI of 10 $\mu g/cm^2$ on both sides the energy loss is 86 keV ($^{86}As^{33+}$, 386.3 MeV/u), while for the pure carbon foil with a thickness of 10 $\mu g/cm^2$ the energy loss is 31 keV. That is a factor of 2.7 less. According to Figure 4.18 the m/q range is definitely similar in both experiments. Therefore the comparison is fair between two experiments.
The experimental results with ^{238}U fission fragments (Figure 4.19) as well as with $^{20}Ne^{10+}$ stable beam (Figure 4.17) showed approximately 8-10 times longer ions revolutions in the ring. These achievements are attributed to:

- a factor of 2-2.7 less energy loss because of a thinner carbon foil installed in the TOF detector;

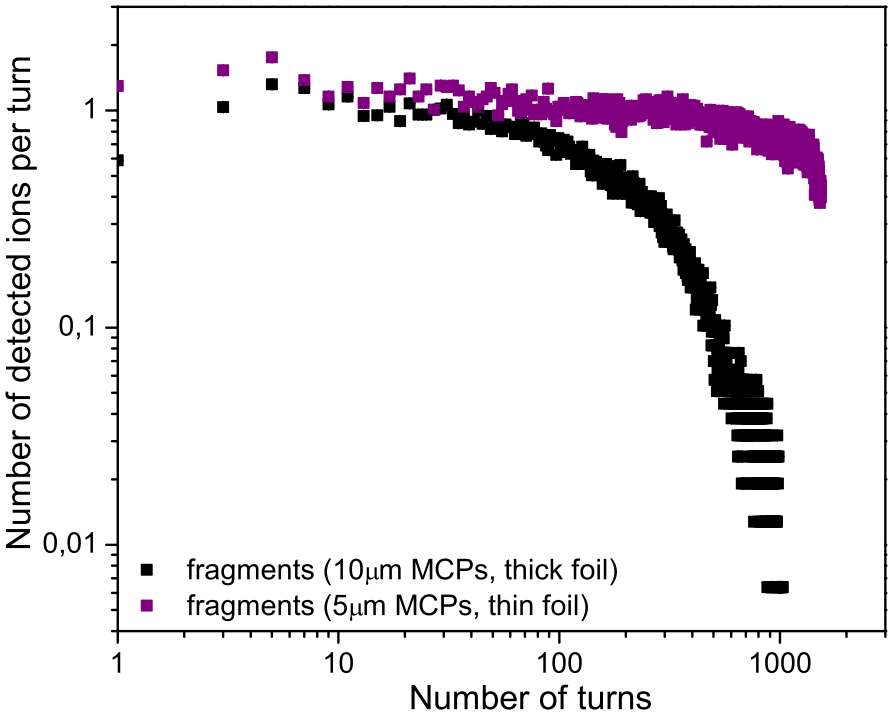

Figure 4.19: Change in the average number of detected ions in the ring per turn for the data with ^{238}U fission fragments. The experimental data where MCPs with 5 μm pore size and a thin carbon foil were used is shown with violet squares. The sharp edge of the violet curve is explained by the maximum record length set in the oscilloscope of 800 μs what corresponds to about 1600 turns. The data for the experiment in 2006 using MCPs with 10 μm pore size and a thicker carbon foil coated with CsI is indicated with black squares. The data for both experiments are normalized at turn number 10 to 1.6 ions. The mass-to-charge ratio range of the ions is the same in both experiments. Using a thin carbon foil, which caused a factor of 2.7 less energy loss and 4 times higher rate resistant MCPs with 5 μm pore size up to 10 times more turns of the ions circulating in the ring are observed.

- 4 times increase in rate capability of the MCP detector using microchannel plates with 5 μm pore size.

The results from both experiments prove that one indeed will observe higher number of turns of the circulated ions in the ring and therefore improve the detection efficiency and mass measurement accuracy.

A	Z	N	Element	ME [keV]	ΔME [keV]	Reference source
79	31	31	Ga	-62547.6	1.9	[Hak 08]
81	32	32	Ge	-66291.7	2.1	[Hak 08]
83	33	33	As	-69669.3	2.8	[Hak 08]
83	32	32	Ge	-60976.3	2.5	[Hak 08]
84	33	33	As	-65853.5	3.2	[Hak 08]
86	34	34	Se	-70503.2	2.5	[Hak 08]
87	34	34	Se	-66426.1	2.2	[Hak 08]
88	35	35	Br	-70716	4	[Rah 07]
88	34	34	Se	-63884.1	3.3	[Hak 08]
88	33	33	**As**	-51290 #	500#	[Aud 03]
89	35	35	Br	-68275	4	[Rah 07]
91	36	36	Kr	-70973.9	2.3	[Del 06]
92	36	36	Kr	-68769.3	2.7	[Del 06]
93	37	37	Rb	-72613	9	[Rai 02]
93	36	36	Kr	-64136	2.5	[Del 06]
94	37	37	Rb	-68564	9	[Rah 07]
94	35	35	**Br**	-47800#	400#	[Aud 03]
95	37	37	Rb	-65935	4	[Rah 07]
96	38	38	Sr	-72926	10	[Hag 06]
97	38	38	Sr	-68587	10	[Hag 06]
98	38	38	Sr	-66431	10	[Hag 06]
99	39	39	Y	-70654	8	[Hag 07b]
100	39	39	Y	-67332	12	[Hag 07b]
101	39	39	Y	-65065	8	[Hag 07b]
102	40	40	Zr	-71590	10	[Hag 06]
103	40	40	Zr	-67819	10	[Hag 06]
104	41	41	Nb	-71823	5	[Hag 07b]
104	40	40	Zr	-65728	10	[Hag 06]
105	41	41	Nb	-69907	5	[Hag 07b]
106	42	42	Mo	-76139	10	[Hag 06]
106	41	41	Nb	-66195	5	[Hag 07b]
107	42	42	Mo	-72556	10	[Hag 06]
107	41	41	Nb	-63715	9	[Hag 07b]
108	42	42	Mo	-70760	10	[Hag 06]
111	43	43	Tc	-69018	11	[Hag 07a]
114	44	44	Ru	-70213	13	[Hag 07a]
116	45	45	Rh or Rh^m	70642	9	[Hag 07a]

122	47	47	**Ag**	-71230#	210#	[Aud 03]
129	49	49	In	-72940	40	[Aud 03]
131	50	50	Sn	-77264	10	[Dwo 08]
132	50	50	Sn	-76547	7	[Dwo 08]
133	51	51	Sb	-78951	25	[Fog 99]
136	52	52	Te	-74430	50	[Aud 03]
137	52	52	Te	-69560	120	[Aud 03]
140	53	53	I	-63773	95	[Kno 08]
141	53	53	I	-60127	112	[Kno 08]
146	55	55	Cs	-55620	70	[Aud 03]
147	55	55	Cs	-52011	60	2008
164	64	64	**Gd**	59750#	400#	[Aud 03]

Table 4.1: Overview of the nuclides, which were identified in this experiment but because of lack of statistics (measurement time $\sim$ 7 h) the mass values could not be determined. The mass values (ME) and the corresponding errors (ΔM) are taken from the reference sources presented in the last column. The masse value labeled with # sign are predicted values from extrapolations. The nuclides with unknown masses which were identified in this experiment indicated with bold and red color.

Chapter 5

Summary

At GSI Darmstadt the technique of Isochronous Mass Spectrometry (IMS) has been developed for direct mass measurements of exotic nuclides. In this method a cocktail beam of highly-charged ions is produced via projectile fragmentation or fission, separated in the FRagment Separator (FRS) and injected into the Experimental Storage Ring (ESR) operated in an isochronous mode. The mass of the exotic nuclei can be deduced from precise revolution time measurements by a time-of-flight (TOF) detector placed in the ESR. In the detector ions passing a thin foil release secondary electrons, which are transported to two microchannel plate (MCP) detectors in forward and backward directions by electric and magnetic fields. In this work the performance characteristics of the detector were investigated by simulations and by offline and online experiments and significantly improved. In particular the timing performance and the rate capability were measured and enhanced. The detection efficiency improvements developed in previous work were verified and the use of thinner carbon foils to increase the number of turns of the ions in the ring were implemented. This work also forms a basis for the development of a dual detector system for IMS in the collector ring at FAIR.

Since the masses of exotic nuclides are determined from the revolution time measurements, the timing properties of the detector directly influence the mass accuracy. In this work the main contributions to the TOF detector timing such as the transport time of the secondary electrons, the electron transit time through the MCPs and the method of determination of the event time from the MCP signals (event time determination) were analyzed and improved. The timing accuracy of the TOF detector was investigated by coincidence time-of-flight measurements. The timing uncertainty of a

single branch of the detector with standard settings was measured in the laboratory with an α source and amounts to σ_{branch}=48 ps. In an online experiment at the ESR using MCPs with 5 μm pore sizes the timing accuracy was measured as σ_{branch}=48 ps with a stable ^{20}Ne beam and σ_{branch}=45 ps with ^{238}U fission fragments. Those measurements were performed for the kinetic energy of the secondary electrons (K) equals 700 eV.

To improve the transport time of secondary electrons the TOF detector was modified for higher values of electric and magnetic fields. An improved time spread σ_{branch}=37 ps was obtained in the measurements with α-particles using MCPs with 10 μm channel diameter for an kinetic energy of 1400 eV of the secondary electrons.

The contribution from the transit time through the MCP channels to the time spread was investigated with α-particles as a function of different electron yields from the carbon foils. Using a higher thickness of the carbon foil timing is not improved significantly. Therefore, 10 $\mu g/cm^2$ is an optimum for the carbon foil thickness in the matter of efficiency and timing. In case of a foil with a Cs-compound on the surface, for which the number of secondary electrons is increased by a factor of 10, the timing was improved to σ_{branch}=27 ps (K=1400 eV).

A newly constructed anode design improves the bandwidth of the MCP detector by a factor of 2 leading to a reduction in the width of the MCP signals by a factor of two to an improvement of the rise time by about 20 %. The signal shape of the MCP detector influences the determination of the revolution times of the ions in the ring and thus the mass measurement accuracy.

Due to the high revolution frequencies of the ions in the ESR ($\sim$2 MHz) a high rate capability detector is required. In the offline experiments the saturation effect of the MCPs was investigated with an electron beam using MCPs with 10 μm and 5 μm pore sizes. The rate acceptance of the MCP detector was improved by a factor of 4 due to the larger number of channels of MCPs with 5 μm pore size.

At each turn in the ESR the ions pass the foil and lose energy. According to simulations the decrease of the foil thickness by a factor of two allows to double the number of ion revolutions in the ring. To store ions for a longer time in the ESR a thinner carbon foil with a thickness of 10 $\mu g/cm^2$ and MCPs with a 5 μm channel diameter were installed in the TOF detector and used for the first time in the online experiments. The results of the experiments measured with $^{20}Ne^{10+}$ stable beam and ^{238}U fission fragments were compared to the results of the previous experiments. In the previous experiments a carbon foil with a thickness of 17 $\mu g/cm^2$ coated with 10 $\mu g/cm^2$ of

CsI on both sides, which caused a calculated energy loss of 86 keV ($^{86}As^{33+}$, 386.3 MeV/u) and MCPs with 10 μm pore size were used. For the carbon foil of 10 $\mu g/cm^2$ the calculated energy loss is 31 keV, that is a factor of 2.7 less than for the thicker foil. Summing up the results, with thinner carbon foil and higher rate resistance MCPs with 5 μm pore sizes in the TOF detector up to ten times more ion revolutions in the ring were observed. With larger number of turns in the ring one increases the detection efficiency and the mass measurement accuracy. Although the measurement time in the experiment with ^{238}U fission fragments was strongly limited (about 7 h), the measured ions could be identified and compared with results from previous experiments.

Chapter 6

Outlook

6.1 Further Improvements of the TOF Detector

In the offline experiments with twice higher kinetic energy of the secondary electrons (SE) a standard deviation σ_{branch}=37 ps of the coincidence time-of-flight distribution was achieved. *ITSIM* simulations show that an increase in the kinetic energy of the SE by a factor of three leads to improvements in the transport time of SE to forward and backward MCP detectors of about $\sigma_{\text{branch}}(Transport)$ to 17 ps. Currently the time-of-flight detector is upgraded to allow for a kinetic energy of the SE of up to 2100 eV.
The transport of SE from the foil to the MCP detectors is only one of the contributions to the timing limitation of the TOF detector. To improve the MCP signal quality the new anode design will be implemented in the TOF detector. With the new anode the bandwidth of the MCP detector is increased up to 2 GHz, which reflects an improvement by a factor of two. Since the distance between last microchannel plate and the anode plate is increased in the new design, the action of the magnetic field has to be compensated with a higher electric strength inside the MCP detector. The voltages applied per microchannel plates will be kept constant to obtain the same peaked pulse-hight distribution but the potential difference between last MCP and anode plate has to be increased up to about 800 eV.
Further investigations can be conducted with a picosecond laser to perform spatially resolved measurements of the timing accuracy of the TOF detector. Offline experiments showed that a wavelength of 357 nm, a pulse width of $<$25 ps and a peak energy of $\approx$2 μJ is required. A picosecond laser could be also used for verifying the timing characteristics of the TOF detector during the preparation of an IMS experiment at the ESR.
Other plans for the detector include position-sensitive detection using a

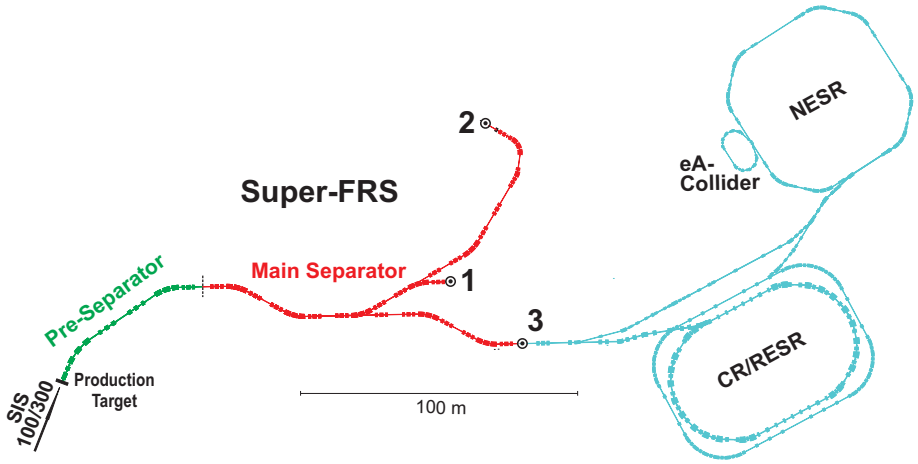

Figure 6.1: Layout of the FAIR facility with Super-FRS and three experimental branches: 1. The high-energy branch; 2. The low-energy branch; 3. The storage ring complex (CR-RESR-NESR) with electron-ion collider (eA) [Lit 08].

delay-line detector. This would allow for an experimental investigation of the dynamics of the ion motion in the ring and potentially for a correction of time-of-flight variations caused by the large beam emittance.

6.2 Isochronous Mass Spectrometry at FAIR

The future project FAIR - **F**acility for **A**ntiproton and **I**on **R**esearch [FAI] is a new generation international facility in Europe with huge discovery potential for new mass measurements. At the FAIR facility (Figure 6.1), the new fragment separator Super-FRS [Gei 03] [Win 08] will provide beams of exotic nuclei with unprecedent intensity, a factor 1000 of the present primary beam intensities. With the ILIMA (**I**someric **B**eams, **L**ifetimes and **M**asses) project at the NuSTAR (**N**uclear **S**tructure, **A**strophysics and **R**eactions) facility the research at the new **C**ollector **R**ing (CR) will cover life-time and mass measurements of very short lived nuclides and isomer separation.
Isochronous Mass Spectrometry will be performed at the CR in combination with the Super-FRS and thus substantially extend the reach of mass measurements to more exotic ions. For these measurements a dual time-of-flight detector system will be developed. The layout of the storage-ring facilities for direct mass and half-life measurements and studies with isomeric beams in the FAIR project ILIMA is shown in Figure 6.2.
The dual TOF detector system for the ILIMA project is indicated in the CR lattice. With the dual TOF detector system placed on the straight section of the CR it will be possible to correct for a non-perfect isochronicity of the

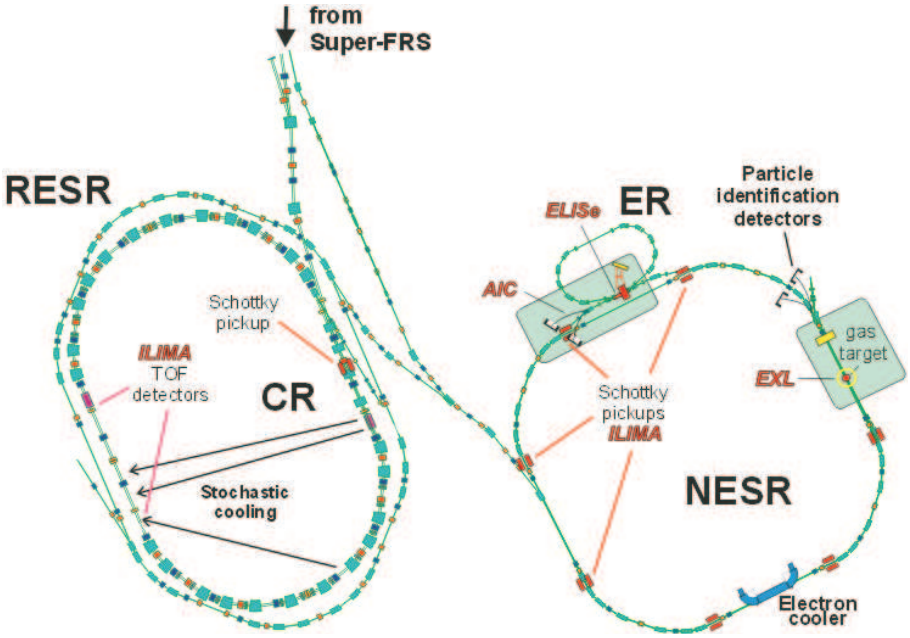

Figure 6.2: Layout of the NuSTAR facility for direct mass and half-life measurements in the FAIR project ILIMA [ILI]. Isochronous mass measurements as well as the half-life measurements of short lived nuclei will be performed at the CR. The position of the dual TOF detector system for the revolution time measurements is indicated on the strait sections of the CR. Nuclides with half-lives longer than about 1 s will be stochastically precooled and injected via RESR into the NESR. To decrease the energy spread of the ions they would be cooled by electron cooling and Schottky Mass Spectroscopy can be performed. The components for other collaborations are also indicated.

ring, since the velocity of the ions can be measured in addition to the ion's revolution times.

Appendix

Time Measurement Accuracy with Ddelay Function

The analysis begins by computing a histogram of the waveform data over the time interval spanned by the cursors or restricted by the record length of the oscilloscope display setting (see Figure 1). The function first scan the spectrum and attempt to identify the region of the waveform that contains the largest density. Then the most probable state (centroid) will be computed to determine the top and the base reference level: the top line corresponds to the top and the base line to the bottom centroid [LeC 07]. Once the top and base are estimated the function determines time between

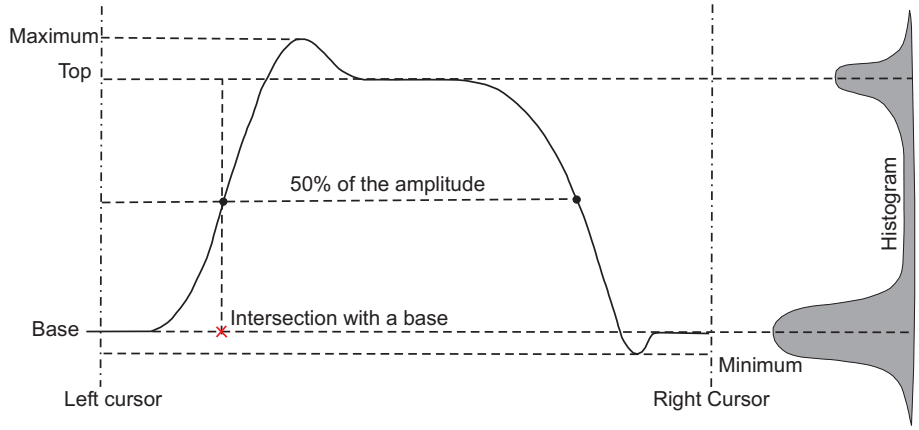

Figure 1: Determining of top and base lines of the waveform for calculations with a digital oscilloscope LeCroy WaveRunner 6000A Series [LeC 07].

first crossing of 50% amplitude levels of two signals.
The time interval measurement accuracy of WaveMaster series oscilloscopes is expressed in the form: $\pm((0.06\cdot$ Sample Interval)+(1 ppm of measured interval)). The second component represents the uncertainty due to the scope's timebase and it is a minor contribution in case of LeCroy scopes. The first component is related to the scope's measurement interpolator. The interpolator is a software component that measures the location in time at

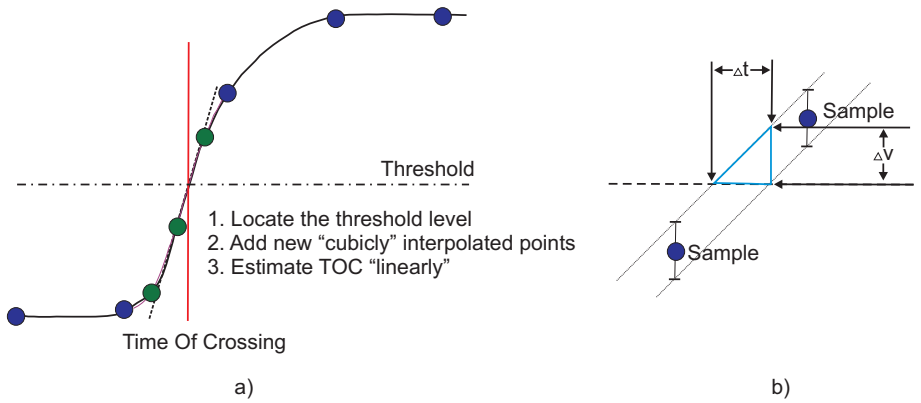

Figure 2: a) A graphical view of measurement interpolation showing how the TOC is determined on a sampled waveform. b) A simple model illustrating the mapping of vertical uncertainty into timing uncertainty [LeC].

which the signal crosses a given threshold value (in this case at 50% of the amplitude level). Interpolation is automatically performed in the scope when three or fewer samples exist on any given edge. A graphical view of measurement interpolation is shown in in Figure 2 a). Only the points surrounding the threshold crossing are interpolated for the measurement. To find a crossing point, a cubic interpolation is used, followed by a linear fit to the interpolated data.

The accuracy of the interpolation is dependent mainly on the transition time of the signal, the sampling rate, vertical noise and effective vertical resolution. The relationship between the vertical resolution and time resolution is

$$\Delta t = \Delta V/dV/dt, \tag{1}$$

where Δt and ΔV are time and amplitude uncertainties and dV/dt is slope of the transition [LeC]. Figure 2 b) shows a typical calculation.

For instance, for signal with an amplitude of 50 % of full scale, 490 ps edge sampled at 10 Gsample/s using an 8 bit digitizer the vertical uncertainty is 1/256 and base on the slope of 0.5 of full scale over 4.9 samples (490 ps at 100 ps/sample) the equivalent time uncertainty works out to:

$$\Delta t = (1/256)/(0.5/4.9) = 0.04. \tag{2}$$

Since the sampling period is 100 ps the uncertainty for this measurement is 0.04 sample periods · 100 ps /sample=4 ps. This timing uncertainty applies to any single measurement. The uncertainty of the mean of the measured values decreases with multiple measurements.

Bibliography

[Agr 70] V. M. Agranovich et al. "Study of the energy spectrum of secondary electrons arising from passage of α particles and fission fragments through thin foils". Soviet. Phys. JETP, Vol. 302, p. 220, 1970. [cited at p. 32]

[Agr 73] U. Agrifov, L. Kishinevshii, E. Mukhamadiev, and E. Parilis. Sov. Phys. Tech. Phys., Vol. 18, 1973. [cited at p. 26]

[Ahl 78] S. Ahlen. "Z_1^7 stopping power formula for fast heavy ions". Phys. Rev. A, Vol. 17, number = 3, pages = 1236,, 1978. [cited at p. 19]

[Ahl 80] S. Ahlen. "Theoretical and experimental aspects of the energy loss of relativistic heavily ionizing particles". Rev. Mod. Phys., Vol. 52, No. 1, p. 121, 1980. [cited at p. 19]

[ATI] ATIMA. "Atomic Interaction with Matter". http://www-linux.gsi.de/∼weick/atima/. [cited at p. 20, 23]

[Aud 03] G. Audi, A. Wapstra, and C. Thibault. "The AME 2003 atomic mass evaluation". Nuclear Physics A, No. 729, p. 337, 2003. [cited at p. 2, 92, 93, 99, 102, 103]

[Aye 10] S. Ayet et al. "A Fast Microchannel-Plate Detector and High-Performance Electronics for Signal Conditioning". In: Verhandlungen der Deutschen Physicalichen Gesellschaft e.V., p. Fachverband Physik der Hadronen und Kerne. HK 377 Poster, 74. Jahrestagung der DPG und DPG Frühjahrstagung, Bonn, 15-19 März 2010. [cited at p. 59, 61, 62]

[Aye 11] S. Ayet et al. "A sub-nanosecond Microchannel-Plate Detector Development". In: Verhandlungen der Deutschen Physicalichen Gesellschaft e.V., p. Fachverband Massenspektrometrie. MS 3.12

Poster, 74. Jahrestagung der DPG und DPG Frühjahrstagung, Dresden, 13-18 März 2011. [cited at p. 59, 61]

[Ays 01] J. Äystö. "Development and application of the IGISOL technique". Nucl. Phys. A, No. 693, p. 477, 2001. [cited at p. 11]

[Bar 69] W. Barkas, J. Dyer, and H. Heckmann. "Resolution of the Σ^- -mass anomaly". Phys. Rev. Lett., Vol. 11, No. 3, p. 26, 1969. [cited at p. 20]

[Ber 63] C. A. Bertulani. "Electromagnetic Processes in Relativistic Heavy Ion Collisions". Phys. Rep., Vol. 163, No. 5,6, p. 299, 1963. [cited at p. 22]

[Ber 90] M. Berz. "Arbitrary order description of arbitrary particle optival systems". Nucl. Instr. and Meth. in Phys. Res. A, No. 298, p. 426, 1990. [cited at p. 22]

[Bet 30] H. Bethe. "Theory of the passage of fast corpuscular rays through matter". Annalen der Physik (Leipzig), Vol. 5, p. 325, 1930. [cited at p. 9]

[Bla 06] K. Blaum. "High-accuracy mass spectrometry with stored ions". Phys. Reports, No. 425, p. 1, 2006. [cited at p. 3]

[Bla 92] B. Blasche and B. Franczak. "The Heavy Ion Synchrotron SIS". Proceedings of European Particle Accelerator Conference (EPAC), Vol. 9, p. 37, 1992. [cited at p. 9]

[Blo 07] M. Block et al. "Mass Measurements of exotic nuclides at SHIPTRAP". In: American Institute of Physics (AIP), Khanty-Mansiysk (Russia), p. 423, 2007. [cited at p. 11]

[Boh 13] N. Bohr. "On the theory of the decrease of velocity of moving electrified particles on passing through matter". Philos. Mag., Vol. 25, p. 10, 1913. [cited at p. 19]

[Boh 15] N. Bohr. "On the decrease of velocity of swift moving electrified particles in passing through matter". Philos. Mag., Vol. 30, p. 581, 1915. [cited at p. 19]

[Bol 96] G. Bollen et al. "ISOLTRAP: a tandem Penning trap system for accurate on-line mass determination of short-lived isotopes". Nucl. Instr. and Meth. in Phys. Res. A, No. 368, p. 675, 1996. [cited at p. 11, 12]

[Bor 91] J. E. Borovsky and D. M. Suszcynsky. "Reduction of secondary electron yields by collective electric fields within metals". Phys. Rev. A, Vol. 43, No. 3, p. 1416, 1991. [cited at p. 30]

[Bos 03] F. Bosch. "Schottky mass- and lifetime-spectrometry of unstable, stored ions". J. Phys. B, No. 36, p. 585, 2003. [cited at p. 14]

[Bow 78] J. Bowman and R. Heffner. "A novel zero time detector for heavy ion spectroscopy". Nucl. Instr. and Meth., Vol. 148, p. 503, 1978. [cited at p. 24, 34]

[Bri 02] P. Bricault. "TRIUMF-ISAC target station and mass separator commissionning". Nucl. Phys. A, No. 701, p. 49, 2002. [cited at p. 6]

[Bro 67] K. L. Brown. Ad. Particle Phys., Vol. 1, 1967. [cited at p. 22]

[Bru 97] A. Brunelle, P.Chaurand, S. Della-Negra, Y. L. Beyec, and E. Parilis. "Secondary Electron Emission Yelds from a CsI Surface Under Impacts of large Molecules at Low Velocities". Rap. Comm. in Mass. Spectr., Vol. 11, p. 353, 1997. [cited at p. 26, 37, 38, 40]

[Bry 93] P. Bryant and K. Johnsen. "The principles of circular accelerator and storage rings". Cambridge University Press, 1993. [cited at p. 17]

[COM] COMSOL. COMSOL Multiphysics, www.comsol.de. [cited at p. 35]

[CST] CST. Computer Simulation Technologies, CST Microwave Studio. www.cst.com. [cited at p. 59, 60]

[Das 07] C. Dass. Fundamentals of Contemporary Mass Spectrometry. Willey-Interscience, 2007. [cited at p. 16]

[Del 06] P. Delahaye et al. "High-accuracy mass measurements of neutron-rich Kr isotopes". Phys. Rev. C, No. 74, p. 034331, 2006. [cited at p. 102]

[Det 74] K. Dettman, K. G. Harrison, and M. W. Lucas. "Charge exchange to the continuum for light ions in solids". J. Phys. B, Vol. 7, No. 2, p. 269, 1974. [cited at p. 31]

[Dev 91] J. Devooght. Particle Induced Electron Emission I. Vol. 122, Springer Tracts in Modern Physics, 1991. [cited at p. 28]

[Dil 01] J. Dilling. Direkte Massenmessungen an exotische Kernen mit SHIPTRAP und ISOLTRAP. PhD thesis, Universität Heidelberg, 2001. [cited at p. 11]

[Dil 06] J. Dilling et al. "Mass Measurements on highly charged radioactive ions, a new approach to high precision with TITAN". Int. J. of Mass Spectrom., No. 251, p. 198, 2006. [cited at p. 11]

[Diw 09] M. Diwisch. "Untersuchung zur Steigerung der Ratenakzeptanz eines Flugzeitdetektors für isochrone Massenmessungen an FRS-ESR bei GSI". Bachelor's Thesis, Justus-Liebig Universität Gießen, 2009. [cited at p. 69, 71, 72]

[Diw 11] M. Diwisch. Verbesserungen der Zeiteigenschaften eines Flugzeitdetektors für die isochrone Massenspektrometrie am FRS-ESR bei GSI. Master's thesis, Justus-Liebig Universität Gießen, 2011. [cited at p. 47, 52]

[Dre 96] C. G. Drexler and R. D. DuBois. "Energy - and angle differential yields of the electron emission from thin carbon foils after fast proton impact". Phys. Rev. A, Vol. 53, No. 3, p. 1630, 1996. [cited at p. 26, 27, 32, 48]

[Dwo 08] M. Dworschak et al. "Restoration of the N=82 Shell Gap from Direct Mass Measurements of $^{132,134}Sn$". Phys. Rev. Lett., No. 100, p. 072501, 2008. [cited at p. 103]

[Ebe 80] E. Eberhardt. "Parameters Pertaining to Microchannel Plates and Microchannel Plate Devices". ITT Technical Note, Vol. 127, 1980. [cited at p. 41]

[Edw 07] C. Edwards. "NEEP 427-Pulse Timing". Lesson 13, University of Wisconsin-Madison, College of Engineering, 2007. [cited at p. 59]

[Eic 95] J. Eichler and W. Meyerhof. "Relativistic Atomic Collisions". Academic Press, 1995. [cited at p. 21]

[Enc] Encyclopedia. The free dictionary. http://encyclopedia2.the freedictionary.com/channel+electron+multiplyer. [cited at p. 36]

[Fab 08] B. Fabian. Characterization and Optimization of a Time-of-Flight Detector for Isochronous Mass Measurement at the ESR. PhD thesis, Justus-Liebig Universität Gießen, 2008. [cited at p. 35, 43, 64, 66, 67, 68, 69, 78, 80, 95, 96, 98]

[FAI] FAIR. FAIR project: Facility for Antiproton and Ion Research. http://www.gsi.de/fair/. [cited at p. 110]

[Fog 99] B. Fogelberg et al. "Precise Atomic Mass Values near ^{132}Sn: the Resolution of a Puzzle". Phys. Rev. Lett., Vol. 82, No. 9, p. 1823, 1999. [cited at p. 103]

[Fra 08] B. Franzke, H. Geissel, and G. M*ü*nzenberg. "Mass and lifetime measurements of exotic nuclei in storage rings". Mass Spectrom. Rev., No. 27, p. 428, 2008. [cited at p. 3, 13]

[Fra 83] B. Franczak. Proc. Europhysics Conf. on Computing in Accelerator Design and Operation, Berlin, 1983. [cited at p. 22]

[Fra 87] B. Franzke et al. "The heavy ion storage and cooler ring prospect ESR at GSI". Nucl. Instr. and Meth. B, No. 24/25, p. 18, 1987. [cited at p. 12, 13]

[Fra 88] G. Fraser, J. Pearson, J. Lees, and W. Feller. Proc. SPIE, Vol. 982, p. 98, 1988. [cited at p. 37]

[Fra 91] G. Fraser, M. Pain, and J. Lees. "The operation of microchannel plates at high count rates". Nucl. Instr. and Meth. in Phys. Res. A, No. 306, p. 247, 1991. [cited at p. 42]

[Fra 92] G. Fraser and J. Lees. "Micro channel plate at high count rates: further studies". Nucl. Instr. and Meth. in Phys. Res. A, No. 327, p. 328, 1992. [cited at p. 42]

[Gei 03] H. Geissel et al. "The Super-FRS progect at GSI". Nucl. Instr. and Meth. B, No. 204, p. 71, 2003. [cited at p. 10, 110]

[Gei 92] H. Geissel, P. Armbruster, K. Behr, et al. "The GSI projectile fragment separator (FRS): a versatile magnetic system for relativistic heavy ions". Nucl. Instr. and Meth. in Phys. Res. B, No. 70, p. 286, 1992. [cited at p. 7, 9, 22]

[Gei 95] H. Geissel, G. Münzenberg, and K. Riisager. "Secondary Exotic Nuclear Beams". Annu. Rev. Nucl. Part. Sci., No. 45, p. 163, 1995. [cited at p. 7, 10]

[Giu 94] L. Giudicotti, M. Bassan, R. Pasqualotto, and R. Sardella. "Simple analytical model of a gain saturation in micro channel plate devices". Rev. Sci. Instr., Vol. 65(1), p. 247, 1994. [cited at p. 42]

[GSI] GSI. Facility at GSI. http://www.gsi.de/portrait/index_e.html. [cited at p. 8]

[Hag 06] U. Hager et al. "Pirst Precision Mass Measurements of Refractory Fission Fragments". Phys. Rev. Lett., No. 96, p. 042504, 2006. [cited at p. 102]

[Hag 07a] U. Hager et al. "Precision mass measurements of neutron-rich Tc, Ru, Rh and Pd isotopes". Phys. Rev. C, No. 75, p. 064302, 2007. [cited at p. 12, 99, 102]

[Hag 07b] U. Hager et al. "Precision mass measurements of neutron-rich yttrium and niobium isotopes". Nucl. Phys. A, No. 793, p. 20, 2007. [cited at p. 102]

[Hag 74] H. Hagstrum. Phys. Rev. 96, p. 336, 1974. [cited at p. 26]

[Hag 92] E. Hagebø et al. "New Production Systems at ISOLDE". Nucl. Instr. and Meth. in Phys. Res. B, No. 70, p. 165, 1992. [cited at p. 6]

[Hak 08] J. Hakala et al. "Evolution of the N=50 Shell Gap Energy Towards ^{78}Ni". Phys. Rev. Lett., No. 101, p. 052502, 2008. [cited at p. 102]

[Ham 06] Hamamatsu. "Technical information: MCP Assembly". Tech. Rep., Hamamatsu Photonics, 2006. [cited at p. 38]

[Has 98] D. Hasselkamp, H. Rothard, K. Groeneveld, J. Kemmler, P. Varga, and H. Winter. Particle Induced Electron Emission. Vol. 123, Springler Tracts in Modern Physics, 1998. [cited at p. 27, 28, 29, 30, 31, 32]

[Hau 00] M. Hausmann et al. "First Isochronous mass spectrometry at the experimental storage ring ESR". Nucl. Instr. and Meth. in Phys. Res. A, No. 446, p. 569, 2000. [cited at p. 13, 15]

[Hau 99] M. Hausmann. Energieisochrone Massenmesssungen am Experimentierspeicherring der GSI. PhD thesis, Justus-Liebig Universität Gießen, 1999. [cited at p. 47, 82, 87]

[Her 03] F. Herfurth et al. "Mass measurements and nuclear physics - recent results from ISOLTRAP". J. Phys. B, No. 36, p. 931, 2003. [cited at p. 11]

[Her 69] G. Herrmann and H. Denschlag. "Rapid Chemical Separations". Annu. Rev. Nucl. Sci., No. 19, p. 1, 1969. [cited at p. 6]

[ILI] ILIMA. ILIMA project: Isomeric Beams, Lifetimes and Masses, Technical Proposal. http://www.gsi.de/forschung/fair_experiments/NUSTAR/. [cited at p. 111]

[Ina 06] K. Inami et al. "A 5 ps TOF-counter with an MCP-PMT". Nucl. Instr. and Meth. in Phys. Res. A, No. 560, p. 303, 2006. [cited at p. 37, 56]

[Iwa 97] N. Iwasa et al. "MOCADI, a universal Monte Carlo code for the transport of heavy ion through matter within ion-optical systems". Nucl. Instr. and Meth. in Phys. Res. B, No. 126, p. 284, 1997. [cited at p. 22, 93]

[Jac 72] J. Jackson and R. McCarthy. "Z^3 Corrections to Energy Loss and Range". Phys. Rev. B, Vol. 6, No. 11, p. 4131, 1972. [cited at p. 20]

[Jun 96] M. Jung, H. Rothard, B. Gervais, and J. Grandin. "Transport of electrons induced by highly charged Ni (74 MeV/u) and Cu (9.6 MeV/u) ions in carbon: A study of target-thickness-dependent electron yields". Phys. Rev. A, Vol. 54, No. 5, p. 4153, 1996. [cited at p. 29, 30, 56]

[Kno 08] R. Knoebel. Neuartige Isochrone Massenmessung kurzlebiger neutronenreicher, gespeicherter Kerne am FRS-ESR. PhD thesis, Justus-Liebig Universität Gießen, 2008. [cited at p. 13, 15, 81, 82, 91, 94, 99, 103]

[Kos 89] P. Koschar, K. Kroneberger, A. Clouvas, and M. Burkard. "Secondary electron yield as a probe of preequilibrium stopping power of heavy ions in the keV region". Phys. Rev. A, Vol. 40, No. 7, 1989. [cited at p. 28, 29, 35]

[Kuz 07] N. Kuzminchuk. Study of charge-state distribution and slowing-down of 40-200 MeV/u heavy ions in solid. Master's thesis, Tomsk Polytechnic University. Tomsk, Russia), 2007. [cited at p. 20]

[LeC] LeCroy. "Time Measurement Accuracy: A Discussion Of Factors Affecting Time Interval Accuracy". LeCroy Application Brief No. LAB WM441, LeCroy Corporation. [cited at p. 114]

[LeC 07] LeCroy. LeCroy WaveRunner 6000A series Oscilloscopes. Operators Manual. LeCroy Corporation, February 2007. 156. [cited at p. 113]

[Leh 07] A. Lehmann, A. Britting, W. Eyrich, C. Pizzolotto, and A. Teufel. "Studies of Microchannel Plate PMTs for the PANDA DIRC". GSI Scientific Report 2009, Vol. FAIR-Experiemnts-33, p. 35, 2007. [cited at p. 37, 38]

[Leo 87] W. Leo. Techniques for Nuclear and Particle Physics Experiments. Springer-Verlag Berlin Heidelberg, 1987. [cited at p. 19, 83]

[Lin 61] J. Lindhard and M. Scharf. "Energy dissipation by ions in the keV region". Phys. Rev., Vol. 124, No. 1, p. 128, 1961. [cited at p. 20]

[Lin 76] J. Lindhard. "The Barkas effect - or Z_p^3, Z_p^4 corrections to the energy loss and range". Nucl. Instr. and Meth., No. 132, p. 1, 1976. [cited at p. 20]

[Lin 96] J. Lindhard and A. Sørensen. "Relativistic theory of stopping for heavy ions". Phys. Rev. A, Vol. 53, No. 4, p. 2443, 1996. [cited at p. 19]

[Lit 05] Y. Litvinov et al. "Mass measurements of cooled neutron-deficient bithmuth projectile fragments with time-resolved Schottky mass spectrometry at the FRS-ESR facility". Nucl. Phys. A, No. 756, p. 3, 2005. [cited at p. 13]

[Lit 08] S. Litvinov. Investigation of the Isochronous Mode of the Experiemntal Storage Ring (ESR) and the Collector Ring (CR). Decay Spectroscopy of Highly Charged Stored ^{140}Pr Ions at the FRS-ESR Facility. PhD thesis, Justus-Liebig Universität Gießen, 2008. [cited at p. 9, 17, 110]

[Lit 10] Y. Litvinov et al. "Direct mass measurements of exotic nuclei in storage rings". Acta Physica Polonica B, Vol. 41, No. 2, p. 511, 2010. [cited at p. 11, 12, 13]

[Lou 74] D. Loubet and C. Barat. "Energy distribution of output electrons in a curved channel". Nucl. Instr. and Meth., No. 118, p. 259, 1974. [cited at p. 32]

[Lun 03] D. Lunney, J. M. Pearson, and C. Thibault. "Recent trends in the determination of nuclear masses". Rev. Mod. Phys., Vol. 75, p. 1021, 2003. [cited at p. 2, 3]

[Mat 04] M. Matoš. Isochronous Mass Measurements of Short-Lived Neutron Rich Niclides at the FRS - ESR Facilities. PhD thesis, Justus-Liebig Universität Gießen, 2004. [cited at p. 15, 83, 84, 86, 90]

[Mon 88] B. Monart. PhD thesis, Universit*é* Paris, 1988. [cited at p. 38]

[Mor 89] D. J. Morrissey. Phys. Rev. C, Vol. 39, No. 2, p. 460, 1989. [cited at p. 22]

[Nat 09] National-Instruments. Tutorial: Top 10 Things to Consider When Selecting a Digitizer/Oscilloscope. http://zone.ni.com/devzone/cda/tut/p/id/4334#toc1, Jun 15 2009. [cited at p. 58]

[NUC 11] NUCS-342. "Fission fragments". In: Introduction to Nuclear science, Simon Fraser Univercity, April 2011. [cited at p. 6]

[Ohy 04] K. Ohya and T. Ishitani. "Monte Carlo Study of secondary electrons emission from SIO_2 induced by focused gallium ion beams". Applied Surface Science, No. 237, p. 606, 2004. [cited at p. 27]

[Pet 08] M. Petrick et al. "Online test of the FRS Ion Catcher at GSI". Nucl. Instr. and Meth. in Phys. Res. B, No. 266, p. 4493, 2008. [cited at p. 10]

[Phoa] Photonics. RP Photonics. Time-Bandwidth Product. http://www.rp-photonics.com/time_bandwidth_product.html. [cited at p. 62]

[Phob] Photonis. Photonis Group. http://www.photonis.com/holding. [cited at p. 37]

[Pla 01] W. R. Plaß. The dependence of RF ion trap mass spectrometry performance on electrode geometry and collisional processes. PhD thesis, Justus-Liebig Universität Gießen, 2001. [cited at p. 35]

[Pla 09] W. Plass. "Aufbau eines Flugzeitmassenspektrometers zur Analyse von flüchtigen organischen Verbindungen bei geringem Partialdruck". Diplomarbeit, Justus-Liebig Universität Gießen, 2009. [cited at p. 60]

[Rad 00] T. Radon et al. "Schottky mass measurements of stored and cooled neutron-deficient projectile fragments in the element range of $57 \leq Z \leq 84$". Nucl. Phys. A, No. 677, p. 75, 2000. [cited at p. 13]

[Rad 94] T. Radon. Aufbau und Test eines schnellen Zeitdetektorsystems. Master's thesis, Justus-Liebig Universitä Gieβen, 1994. [cited at p. 24]

[Rah 07] S. Rahaman et al. "Precise atomic masses of neutron-rich Br and Rb nuclei close to the r-process path". Europ. Phys. Journ. A, No. 32, p. 87, 2007. [cited at p. 102]

[Rai 02] H. Raimbault-Hartmann et al. "High-accuracy mass determination of neutron-rich rubidium and strontium isotopes". Nucl. Phys. A, No. 706, p. 3, 2002. [cited at p. 102]

[Ref 05] H. Refsum, B. Dehning, and J. Koopman. "Simulation of an electron source based calibrating system for an ionisation profile monitor". In: Proceedings of DIPAC 2005, Lyon, France, p. 160, CERN, Geneva, Switzerland, 2005. [cited at p. 70]

[Rin 06] R. Ringle et al. "Precision mass measurements with LEBIT at MSU". Int. J. of Mass Spectrom., No. 251, p. 300, 2006. [cited at p. 11]

[Rog 82] D. Rogers and R. Malina. "Optimization of the performance of a tandem microchannel plate detector as a function of interplate spacing and voltage". Rev. Sci. Instrum., No. 53(9), p. 1438, 1982. [cited at p. 40, 41]

[Rot 90] H. Rothard et al. "Secondary electron yields from thin foils: A possible probe for the electronic stopping power of heavy ions". Phys. Rev. A, Vol. 41, No. 5, p. 2521, 1990. [cited at p. 28, 31]

[Rot 95] H. Rothard et al. "Target-thickness-dependent electron emission from carbon foils bombarded with swiftt highly charged heavy ions". Phys. Rev. A, Vol. 51, No. 4, p. 3066, 1995. [cited at p. 30]

[Sav 06] G. Savard et al. "Studies of neutron-rich isotopes with the CPT mass spectrometer and CARIBU project". Int. J. of Mass Spectrom., No. 251, p. 252, 2006. [cited at p. 11]

[Sch 80] J. Schou. Phys. Rev. B, Vol. 22, No. 5, p. 2141, 1980. [cited at p. 27]

[Sch 90] T. Schwab. PhD thesis, Justus-Liebig Universität Gießen, 1990. [cited at p. 22]

[Sch 93] D. Schneider, G. Schiwietz, and D. DeWitt. "Doubly differential secondary electron yields following 8-MeV/u U^{68+} and 3.5-MeV/u U^{68+} -ion impact on a thin carbon-foil target". Phys. Rev. A, Vol. 47, No. 5, p. 3945, 1993. [cited at p. 30]

[Sch 94] C. Scheidenberger et al. "Direct Observation of Systematic Deviations from the Bethe Stopping Theory for Relativistic Heavy Ions". Phys. Rev. Lett., Vol. 73, No. 1, p. 50, 1994. [cited at p. 19, 20]

[Sch 98] C. Scheidenberger. "Charge state of relativistic heavy ions in matter". Nucl. Instr. and Meth. in Phys. Res. B, No. 142, p. 441, 1998. [cited at p. 21]

[Sea 79] M. P. Seah and W. A. Dench. Surf. Interface Anal., Vol. 1,2, No. Sect. 4.1.2, 4.2, 1979. [cited at p. 27]

[Sha 89] A. Sharma and J. G. Walker. "Effect of local deadtime in imaging detectors". Quantum Opt., No. 1, p. 11, 1989. [cited at p. 41]

[She 02] E. Shefer, A. Breskin, and T. Boutboul. "Photoelectron transport in CsI and CsBr coating films of alkali antimonide and CsI cathodes". Journal of Applied Physics, Vol. 92, No. 8, p. 4758, 2002. [cited at p. 27]

[Sig 00] P. Sigmund. "Shell correction in Bohr stopping theory". Europ. Phys. J. D, No. 12, p. 111, 2000. [cited at p. 20]

[Sig 04] P. Sigmund. Stopping of Heavy ions. A theoretical Approach. Vol. 204, Springer, 2004. [cited at p. 20]

[Ste 04] M. Steck et al. "Electron cooling experiments at the ESR". Nucl. Instr. and Meth. in Phys. Res. A, No. 532, p. 357, 2004. [cited at p. 13, 17]

[Ste 57] E. J. Sternglass. "Theory of secondary electron emission by high speed ions". Phys. Rev., The Second series, Vol. 108, No. 1, 1957. [cited at p. 28, 29]

[Ste 97] M. Steck et al. "Diagnostic methods to detect the properties of cooled heavy ion beams in storage rings". Proceedings of the 3rd international Conference on Nuclear Physics at Storage Rings STORI96, Vol. A, No. 5626, p. 473c, 1997. [cited at p. 18]

[Sto 30] M. Stobbe. Ann. Phys., Vol. 7, p. 601, 1930. [cited at p. 21]

[Sun 08a] B. Sun. Isochronous mass measurement for uranium fission fragments. PhD thesis, Peking University (China), 2008. [cited at p. 13, 47, 82, 87, 94, 99]

[Sun 08b] B. Sun. "Nuclear structure studies of short-lived neutron-rich nuclei with the novel large-scale isochronous mass spectrometry at the FRS-ESR facility". Nucl. Phys. A, No. 812, p. 1, 2008. [cited at p. 13, 15, 91]

[Sun 09] B. Sun. Software development for ESR Isochronous Mass Spectrometry. GSI, Darmstadt, Germany; JLU Giessen, Germany, 2009. [cited at p. 87]

[Tan 85] I. Tanihata et al. "Measurements of interaction cross sections and nuclear radii in the light p-shell region". Phys. Rev. Lett., Vol. 55, No. 24, p. 2676, 1985. [cited at p. 2]

[Tro 93] J. Troetscher. Der Experimentierspeicherring der GSI als Flugzeitmassenspektrometer für exotische Nuklide. PhD thesis, Justus-Liebig Universität Gießen, 1993. [cited at p. 24, 34, 35, 43, 64]

[Vav 08] J. Va'vra. "A high-resolution TOD detector-A possible way to compete with a RICH detector". Nucl. Instr. and Meth. in Phys. Res. A, No. 595, p. 270, 2008. [cited at p. 56, 63]

[Wal 52] M. Walske. Phys. Rev., Vol. 88, No. 1283, 1952. [cited at p. 20]

[Wal 56] M. Walske. "The Stopping Power of L-Electrons". Phys. Rev., Vol. 101, No. 3, p. 940, 1956. [cited at p. 20]

[Win 08] M. Winkler, H. Geissel, and H. Weick. "The status of the Super-FRS in-flight facility at FAIR". Nucl. Ins. Meth. in Phys. Res. B, No. 266, p. 4183, 2008. [cited at p. 110]

[Wiz 79] J. Wiza. "Microchannel plate detector". Nucl. Instr. and Meth., Vol. 162, p. 587, 1979. [cited at p. 37]

[Wol 90] H. Wollnik. Manual for GICO. Justus-Liebig Universität Gießen, 1990. [cited at p. 22]

[Wol 97] H. Wollnik et al. "TOF Mass Measurements of Exotic Nuclei at the ESR of the GSI". Nucl. Phys. A, No. 626, p. 327c, 1997. [cited at p. 13, 17, 24]

[Xia 02] J. Xia et al. "The heavy ion cooler-storage-ring project (HIRFL-CSR) at Lanzhou". Nucl. Instr. and Meth. in Phys. Res. A, No. 488, p. 11, 2002. [cited at p. 12]

[Xia 09] T. Xiao-Lin. "A pilot experiment for mass measurement at CSRe.". Chinese Physics C, Vol. 33, No. 7, p. 516, 2009. [cited at p. 12]

Acknowledgements

I would like to thank all people who made this work possible. First and foremost I offer my sincerest gratitude to my supervisor Prof. Dr. Dr. h.c. Hans Geissel, who supported me during my work on thesis with his patience and knowledge whilst allowing me always a space to work in my own way.
I am very thankful to Dr. Wolfgang R. Plass a leader of IONAS group, who took particular care about our work. Thank you for all discussions, which helped me to develop the ideas put forward here.
I would like to thank Prof. Dr. Christoph Scheidenberger for warm welcome I received in IONAS group, who was an excellent supervisor during my Master work, shared his knowledge about the charge states and stopping power of relativistic heavy ions and did his best to make my stay in Giessen comfortable.
It is a pleasure to thank Prof. Dr. Yuri Pivovarov from Tomsk Polytechnic University (Russia) for introducing me to a world of science, for his excellent advises and strong support. Thank you, that once you saw a potential in me and offered the opportunity to study at JLU and GSI.
Special thanks go to my tutors Dr. Ronja Knöbel and Dr. Baohua Sun, who was essentially teaching me everything I know about IMS data analysis. I appreciate their effort to find time to answer my never-ending questions.
Dr. habil. Yuri Litvinov and Dr. Helmut Weick, I would like to thank for their support and help during the ESR experiments.
I am grateful to Dipl. Ing. Christos Karagiannis for the help with the TOF detector at the ESR and lab view development; to Dr. Benjamin Fabian, who introduced me to the TOF detector; to Dr. Thomas Faestermann and Dr. Roman Gernhäuser from TU München for supplying us with carbon foils; to Dr. Christopher Geppert for the opportunity to take an advantage of the laser setup for the efficiency measurement; to Reiner Weiss and his team from the mechanical workshop of the Physics Department for the efficient and precision machining.
A huge enormous thank to Dipl. Ing. Samuel Ayet for the simulations with

a new anode design and help with the measurements and to MS. Marcel Diwisch, for the help with a rate capability and timing measurements. It was a good challenge to be a supervisor of a "student".
Thank you to Dipl. Phys. Christian Jesch for taking care about the data storage during the experiment at the ESR.
Many thanks to all past and present members of IONAS-group at II.Physikalishes Institut and KP II department at GSI for the nice working atmosphere, interesting discussions and help in the lab. In particular I want to thank Dr. Timo Dickel, Dr. Martin Petrick, Dipl. Phys. Emma Haettner, Dr. Ekaterina Kozlova, Dr. Sergej Litvinov and Dr. Andrej Prochazka.
I wish to express my gratitude towards my boyfriend Andreas Feuerstein for the motivation and support during these years. Among many others, I thank Xiaoyu Qiang, Tatjana Kessler and Szilvia Major.
Despite the geographical distance, my family was always nearby. I wish to thank my parents, who has been a constant source of support - emotional, moral and of course financial throughout all my studies at Universities in Russia and Germany. To them I dedicate this thesis.

Ich erkläre: Ich habe die vorgelegte Dissertation selbständig und ohne unerlaubte fremde Hilfe und nur mit den Hilfen angefertigt, die ich in der Dissertation angegeben habe. Alle Textstellen, die wörtlich oder sinngemäß aus veröffentlichten Schriften entnommen sind, und alle Angaben, die auf mündlichen Auskunften beruhen, sind als solche kenntlich gemacht. Bei den von mir durchgeführten und in der Dissertation erwähnten Untersuchungen habe ich die Grundsätze guter wissenschaftlicher Praxis, wie sie in der "Satzung der Justus-Liebig-Universität Gießen zur Sicherung guter wissenschaftlicher Praxis" niedergelegt sind, eingehalten.

Gießen, 20 September 2011

Natalia Kuzminchuk